Design and development of functional dry adhesives and their applications

by

Jeffrey M. Krahn

M.A.Sc., Simon Fraser University, 2011

B.Sc., Simon Fraser University, 2008

Thesis Submitted in Partial Fulfillment of the
Requirements for the Degree of
Doctor of Philosophy

in the
School of Engineering Science
Faculty of Applied Science

SIMON FRASER UNIVERSITY

Fall 2014

Approval

Name: **Jeffrey M. Krahn**

Degree: **Doctor of Philosophy (Engineering Science)**

Title of Thesis: ***Design and development of functional dry adhesives and their applications***

Examining Committee: **Chair:** Dr. Shahram Payandeh

Dr. Carlo Menon, P.Eng.
Senior Supervisor
Associate Professor

Dr. Ash Parameswaran, P.Eng.
Supervisor
Professor

Dr. Bozena Kaminska
Supervisor
Professor

Dr. Bonnie Gray, P.Eng.
Internal Examiner
Associate Professor
School of Engineering Science

Dr. Konrad Walus, P.Eng.
External Examiner
Associate Professor
Electrical and Computer Engineering
University of British Columbia

Date Defended/Approved: October 17, 2014

Partial Copyright Licence

Abstract

Functional dry adhesives are dry adhesives that rely on dry adhesive structures for adhesion but also include additional functionality that enables adhesion switching or sensing capabilities. This thesis describes the design and testing of functional dry adhesives.

Electro-dry-adhesives with flexible electrodes were fabricated. When a high voltage was applied to the flexible electrodes, fabricated from mixing and curing Carbon Black (CB) and polydimethylsiloxane (PDMS), an electrostatic field was generated between opposing electrodes and between the Electro-dry-adhesive and the surface it was attached to. The generated electrostatic field resulted in an increased shear adhesion force over the shear adhesion measured without the applied electrostatic field applied as well as the ability to self-preload.

Magnetic field switchable dry adhesives were designed with a backing layer composed of iron oxide particles embedded within PDMS. The design of the dry adhesive backing layer allowed increased or decreased measured adhesion forces when the magnetic field was present during only the pull-off portion of the normal dry adhesion test cycle depending on the orientation of the magnetic field. Decreased adhesion was observed when the magnetic field was present during either the entire adhesion test cycle or when the magnetic field was present during only the preload portion of the dry adhesion test cycle regardless of the orientation of the magnetic field.

Force and torque sensing dry adhesives were designed and fabricated by molding CB-PDMS. Force sensing was observed when the device was both compressed and extended by measuring a change in the resistance across the device terminals. Torque sensing was observed when the dry adhesive backing layer was twisted again by comparing resistance changes across the device terminals. The design of the force and torque sensing dry adhesives allowed the user to differentiate between forces in compression and extension as well as torques.

Finally, a low cost method of fabricating dry adhesives was developed that utilizes commercially available meshes as a mold. The ability to utilize commercially available meshes instead of cleanroom fabrication techniques may save on overall fabrication costs and allow dry adhesives to be fabricated in large sheets.

Keywords: Biomimetic, dry adhesive, electrostatic, magnetic, polymer, mushroom caps

Acknowledgements

I would like to thank Dr. Carlo Menon, my senior supervisor, for providing such a great thesis project and for his continual feedback and encouragement.

Special thanks are extended to all members of the MENRVA research group for both their help and friendship.

Last but not least, I would like to thank my wife, Catherine McAllan, for her support, patience, encouragement and positive feedback.

Table of Contents

List of Tables

List of Figures

List of Acronyms

SFU	Simon Fraser University
PDMS	Poly(dimethylsiloxane)
PMMA	Poly(methtyl methacrylate)
PU	Polyurethane
PVS	Polyvinylsiloxane
PUA	Polyurethane acrylate
CB	Carbon Black
CB-PDMS	Carbon Black – Poly(dimethylsiloxane)
SEM	Scanning Electron Microscope
PP	Poly propylene
TFS	Torque and Force Sensing

Chapter 1. Introduction

1.1. Motivations

Adhesives are used to bind surfaces together and come in either 'dry' or 'wet' forms. Dry adhesives refer to adhesives which are capable of bonding to materials and yet, when removed, do not leave a residue. Wet adhesives on the other hand often leave a residue when peeled from a surface and are often referred to as either glue or tape. Table 1-1 summarizes some of the benefits and drawbacks of both wet and dry adhesives.

Table 1-1: Summary of the benefits and drawbacks of wet and dry adhesives

Type of adhesive	Benefits	Drawbacks
Dry adhesive	• Reusable • No residue left behind • Easily cleaned for reuse	• Expensive & time consuming fabrication processes • Currently limited to smooth surfaces
Wet adhesive	• Readily manufactured in sheets or rolls • Chemical • High adhesion bond strength • Can be used on many surfaces	• Non-reusable • Leave sticky residue • Not easily cleaned for reuse

In the last decade, research into biomimetic dry adhesives which are designed to mimic the structures used by gecko to adhere to a wide range of materials has led to a great many innovations and unique approaches to the development of biomimetic dry adhesives. While many improvements have been made, synthetic dry adhesives are still limited in their adhesion to a narrow range of materials and surfaces. In particular, they are limited to relatively smooth materials such as glass or Poly(methyl methacrylate) (PMMA) and, while adhesion is strong, could be greatly improved by the incorporation of switchable adhesion technology.

In order to improve the integration of biomimetic dry adhesives into climbing robots or other applications where temporary adhesion is required, such as signage or surveillance devices, it is desirable to have functional dry adhesives. Functional adhesives use the surface features of biomimetic dry adhesives to adhere to walls and other surfaces using van der Waals' forces but also integrate a secondary level of functionality within their structure. Proposed functionalities include switchable dry adhesives which can be quickly and easily switched between a low and high adhesion state or which can perform other functions such as force or torque measurements.

Rapid switching between a high and low adhesion state for dry adhesives used on climbing robots, signage or attachment of surveillance equipment is important because of the need for rapid attachment and detachment in order for a climbing robot to move quickly across a surface or for removal of surveillance equipment or signage. In order to develop switchable adhesives, both electrostatic and magnetic methods are explored within this thesis.

Another form of functional adhesives, also important for integration within an end device, is the ability for an object to sense when it is beginning to detach. The sooner the sign, surveillance camera or robot can detect detachment conditions the sooner it is able to recover and ensure its ability to continue adhering. Integration of both force and torque sensors within the dry adhesive structure ensures that the forces and torques acting on the surface of the adhesive are accurately understood by the device controller. This work discusses the design, fabrication and testing of force and torque sensing adhesives.

In order to ensure biomimetic dry adhesives can be integrated into everyday use, a robust but simple fabrication method should be developed. Currently, dry adhesives are manufactured in a cleanroom environment with highly specialized equipment. Due to the size constraints imposed by the equipment used, it can be very expensive to manufacture large sheets or rolls of dry adhesives. A low-cost method for fabrication of biomimetic dry adhesives is developed which utilizes commercially available mesh as a mold cavity.

1.2. Objectives

With the overall goal of designing functional dry adhesives through technological advancement and application development, the following objectives were established as a way to achieve this goal:

1. Design switchable dry adhesives that are capable of rapid switching between a high and low adhesion state
2. Design force and torque sensing dry adhesives
3. Design a manufacturing method to fabricate dry adhesives that does not require a cleanroom environment

Having met each of the three objectives, future work on dry adhesives will focus on integrating the dry adhesives fabricated using the manufacturing method listed as objective 3 into both the switchable and force and torque sensing dry adhesives designed in objectives 1 and 2.

1.3. Thesis layout

In this work, Chapter 2 provides a brief introduction to dry adhesives and provides justification for the dry adhesives made from Poly(dimethylsiloxane) (PDMS) as seen in the remaining chapters. Chapter 3 through to Chapter 7 are individually formed directly from 4 out of 5 papers published in peer-reviewed journals. The 5th paper is currently in press.

Objective 1 is addressed in chapters 3, 4 and 5. Chapter 3 begins by describing the design and fabrication of electro-dry-adhesives that synergistically combine biomimetic dry adhesives which utilize van der Waals' forces with the ability to generate electrostatic forces for increased adhesion and self-preloading. The electro-dry-adhesives are composed of a composite conductive polymer matrix that allows current to flow through the polymer. Chapter 3 expands on the concept of electro-dry-adhesion by showcasing an electro-dry-adhesive that enables multiple electrodes to be contained within a single device and which are designed for use on conductive surfaces.

Chapter 5 also addresses objective 1 but uses a different approach to that seen in chapters 3 and 4. Chapter 5 describes the design, fabrication and testing of dry adhesives with adhesion controlled through the application of a magnetic field. Depending on the orientation of the magnetic field or the point at which the magnetic field is applied during the normal adhesion test cycle, increased or decreased adhesion is observed.

Objective 2 is met in chapter 6 which describes the design, fabrication and testing of force and torque sensing dry adhesives. The force and torque sensing dry adhesives are capable of measuring forces in compression and extension as well as torques. The design of the force and torque sensing allows the user to differentiate whether a torque or force has been applied.

Finally, chapter 7 describes the development of a low-cost dry adhesive manufacturing process that does not require a cleanroom environment and is capable of being expanded to fabricating large sheets or rolls of dry adhesives thus meeting objective 3.

1.4. Scientific contributions

It has been a great honour to be able to share a portion of my scientific contributions with my fellow researchers in the form of the following peer-reviewed journal papers, peer-reviewed conference papers and abstract refereed conference papers:

1.4.1. Refereed journal papers

1. **Krahn J.**, Bovero E., and Menon C. (in press) Magnetic field switchable dry adhesives. Submitted August 1, 2014

2. Tannouri P., Arafeh K. M., **Krahn J. M.**, Beaupré S. L., Menon C. and Branda N. R. (2014) A photoresistive biomimetic dry adhesive based on doped PDMS microstructures, *Chem. Mater.* doi: 10.1021/cm502222c

3. Pattantyus-Abraham A. G., **Krahn J.**, and Menon C. (2013) Recent advances in nanostructured biomimetic dry adhesives. *Frontiers: Bioengineering and Biotechnology* doi: 10.3389/fbioe.2013.00022

4. **Krahn J. M.**, Pattantyus-Abraham A. G., and Menon C. (2013) Polymeric electro-dry-adhesives for use on conducting surfaces. *Proceedings of the Institution of Mechanical Engineers, Part L: Journal of Materials: Design and Applications*, doi: 10.1177/1464420713509376

5. **Krahn, J.** and Menon, C. (2013) Characterization of dry adhesives fabricated using a novel mass production manufacturing technique, *Macromolecular Reaction Engineering*, DOI: 10.1002/mren.201300111

6. **Krahn J.** and Menon C. (2013) Dry adhesives with sensing features, *Smart Materials and Structures* **22** 085010, doi:10.1088/0964-1726/22/8/085010

7. **Krahn J.** and Menon C. (2012) Electro-Dry-Adhesion *Langmuir* **28** 5438-43

1.4.2. Refereed conference papers

1. Diaz Tellez J. P., **Krahn J.** and Menon C. (2011) Characterization of electro-adhesives for robotic applications ROBIO pp 1867-72

1.4.3. Abstract refereed conference papers

1. Savioli L., Sguottia G., Francesconi A., Branz F., **Krahn J.**, and Menon C. (2014) Morphing adhesive interface to manipulate uncooperative objects, SPIE Smart Structures/NDE, San Diego, USA.

2. **Krahn J. M.**, Pattantyus-Abraham A. G., and Menon C. (2013) Dielectrophoretic self-cleaning dry adhesives AB2013 FEUP-Porto (4-5 July 2013)

3. **Krahn J. M.**, Pattantyus-Abraham A. G., and Menon C. (2013) Electro-dry-adhesives for use on conducting surfaces AB2013 FEUP-Porto (4-5 July 2013)

4. Branz F., Savoili L., Francesconi A., Sansone F., **Krahn J.** and Menon C. (2013) Soft-docking system for capture of irregularly shaped, uncontrolled space objects. 6th European Conference on Space Debris, ESA/ESOC Darmstadt, Germany (April 22-25)

Chapter 2. Design criteria and performance of PDMS dry adhesives presented in the literature

The following chapter provides a brief overview of the progress made in the field of biomimetic dry adhesives and provides insight into the dry adhesive fabrication methods used in subsequent chapters. A brief overview of the design and adhering properties of PDMS-based dry adhesives is also provided.

2.1. Overall design criteria for gecko-like dry adhesives

Since 2000, when it was determined that Van der Waals' forces were the main contributor to gecko adhesion[1,2], there have been many research groups worldwide that have spent a considerable amount of time fabricating and designing biomimetic dry adhesives. Most of their research has been focused on achieving one or more of the following properties listed below that highlight the ideal properties of synthetic dry adhesives that mimic the gecko foot[3]:

1. Adhesion primarily through van der Waals interactions
2. Anisotropic adhesion
3. A high pull-off to preload ratio
4. Low detachment force when required
5. Self-cleaning
6. Anti-self-matting/self-adhesion
7. A low to no adhesion state in the absence of shear

The following sections briefly address the progress in each of the seven highlighted properties of synthetic dry adhesives.

2.1.1. Adhesion mechanism

Researchers have shown that nearly all synthetic dry adhesives rely primarily on van der Waals forces for adhesion[1,4,5] although capillary forces[6,7] and more recently, electrostatic interactions[8], are thought to influence adhesion.

Van der Waals forces can be summarised as the forces between neutral molecules due to dipolar interactions and includes Coulomb interactions, monopole-dipole interaction and dipole-dipole interactions. The Coulomb force is the electrostatic force between two charges Q_1 and Q_2 separated by a distance, D, and can be calculated from:

$$F = \frac{Q_1 Q_2}{4\pi\varepsilon\varepsilon_0 D^2} \qquad \text{Equation 2-1}$$

Where ε_0 is the permittivity in a vacuum while ε is the relative permittivity of the material in which the charges are located[9].

For most molecules however the total electric charge is zero but may be unevenly distributed with a more positive and more negative side and are referred to as dipoles. The maximum potential energy between a monopole with charge Q and dipole with dipole moment, μ, separated by a distance, D, can be calculated from:

$$V(D) = -\frac{Q^2\mu^2}{6(4\pi\varepsilon_0)^2 k_B T D^4} \qquad \text{Equation 2-2}$$

Where k_B is Boltzmanns constant and T is the temperature in Kelvin[9].

Similarly, when two dipoles are allowed to rotate freely the thermally averaged dipole-dipole free energy can be determined from:

$$V(D) = -\frac{\mu_1^2\mu_2^2}{3(4\pi\varepsilon_0)^2 k_B T D^6} = -\frac{C_{orient}}{D^6} \qquad \text{Equation 2-3}$$

Which is referred to as the Keesom interaction[9].

The Helmholtz free energy, the energy due to the attractive force generated between a charge approaching a molecule without a static dipole moment is given by:

$$V = -\frac{Q^2\alpha}{2(4\pi\varepsilon_0)^2 D^4}$$ Equation 2-4

Where α is the polarisability. If the interaction is instead between a polarisable molecule and a static dipole, the Helmholtz free energy becomes related to the induced charge, C_{ind} by:

$$V = -\frac{\mu^2\alpha}{(4\pi\varepsilon_0)^2 D^6} = -\frac{C_{ind}}{D^6}$$ Equation 2-5

Which is referred to as the Debye interaction[9].

The free energy between two nonpolar molecules with ionization energies $h\nu_1$ and $h\nu_2$, referred to as the London dispersion interaction, can be approximated by[9]:

$$V = -\frac{3}{2}\frac{\alpha_1\alpha_2}{(4\pi\varepsilon_0)^2 D^6}\frac{h\nu_1\nu_2}{(\nu_1+\nu_2)} = -\frac{C_{disp}}{D^6}$$ Equation 2-6

Finally, Van der Waals interactions are the sum of the Keesom, Debye and London dispersion interactions and can be estimated from[9]:

$$V_{vdW} = -\frac{C_{orient}+C_{ind}+C_{disp}}{D^6}$$ Equation 2-7

While it can be useful to calculate the attractive forces between individual molecules, it is often more practical to calculate the Van der Waals' forces between macroscopic solids. Hamaker's approach was to relate the density of molecules in material A, Q_A , and for material B, Q_B, to the sum of the Keesom, debye and London dispersion interactions between the two materials, C_{AB}, in order to calculate the Hamaker constant, A_H[9]:

$$A_H = \pi^2 C_{AB} Q_A Q_B$$ Equation 2-8

The Van der Waals' energy between the two solids is then given by[10]:

$$V = -\frac{A_H}{12\pi D^2}$$ Equation 2-9

The force per unit area, f, is then:

$$\boldsymbol{f} = -\frac{A_H}{6\pi D^3}$$ Equation 2-10

For two spheres with radii R_1 and R_2, Van der Waals found the energy between the two spheres to be[9]:

$$V = -\frac{A_H}{6}\left[\frac{2R_1R_2}{d_{cc}^2-(R_1+R_2)^2} + \frac{2R_1R_2}{d_{cc}^2-(R_1-R_2)^2} + ln\left(\frac{d_{cc}^2-(R_1+R_2)^2}{d_{cc}^2-(R_1-R_2)^2}\right)\right]$$ Equation 2-11

Where d_{cc} is the distance separating the centre of the spheres.

If the radii of the spheres are greater than the distance between them, the Van der Waals force between the two spheres can be reduced to[10]:

$$F = \frac{A_H}{6D^2}\frac{R_1R_2}{R_1+R_2}$$ Equation 2-12

Finally, the Van der Waals' force between a plane and a sphere can be found by letting the radius of one of the spheres go to infinity[10]:

$$F = \frac{A_H R_1}{6D}$$ Equation 2-13

2.1.2. Anisotropic adhesion

Anisotropic adhesion is defined as adhesion that is either direction dependent or includes additional functionality which enables adhesion switching. Typically, direction dependent adhesion means that when peeled in the primary adhesion direction the observed adhesion forces are increased over those seen in the other directions. Synthetic anisotropic dry adhesion has been observed by fabricating dry adhesive fibres with offset[11] or angled caps[12]. Switchable dry adhesives have been achieved by using a phase-change backing layer[13] or shape memory polymers.

2.1.3. High pulloff to preload ratio

In order to achieve the close surface-surface contact required for Van der Waals' interactions to occur, dry adhesives typically require a preloading force. A preloading force simply pushes the dry adhesive surface into contact with the attachment substrate and allows it to conform to the attachment substrate ensuring good surface-surface

contact and thus increasing adhesion. While actual measured adhesion values are dependent on the fibre material and shape, a typical preload-pulloff curve will display an exponential increase in adhesion for increasing preload until the preload-pulloff relationship levels off due to contact area saturation[14–16].

2.1.4. Low detachment force when required

The desire for a low detachment force when required is similar to property 2, anisotropic adhesion, and has led researchers to develop several interesting methods for designing switchable dry adhesives including the inclusion of phase-change backing layers[13], shape memory pillars of fibres[17]. The desire for new methods of providing switchable adhesion was one of the inspirations for this thesis.

2.1.5. Self-cleaning

To date, self-cleaning dry adhesives have been fabricated with high aspect ratios using a variety of materials such as polypropylene[18], polyurethane[19] or polyethylene[20]. Additionally, self-cleaning has required that the dry adhesive be dragged along a surface[18] or rinsed with water[20]. Another approach to self-cleaning that requires further investigation is the use of electrostatic fields.

2.1.6. Anti-self-matting/self-adhesion

From the early days in synthetic dry adhesive research, anti-self matting has been achieved by adjusting the aspect ratio of the individual fibres along with reducing their density. In general, high aspect ratio fibres tend to collapse on each other either by their own weight or when preloaded[3,21] and, because of their affinity for Van der Waals' interactions, form a dense mat of interconnected fibres.

2.1.7. Low to no adhesion state in the absence of shear

A low adhesion state in the absence of shear enables the gecko to quickly detach itself from a surface and would be an ideal property for dry adhesives designed for climbing robots or sign attachment. The inclusion of a low to no adhesion state in the

absence of shear would help prevent fibers from spontaneously attaching to each other and engaging the attachment substrate unless desired[3].

2.2. Dry adhesive fibre design: optimal shape and size

For strong adhesion, dry adhesives that rely on van der Waals forces require a large contact area with the surface they are adhering to[5]. While a large contact area on smooth surfaces can be achieved with a flat unstructured surface, an increase in surface roughness may result in a decrease in the actual contact area and in decreased adhesion. The reduced adhesion due to increased surface roughness has led researchers to fabricate dry adhesives composed of arrays of fibres[13,22–24] which, while resulting in an overall decrease in available surface area, are able to better conform to surfaces with the end result being an increase in overall adhesion. Research indicates that the contact surface should still be as large as possible for a given post diameter while avoiding collapsing the posts[25]. Similarly, increased adhesion has been reported with high aspect ratio fibres as long as the posts do not collapse[14]. Another benefit of designing dry adhesives fibres in arrays of fibres is a resistance to peeling due to a resistance in crack propagation[26]. The term crack propagation refers to the way the adhesives are peeled from a contact substrate where peeling is initiated at the edge of the contact area and a crack forms between the two surfaces. As the two surfaces are peeled apart, the crack propagates across the contact area until the adhesive is entirely peeled from the substrate.

The shape of the fibre tip, which also defines the contact surface[14,21], has also been shown to affect adhesion. Again, the shape of the fibre tip is thought to enhance peeling resistance by resisting crack formation with a flat overhanging mushroom-like cap design providing enhanced adhesion while a flat or spherical fibre tip provides reduced adhesion[27]. Several researchers have used offset[11] or angled[12] overhanging caps to provide anisotropic or directional adhesion which provides strong adhesion when peeled in one direction but decreased adhesion when peeled from the opposite direction.

2.3. Synthetic dry adhesives: common materials

Another important aspect to dry adhesive design is the intrinsic properties of the material that is used to fabricate the surface structures of the dry adhesives. Generally, researchers have reported molding dry adhesive from elastomers such as polydimethylsiloxane (PDMS)[11,13,24,25,28,29], PVS[30,31] or polyurethanes (PU)[20,32,33] although Teflon AF[34] and PMMA[35] have also been reported. Due to the ease of use and measured adhesion pressures of as high as 219 kPa[3] for structured fibres, PDMS, often manufactured by Dow Corning as Sylgard 184, has been one of the most commonly used materials for dry adhesive fibres. Another commonly used elastomer is a polyurathane from BJB enterprises (ST-1060). Although surface energies, material strength and visco elastic properties are very different, Sylgard 184 and ST-1060 have comparable Young's modulus (~2-3 MPa) and Shore Hardness (~Shore A 60 hardness)[3].

2.4. Reliability of dry adhesives

While considerable effort has been expended in developing strong dry adhesives which could conform to a wide range surfaces and which mimic the functionality of the gecko, much less effort has been expended on testing the long-term reliability or the effects of exposure to varying environmental conditions. The following sections outline the long term and environmental testing performed by Mike Henrey, a former member of the MENRVA research group. All of the testing described here was done on dry adhesives manufactured from molds fabricated using the manufacturing process initially developed by Dan Sameoto.

2.4.1. Adhesion cycle testing: long term adhesion testing

Several authors have noted long-term adhesion degradation when describing their PDMS dry adhesives[36,37]. Under laboratory test conditions, while developing a spider-like climbing robot, it was reported that over 2000 cycles a 12% adhesive degradation was observed. Interestingly, peak adhesive performance was observed during approximately the first 100 cycles followed by a period of degradation over the

next 500 cycles. After approximately 600 cycles, the measured adhesive force leveled off and remained approximately constant for the remaining 1400 adhesion test cycles. However, when being used on the climbing robot, the life cycle of the dry adhesives, as defined by the ability of the robot to climb a wall, was only approximately 570 cycles[36]. The reduction in life cycles may be due to an increased accumulation of dust when in use on the robot.

2.4.2. Effect of temperature on dry adhesion

Using a Nano-Scratch Tester (NST) the effect of temperature on the adhesion of PDMS dry adhesives manufactured within the MENRVA group was explored by Mike Henrey. Adhesion testing was performed at temperatures ranging from -50 to +75 ^{o}C at a pressure 1 x 10^{-5}mbar. When comparing the effect of temperature on adhesion over a total of 450 adhesion test measurements, no significant change in adhesion was observed[38] which indicates that PDMS dry adhesives are suitable for use over a wide range of temperatures.

2.4.3. Effect of pressure on dry adhesion

Using the same NST described in the previous section, adhesion tests were performed at a range of pressures ranging from atmospheric pressure down to 1 x 10^{-5}mbar. Adhesion test results indicate that while there was a 6% change in the effective Young's modulus, thought to be due to either outgassing or the ultra-low humidity under vacuum, there was no observed change in the saturation adhesion between vacuum and atmospheric testing[38].

2.4.4. Effect of relative humidity on dry adhesion

Relative humidity (RH) has been shown to affect the adhesion of the setae of the Tokay Gecko with measured adhesion forces rising from nearly 0 at 15% RH to a maximum at approximately 90% RH and is thought to be related to changes in materials properties[39]. Synthetic dry adhesives made from PDMS on the other hand showed no significant change in adhesion over relative humidity ranging from 2 to 90%[16].

2.5. Comparison of dry adhesive designs

Table 2-1 provides a summary of the adhesive strength provided by various fibre shapes and materials.

Table 2-1: Summary of the adhesion levels achieved through various fibre designs and materials

Material	Approximate Young's Modulus [MPa]	Aspect ratio (Height: radius)	Fibre shape	Tested area [cm^2]	Preload	Maximum adhesion	Reference
PU	150	6.5	Mushroom-like fibres	1	2mN	270 kPa	[40]
PDMS	0.6	2	Mushroom-like fibres	0.33	300mN	220 kPa	[29]
PU	2.9	4	Mushroom-like fibres	0.02	12N	18N cm^{-2}	[19]
PU	2.9	4.88	Spatula tipped fibres	0.03	6.7N cm^{-2}	14.1N cm^{-2}	[41]
PDMS	2.5	1	Mushroom-like fibre	0.01	20mN	90kPa	[25]
PDMS	2	1	Mushroom-like fibres	1.35	Pressed by hand	6.86N	[11]
PU	2.9	2	Flared tip	0.01	8mN	40mN	[33]
PU	2.9	2.86	Angled spatula tipped	1	5mN	50kPa	[32]
Polyurethane acrylate (PUA)	19.8	11.11	Bent cylindrical fibres with round tip	1	0.3N	39nN/hair	[42]
Polyvinylsiloxane (PVS)	3	2	Mushroom-like fibres	0.1	90mN	120mN	[43]
PDMS	1.51	2.4	Flared tip and graphed Poly(n-butyl acrylate) fibres	0.015	16mN	16mN	[44]
PDMS	1.75	4	Wedge shaped fibres	1	80µm depth	5.1kPa	[24]
PMMA	2000	21.25	Rounded tip fibres	1	Unknown	3-4N	[45]

2.6. Conclusion

Since 2000, researchers have made significant strides in designing dry adhesives and understanding the mechanism through which they adhere. PDMS has become a popular material for manufacturing dry adhesives due to a number of factors including ease of use and high adhesion. Dry adhesives manufactured from PDMS have been shown to provide stable and reliable adhesion over temperatures ranging from -50 to +75 ^{o}C, RH ranging from 2 to 90% and at pressures ranging from 1 x 10^{-5}mbar to atmospheric pressure.

In this work, I focus on dry adhesives made from PDMS because of the properties described above along with the use of a reliable mold manufacturing process which was initially developed by Dan Sameoto, a former member of the MENRVA research group[11,25]. Using a variation of the method pioneered by Dr. Sameoto, I was able to quickly manufacture my own molds and concentrate on designing functional dry adhesives.

2.7. References

(1) Autumn, K.; Sitti, M.; Liang, Y. A.; Peattie, A. M.; Hansen, W. R.; Sponberg, S.; Kenny, T. W.; Fearing, R.; Israelachvili, J. N.; Full, R. J. Evidence for van Der Waals Adhesion in Gecko Setae. *Proc. Natl. Acad. Sci. U. S. A.* **2002**, *99*, 12252–12256.

(2) Autumn, K.; Liang, Y. a; Hsieh, S. T.; Zesch, W.; Chan, W. P.; Kenny, T. W.; Fearing, R.; Full, R. J. Adhesive Force of a Single Gecko Foot-Hair. *Nature* **2000**, *405*, 681–685.

(3) Sameoto, D.; Menon, C. Recent Advances in the Fabrication and Adhesion Testing of Biomimetic Dry Adhesives. *Smart Mater. Struct.* **2010**, *19*, 103001.

(4) Geim, A. K.; Dubonos, S. V; Grigorieva, I. V; Novoselov, K. S.; Zhukov, A. A.; Shapoval, S. Y. Microfabricated Adhesive Mimicking Gecko Foot-Hair. *Nat. Mater.* **2003**, *2*, 461–463.

(5) Jagota, A.; Bennison, S. J. Mechanics of Adhesion through a Fibrillar Microstructure. *Integr. Comp. Biol.* **2002**, *42*, 1140–1145.

(6) Huber, G.; Mantz, H.; Spolenak, R.; Mecke, K.; Jacobs, K.; Gorb, S. N.; Arzt, E. Evidence for Capillarity Contributions to Gecko Adhesion from Single Spatula Nanomechanical Measurements. *Proc. Natl. Acad. Sci. U. S. A.* **2005**, *102*, 16293–16296.

(7) Sun, W.; Neuzil, P.; Kustandi, T. S.; Oh, S.; Samper, V. D. The Nature of the Gecko Lizard Adhesive Force. *Biophys. J.* **2005**, *89*, L14–7.

(8) Izadi, H.; Penlidis, A. Polymeric Bioinspired Dry Adhesives: Van Der Waals or Electrostatic Interactions? *Macromol. React. Eng.* **2013**, *7*, 588–608.

(9) Kappl, M.; Butt, H.-J. *Surface and Interfacial Forces*; WILEY-VCH Verlag GmbH & Co. KGaA: Weinheim, 2010.

(10) Parsegian, V. A. *Van Der Waals Forces: A Handbook for Biologists, Chemists, Engineers, and Physicists*; Cambridge University Press: Cambridge, 2006; p. 396.

(11) Sameoto, D.; Menon, C. Direct Molding of Dry Adhesives with Anisotropic Peel Strength Using an Offset Lift-off Photoresist Mold. *J. Micromechanics Microengineering* **2009**, *19*, 115026.

(12) Jeong, H. E.; Suh, K. Y. Nanohairs and Nanotubes: Efficient Structural Elements for Gecko-Inspired Artificial Dry Adhesives. *Nano Today* **2009**, *4*, 335–346.

(13) Krahn, J.; Sameoto, D.; Menon, C. Controllable Biomimetic Adhesion Using Embedded Phase Change Material. *Smart Mater. Struct.* **2011**, *20*, 015014.

(14) Greiner, C.; Campo, A. Del; Arzt, E. Adhesion of Bioinspired Micropatterned Surfaces: Effects of Pillar Radius, Aspect Ratio, and Preload. *Langmuir* **2007**, *23*, 3495–3502.

(15) Henrey, M.; Wormnes, K.; Pambaguian, L.; Menon, C. Sticking in Space: Manufacturing Dry Adhesvies and Testing Their Performance in Space Environments. In.

(16) Greiner, C.; Buhl, S.; del Campo, A.; Arzt, E. Experimental Parameters Controlling Adhesion of Biomimetic Fibrillar Surfaces. *J. Adhes.* **2009**, *85*, 646–661.

(17) Reddy, S.; Arzt, E.; del Campo, a. Bioinspired Surfaces with Switchable Adhesion. *Adv. Mater.* **2007**, *19*, 3833–3837.

(18) Lee, J.; Fearing, R. S. Contact Self-Cleaning of Synthetic Gecko Adhesive from Polymer Microfibers. *Langmuir* **2008**, *24*, 10587–10591.

(19) Kim, S.; Cheung, E.; Sitti, M. Wet Self-Cleaning of Biologically Inspired Elastomer Mushroom Shaped Microfibrillar Adhesives. *Langmuir* **2009**, *25*, 7196–7199.

(20) Lee, J.; Fearing, R. S. Wet Self-Cleaning of Superhydrophobic Microfiber Adhesives Formed from High Density Polyethylene. *Langmuir* **2012**, *28*, 15372–15377.

(21) Parsaiyan, H.; Barazandeh, F.; Mehdirezaei, S.; Parsaiyan, M.; Safdari, M. Wide-End Fibers and Their Adhesion Performance in Biological Attachment Systems. *Int. J. Adhes. Adhes.* **2009**, *29*, 444–450.

(22) Long, R.; Hui, C.-Y.; Kim, S.; Sitti, M. Modeling the Soft Backing Layer Thickness Effect on Adhesion of Elastic Microfiber Arrays. *J. Appl. Phys.* **2008**, *104*, 044301.

(23) Aksak, B.; Murphy, M. P.; Sitti, M. Adhesion of Biologically Inspired Vertical and Angled Polymer Microfiber Arrays. *Langmuir* **2007**, *23*, 3322–3332.

(24) Parness, A.; Soto, D.; Esparza, N.; Gravish, N.; Wilkinson, M.; Autumn, K.; Cutkosky, M. A Microfabricated Wedge-Shaped Adhesive Array Displaying Gecko-like Dynamic Adhesion, Directionality and Long Lifetime. *J. R. Soc. Interface* **2009**, *6*, 1223–1232.

(25) Sameoto, D.; Menon, C. A Low-Cost, High-Yield Fabrication Method for Producing Optimized Biomimetic Dry Adhesives. *J. Micromechanics Microengineering* **2009**, *19*, 115002.

(26) Chung, J. Y.; Chaudhury, M. K. Roles of Discontinuities in Bio-Inspired Adhesive Pads. *J. R. Soc. Interface* **2005**, *2*, 55–61.

(27) Del Campo, A.; Greiner, C.; Arzt, E. Contact Shape Controls Adhesion of Bioinspired Fibrillar Surfaces. *Langmuir* **2007**, *23*, 10235–10243.

(28) Krahn, J.; Liu, Y.; Sadeghi, A.; Menon, C. A Tailless Timing Belt Platform (TBCP-II) Utilizing Dry Adhesives with Mushroom Caps. *Smart Mater. Struct.* **2011**, *20*, 11.

(29) Davies, J.; Haq, S.; Hawke, T.; Sargent, J. A Practical Approach to the Development of a Synthetic Gecko Tape. *Int. J. Adhes. Adhes.* **2009**, *29*, 380–390.

(30) Varenberg, M.; Gorb, S. Shearing of Fibrillar Adhesive Microstructure: Friction and Shear-Related Changes in Pull-off Force. *J. R. Soc. Interface* **2007**, *4*, 721–725.

(31) Varenberg, M.; Gorb, S. Close-up of Mushroom-Shaped Fibrillar Adhesive Microstructure: Contact Element Behaviour. *J. R. Soc. Interface* **2008**, *5*, 785–789.

(32) Murphy, M. P.; Aksak, B.; Sitti, M. Gecko-Inspired Directional and Controllable Adhesion. *Small* **2009**, *5*, 170–175.

(33) Aksak, B.; Murphy, M. P.; Sitti, M. Gecko Inspired Micro-Fibrillar Adhesives for Wall Climbing Robots on Micro / Nanoscale Rough Surfaces. In *IEEE International Conference on Robotics and Automation*; 2008; pp. 3058–3063.

(34) Izadi, H. Gecko Adhesion and Gecko-Inspired Dry Adhesives: From Fundamentals to Characterization and Fabrication Aspects, University of Waterloo, 2014, p. 203.

(35) Jeong, H. E.; Lee, S. H.; Kim, P.; Suh, K. Y. Stretched Polymer Nanohairs by Nanodrawing. *Nano Lett.* **2006**, *6*, 1508–1513.

(36) Henrey, M.; Ahmed, A.; Boscariol, P.; Shannon, L.; Menon, C. Abigaille-III: A Versatile, Bioinspired Hexapod for Scaling Smooth Vertical Surfaces. *J. Bionic Eng.* **2014**, *11*, 1–17.

(37) Kroner, E.; Maboudian, R.; Arzt, E. Adhesion Characteristics of PDMS Surface during Repeated Pull-off Force Measurements. *Adv. Eng. Mater.* **2010**, *12*, 398–404.

(38) Henrey, M.; Díaz Téllez, J. P.; Wormnes, K.; Pambaguian, L.; Menon, C. Towards the Use of Mushroom-Capped Dry Adhesives in Outer Space: Effects of Low Pressure and Temperature on Adhesion Strength. *Aerosp. Sci. Technol.* **2013**, *29*, 185–190.

(39) Puthoff, J. B.; Prowse, M. S.; Wilkinson, M.; Autumn, K. Changes in Materials Properties Explain the Effects of Humidity on Gecko Adhesion. *J. Exp. Biol.* **2010**, *213*, 3699–3704.

(40) Sameoto, D.; Menon, C. Deep UV Patterning of Acrylic Masters for Molding Biomimetic Dry Adhesives. *J. Micromechanics Microengineering* **2010**, *20*, 115037.

(41) Kim, S.; Sitti, M.; Jang, J.-H.; Thomas, E. L. Fabrication of Bio-Inspired Elastomer Nanofiber Arrays with Spatulate Tips Using Notching Effect. In *Nanotechnology, 2008. NANO '08. 8th IEEE Conference on*; 2008; pp. 780–782.

(42) Kim, T.; Jeong, H. E.; Suh, K. Y.; Lee, H. H. Stooped Nanohairs: Geometry-Controllable, Unidirectional, Reversible and Robust Gecko-like Dry Adhesive. *Adv. Mater.* **2009**, *21*, 2276–2281.

(43) Varenburg, M.; Gorb, S. A Beetle-Inspired Solution for Underwater Adhesion. *J. R. Soc. Interface* **2008**, *5*, 383–385.

(44) Sitti, M.; Cusick, B.; Aksak, B.; Nese, A.; Lee, H.-I.; Dong, H.; Kowalewski, T.; Matyjaszewski, K. Dangling Chain Elastomers as Repeatable Fibrillar Adhesives. *Appl. Mater. Interfaces* **2009**, *1*, 2277–2287.

(45) Jeong, H. E.; Lee, S. H.; Kim, P.; Suh, K. Y. High Aspect-Ratio Polymer Nanostructures by Tailored Capillarity and Adhesive Force Colloids. *Colloids Surfaces A Physicochmeical Eng. Asp.* **2008**, *313-314*, 359–364.

Chapter 3. Electro-dry-adhesion

The content of this chapter has been slightly modified from what first appeared in print in:

Krahn, Jeffrey and Menon, Carlo. Electro-dry-adhesion. *Langmuir* 2012, 28, 8438-5443

3.1. Abstract

This work presents novel conductive bioinspired dry adhesives with mushroom caps that enable the use of a synergistic combination of electrostatic and van der Waals forces (electro-dry-adhesion). An increase in shear adhesion bond strength of up to 2600% on a wide range of materials is measured when a maximum electrical field of $36.4 V\mu m^{-1}$ is applied. A suction effect, due to the shape of the dry adhesive fibers, on overall adhesion was not noted for electro-dry-adhesives when testing was performed at both atmospheric and reduced pressure. Utilization of electrostatics to apply a preloading force to dry adhesive fiber arrays allows increased adhesion even after electrostatic force generation has been halted by ensuring the close contact necessary for van der Waals forces to be effective. A comparison is made between self-preloading of the electro-dry-adhesives and the direct application of a normal preloading pressure resulting in nearly the same shear bond strength with an applied voltage of 3.33kV on the same sample.

3.2. Introduction

Biomimetic dry adhesives based on the fibrillar structures used by geckos to adhere to a wide range of materials are thought to rely on van der Waals' forces for attachment[1]. Over the last several years researchers have developed a number of

techniques to manufacture arrays of biomimetic dry adhesive fibres. These include, among others, nano-drawing[2], nano-imprinting[3], plasma etching of polyimide[4] and poly(dimethylsiloxane) (PDMS) demoulding[5–7]. In order to achieve increased levels of adhesion several techniques have been used such as increasing the number of individual fibres in conjunction with decreasing fibre diameter and a subsequent increase in density[8]. Factors shown to affect the overall level of adhesion include the aspect ratio of the fibres and variation in the size and shape of the mushroom-like cap overhang[9–12], changing the stiffness of the backing layer[7] and fiber hierarchy which enables better conformation and attachment to rough surfaces[13, 14]. Recent studies have developed dry adhesives for use in a wide range of environments including use on both wet and dry surfaces[15] as well as medically compatible versions[16, 17].

While further research has been ongoing in the development of biomimetic dry adhesives, at the same time different research groups have been developing and manufacturing a range of conductive polymers. Conductive polymers are typically made by adding nano- or micro-sized particles to normally non-conductive polymers such as UV-curable monomers[18], PDMS[19–21], polypropylene or polyurethanes[22]. These conductive polymers have been developed for a wide range of uses including flexible circuits[21] and the sensing of liquids[22]. The particles commonly used in conductive polymers have been carbon nanotubes[18, 20, 23], carbon black[19, 21, 22] (CB) or silver[19, 21] (Ag). The overall conductivity of the particle-polymer mix is a direct result of the percentage of particles by weight mixed into the polymer and the conductivity of the individual particles.

While documented research on electrostatics dates back to the early 1700's[24], research has continued to be very active in the last few years as researchers have focused on a number of different areas of interest. The generation of electrostatic forces between electrodes and an attachment substrate has been used for a variety of applications including attachment systems for grippers[25, 26], robots used in assembly lines for the manufacturing of clothing[27] and in the semiconductor fabrication industry as electrostatic chucks[28–30]. Recently, another application for electrostatic forces has been as an attachment method for climbing robots[31–33] where the generation of electrostatic forces to adhere a robot to a wall is often referred to as electro-adhesion.

3.3. Experimental

In this work, conductive biomimetic dry adhesives with mushroom caps were manufactured by mixing 20-50nm[34] diameter CB particles (Vulcan XC-72R) with PDMS (Sylgard 184) to form a composite of CB and PDMS (CB-PDMS). CB-PDMS was then allowed to cure on moulds to ensure the surface of the cured CB-PDMS retained the biomimetic dry adhesive features. For this study, the moulds were manufactured similarly to those previously reported[6, 7] with the moulds themselves being capable of reliably reproducing uniform arrays of fibers which were composed of a mushroom-like cap 1.8μm thick and 17.8μm in diameter atop a post with a 9.3μm diameter for a total height of 10.5μm.

CB-PDMS was manufactured by first mixing PDMS in a 10:1 mixture of prepolymer to curing agent by weight. The desired amount of CB was then measured in order to achieve the desired conductivity within the CB-PDMS. After weighing out the amount of CB to be used, the CB and PDMS were mixed together by adding a portion of the predetermined amount of CB to the CB-PDMS mix and stirring by hand until the CB was mixed throughout the PDMS. Once the desired concentration of CB was achieved, the CB-PDMS mixture, now with a much thicker consistency than regular PDMS, was then spread over the mould while exerting downward pressure to ensure that the CB particles were forced into the micro-scale features of the mould. A room temperature degassing period allowed some uncured PDMS to seep from the CB-PDMS into the much smaller mushroom cap portion of the mould and ensure the formation of mushroom caps. After two hours of pre-curing at room temperature, the mould and partially cured CB-PDMS was transferred to an 80^0C oven to complete the curing process for a further three hours to ensure the PDMS had cross-linked to form the final CB-PDMS polymer. A scanning electron microscope (SEM) image of the conductive dry adhesive fibers can be seen in Figure 3-1. From the image, it can be seen that the adhesive fibers appear to have an inset central region above the conductive post with a bulged outer overhanging ring.

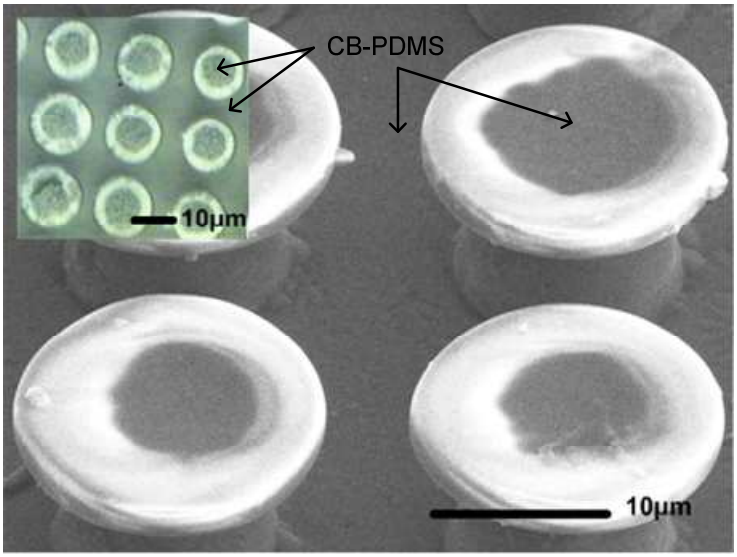

Figure 3-1: Scanning Electron Microscope (SEM) image of the CB-PDMS microstructures with an inset microscope image showing a bulged overhanging outer rim and an inner inset region which did not produce a significant suction effect during adhesion tests. The dark areas indicated by the arrows are composed of CB-PDMS.

During initial testing, conductive dry adhesives composed with higher concentrations of CB provided increased adhesion over samples fabricated with lower concentrations of CB. This is likely due to the increased conductivity of samples allowing a more even charge distribution across the entire sample resulting in increased adhesion even though the individual fibers were stiffer at these higher concentrations.

3.4. Results and Discussions

In order to determine the conductivity of the carbon filled posts, a microelectronic probe station with four micro-manipulators was used to ensure contact was made with the tips of four linearly evenly spaced posts. Each contact probe was connected directly to a digital multimeter configured for four terminal sensing. With this configuration, as seen in Figure 3-2, the resistance through the fibers and backing layer was measured in order to show that while very few CB particles, as indicated in Figure 3-1, were forced into the overhanging mushroom cap during the manufacturing process, the posts themselves were filled with particles resulting in conductive fibers. Measurements were

made at different locations on the samples with similar results indicating that mixing was uniform throughout the sample.

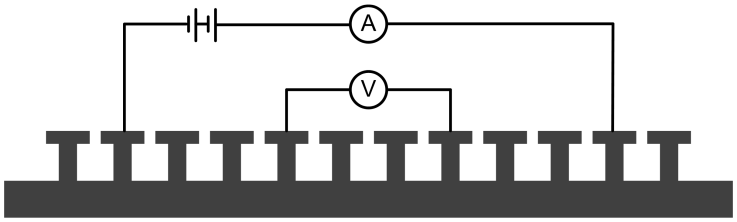

Figure 3-2: Four-terminal sensing being used to measure the resistance of the individual fibers and the backing layer. Four micro-manipulator probe tips were used to contact the tips of four individual and evenly spaced dry adhesive fibers

The conductivity, σ, of the composite CB-PDMS was directly related to the weight percentage of CB added to PDMS as shown in Figure 3-3. The conductivity was determined by using the following relationship[35]:

$$\sigma = \frac{1}{2\pi sR} \qquad \text{Equation 3-1}$$

where R is the resistance, determined by a 4-wire resistance measurement, and s is the distance between the tips of each of the four linearly aligned, evenly spaced, wires on the surface of the CB-PDMS.

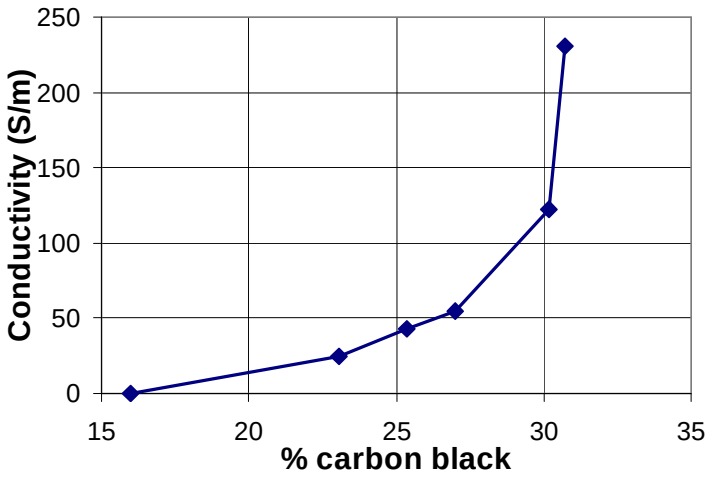

Figure 3-3: Relationship between the CB particle concentration in PDMS and the resulting measured conductivity.

Similar to the increasing conductivity of CB-PDMS by addition of CB, increasing the concentration of CB particles within PDMS results in an increase in the stiffness of the CB-PDMS material. A minimum of three tensile tests was performed on each of three variations of CB-PDMS and the results were averaged in order to determine the Young's modulus of each variation (Figure 3-4). For PDMS without the inclusion of CB particles, the measured material stiffness was 1622±99kPA, which is in agreement with previously reported results[36]. For 23.2% and 24.4% CB by weight in PDMS, the Young's modulus was measured to be 2247±215kPa and 3397±88kPa respectively.

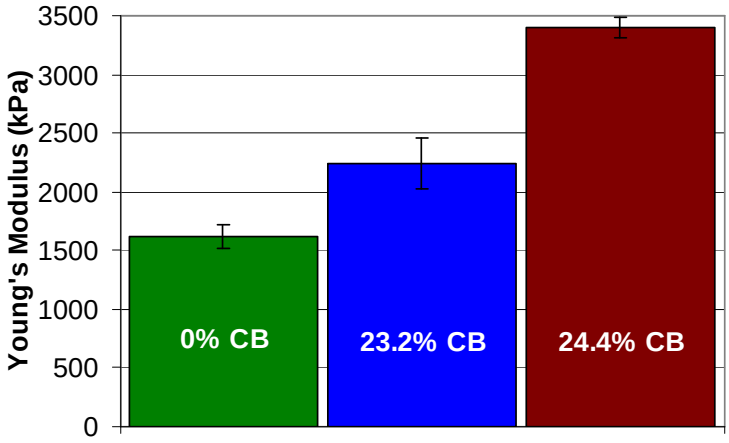

Figure 3-4: Increasing material stiffness of CB-PDMS with increasing particle concentration.

While the ability to manufacture conductive dry adhesive fibers adds to the list of potential uses for polymer-based biomimetic dry adhesives, the conductive adhesive sheets were, when combined with electro-adhesion, capable of substantial increases in the level of adhesion over that measured for flat CB-PDMS samples. Indeed, while dry adhesives have been shown to work well on smooth surfaces such as glass or PMMA, incorporating electro-adhesion into the adhesives themselves allows biomimetic adhesives to be used on a wider range of surfaces including drywall and polypropylene (PP). In order to measure the increase in adhesion strength when applying an electric field, two separate square conductive dry adhesive electrodes, each with an area of 43.56cm^2 and a thickness of 0.9mm, were placed on the substrate on which testing was performed. Figure 3-5 shows a conceptual diagram of two separate conductive dry adhesives placed on a dielectric insulator being used as electrodes to generate an attractive electrostatic force between themselves and the conductive layer. It should be noted that electro-dry-adhesion does not however require both a conductive layer and dielectric insulating layer as long as the attachment substrate is non-conducting.

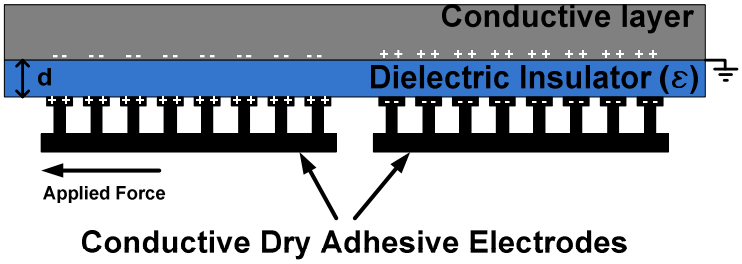

Figure 3-5: Conceptual diagram of two conductive dry adhesive electrodes being used to generate an attractive electrostatic force.

For the purpose of testing the overall shear adhesion provided by combining dry adhesion and electro-adhesion, tests were performed on PP, PMMA and unpainted drywall (gypsum board). Since PP and PMMA are dielectric insulators (110μm and 2.56mm thick respectively), a conductive layer, arbitrarily chosen to be steel (11 gauge, A366), was used to prove the effectiveness of electro-dry-adhesion. In the case of drywall, the rough unpainted paper outer layer acted as the dielectric material and the applied electrostatic force was between the electrode and the drywall sheeting's inner gypsum layer. During testing, two CB-PDMS electrodes with the same area were placed side by side on the material on which tests were performed and a range of voltages from 0 to 4kV were applied across the electrodes. After applying the desired voltage across the electrodes, the shear adhesion bond strength of one of the conductive dry adhesive electrodes was measured. While the DC-DC voltage convertor (EMCO, E101CT) was capable of outputting up to 5kV, the maximum voltage applied to the electrodes during testing was 4kV. This was done in order to maintain a consistent testing environment while avoiding a voltage breakdown at higher voltages between individual electrodes which were separated by a 1cm air gap during testing. All electrical connections were arranged so that they did not affect or interfere with the shear adhesion force measurements. After the desired voltage had been applied, a spring scale (globe) was used to measure the shear adhesion force to the electrode under test as indicated in Figure 3-6. In particular, the force required to overcome the adhesion in shear was noted.

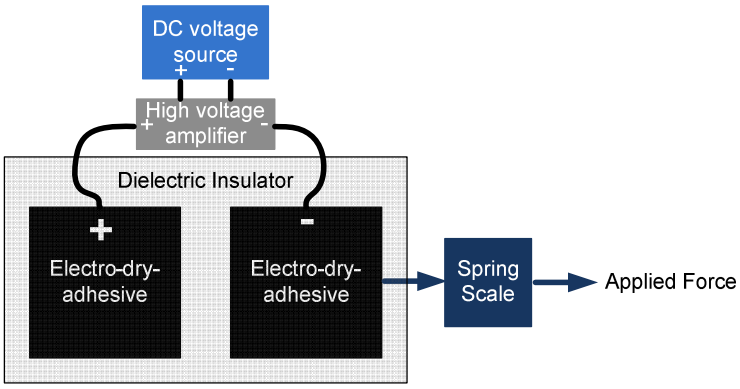

Figure 3-6: Experimental setup used to determine the shear adhesion bond force.

After each test, each of the electrodes was grounded to ensure that most residual charge was removed from the electrodes. From the measured applied force, the shear bond strength was determined by dividing the applied force by the total area of the electrode which was the same in all cases. In Figure 3-7, a comparison is made between the shear adhesion provided by PDMS dry adhesives, flat CB-PDMS and conductive dry adhesives having the same size and concentration of CB under an applied voltage of 2kV (Figure 3-7A) or 4kV (Figure 3-7B). The peak increase in shear bond strength when conductive fibers were used was 400% greater over flat CB-PDMS when tested on drywall, 2360% greater on PP and 2600% greater when tested on PMMA. The respective applied electric fields were 8.1Vμm^{-1}, 36.4Vμm^{-1} and 0.8Vμm^{-1} for an applied voltage of 4kV (Figure 3-7B). The variation in the applied electric field is due to the differing material thicknesses. It should also be noted that the peel strength of the conductive dry adhesives was less than 0.02kPa at all voltages. A careful comparison of both pristine conductive fibers and the PP dielectric layer before and after shear bond strength testing indicate the application of up to 4kV across the electrodes during shear adhesion bond strength measurements did not result in a noticeable change in the either the fiber or dielectric morphology.

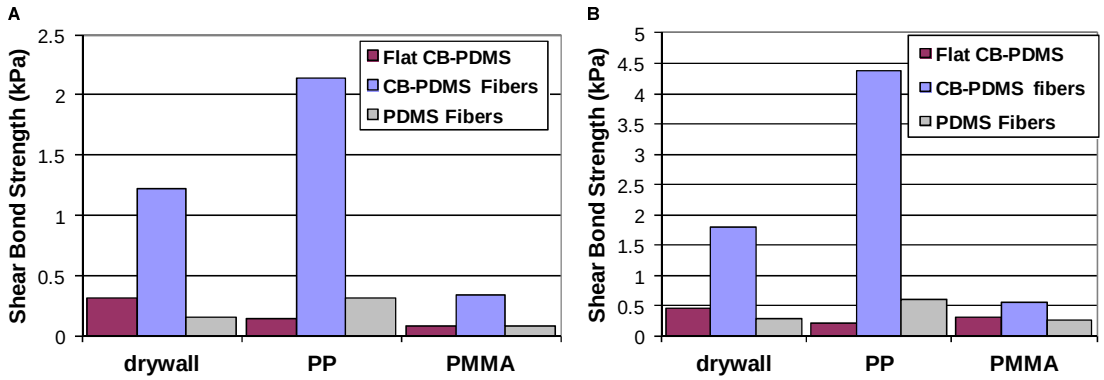

Figure 3-7: The observed increase in shear bond strength of the electrodes to a range of different materials when either A.) 2kV or B.) 4kV was applied to the electrodes. In all cases an increase in shear bond strength was observed for conductive dry adhesive (fibers) samples over flat (no fibers) samples and nonconductive PDMS samples with fibers. All samples were of the same dimensions.

In order to determine if there was a suction effect to shear bond strength due to the shape of the fiber tips as seen previously seen in Figure 3-1, testing was performed at both atmospheric and reduced pressure (-80 kPa) relative to atmospheric pressure in a vacuum chamber (Abbess Instruments). After applying the desired voltage, a linear stepper stage, suitable for use in a vacuum, (Zaber Technologies, T-LS28-SMV) was used to apply a shear force while a spring scale was used to measure the applied shear bond force. The shear adhesion bond strength was then determined as previously from the overall dimensions of the samples under test. Over a minimum of three trials at both atmospheric pressure and reduced pressure there was little noticeable difference in shear adhesion bond strength as can be seen in Figure 3-8.

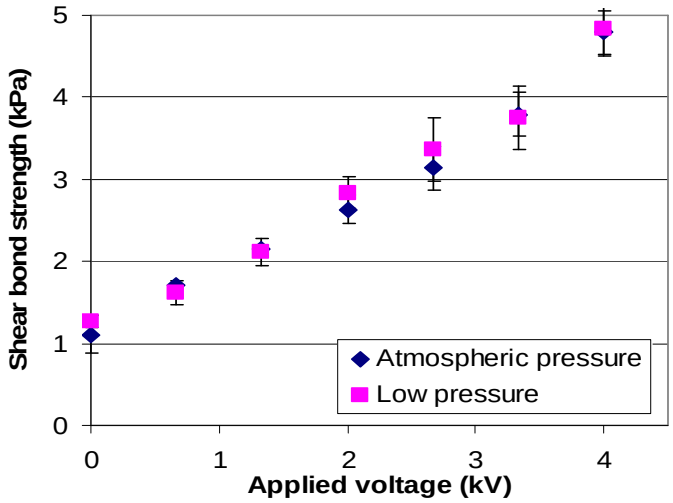

Figure 3-8: Average shear bond strength for the same sample at both atmospheric and reduced (-80 kPa) pressure.

A unique property of biomimetic electro-dry-adhesives is the ability to self-preload. The generation of an electrostatic force by the application of a voltage across the conductive dry adhesive electrodes results in a self-applied preloading mechanism which ensures a large number of individual fibers are in the close contact necessary for van der Waals interactions to occur between each fiber and the attachment substrate. In order to show the ability of electro-dry-adhesion to self-preload, an experimental test was carried out by applying a voltage across two conductive dry adhesives for a total of 60s, followed by grounding the adhesives for a further 60s in order to reduce built up static charge.

Using a high voltage divider (EMCO, V1GR) the dielectric (PP) voltage was measured before during and after the 60s charge/discharge cycle for each applied voltage. Prior to applying a voltage across the sample, 205.5±0.3mV was measured on the back surface of the dielectric material.

Initially upon applying 4kV across the samples, a large spike in voltage was detected on the surface of the dielectric. This spike lasted for less than 0.4s and reached a minimum of -618.210V. This spike in voltage was most likely due to electrons moving across the surface of the dielectric material from the negative electrode towards the surface of the dielectric material near the positive electrode where the measurement was

taken. After reaching a steady state voltage during the 60s charge up time, the average measured voltage on the dielectric was found to 690.3±0.3mV. After grounding the electrodes, another voltage spike was observed. This second spike in voltage reached a maximum of 724.079V and is likely due to the electrons near the positive electrode moving toward the grounded electrodes leaving a concentration of positive charge on the backside of the dielectric material. This second spike lasted for less than 0.6s before a steady state voltage was reached. After reaching a steady state voltage, the average voltage of the dielectric, while it was still grounded, was measure to be 15.3±0.3mV. After grounding the electrodes for a minimum of 60s, a third, much smaller, spike in voltage of -7.932V also lasting for less than 0.4s was measured when the connection to ground was removed from the electrode prior to measuring the shear adhesion bond force. There remained some residual electrostatic voltage across the electrodes after the ground was removed which was measured to be an average of 173.7±0.3mV which is lower than the voltage measured on the dielectric surface before the 60s charge/discharge cycle.

This indicates that by using the 60s charge/discharge cycle we were able to significantly reduce the built up charge on the surface of the dielectric material. However, it is possible that residual charge may still remain on the dielectric material for as long as several days[37]. Figure 3-9 shows the largest two of the three spikes in negative and positive charge measured on the backside of the dielectric material when the samples were first charged (negative spike) and when they were grounded. A much smaller spike was also observed when the connection to ground was removed. Similar results were also observed over a range of applied voltages up to 4kV.

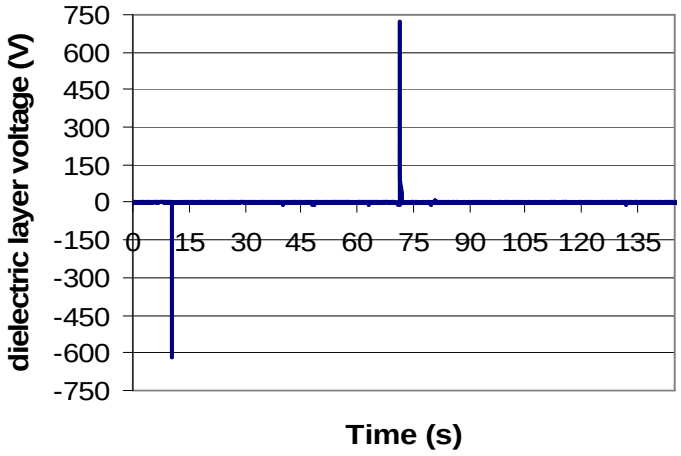

Figure 3-9: Measured dielectric layer voltage during a single 60s charge/discharge cycle. The two large spikes in voltage resulted from the shifting of electrons on the dielectric layer as 4kV was applied to the sample (negative spike) and when the sample was grounded (positive spike).

The average measured shear bond strength from a minimum of three trials that used an electrical field to preload the conductive dry adhesives resulted in an increased shear adhesion bond as shown in Figure 3-10. An average maximum increase in adhesion of 1.8kPa was recorded when a 36.4Vμm^{-1} electric field was applied (and then removed) over tests taken with no applied electric field. The observed increase in adhesion after having applied a voltage across the electrodes is a direct result of the adhesive fibers being preloaded to the surface of the PP. The increased preload enables greater adhesion by forcing the fibers to conform to the substrate surface roughness thus increasing contact surface area for the fiber tips and maximizing van der Waals force. For comparison, Figure 3-10 also shows the average measured shear bond strength when a variety of different masses were used to apply a preload pressure to the same sample. In Figure 3-10 equation 3-2[38] was used to determine the equivalent applied voltage, V_{eq}, based on the pressure, P, applied to the sample

$$V_{eq} = \sqrt{\frac{8P_N t^2}{\varepsilon_0 \varepsilon_r^2}} \qquad \text{Equation 3-2}$$

Where ε_0 is the dielectric permittivity of vacuum, ε_r is the dielectric permittivity of the PP and *t* is the thickness of the PP. Initially, low applied pressures result in lower shear bond strength than seen for self-preloading. This is likely due to preloading at lower applied pressures resulting in fewer fibers being in contact. Electrostatic preloading however results in an even pressure distribution and thus greater shear bond strength for a given voltage. As the applied pressure, related to voltage in Figure 3-10, increases a greater number of fibers are forced into contact which results in similar shear bond strength at 3.33kV for both sets of tests as the number of fibers in contact approaches the total number of fibers.

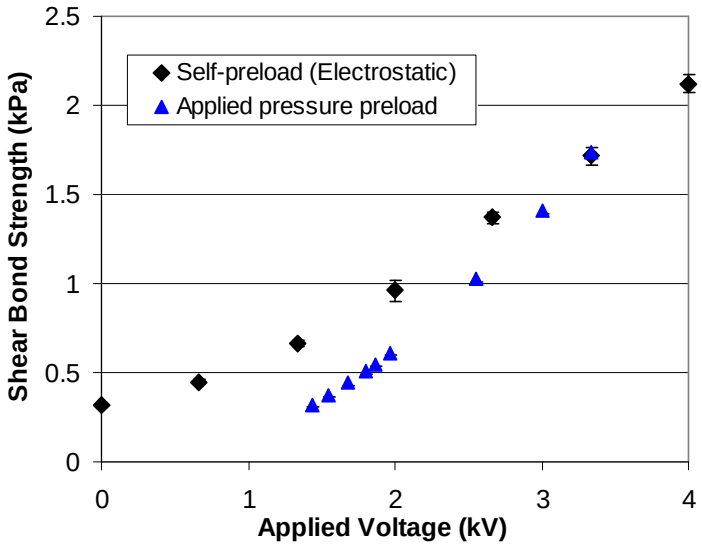

Figure 3-10: Average improvement of the shear bond strength of the self-preloading electro-dry-adhesives. The applied electrostatic force is between the CB-PDMS electrodes and steel with polypropylene (PP) acting as the dielectric insulator and the material to which the CB-PDMS samples are adhering. For comparison, the shear bond strength with respect to the voltage equivalent of the normal applied pressure, converted using equation 3-2, was used to preload the same sample.

3.5. Conclusion

Conductive biomimetic dry adhesives were fabricated by mixing CB and PDMS to form CB-PDMS and curing on a mould. An increased concentration of CB resulted in

an increased material stiffness over that of PDMS which was measured to be 1622±99kPa for PDMS and ranging to 3397±88kPa for CB-PDMS with 24.4% CB. Also, by increasing the concentration of CB within PDMS, the conductivity of CB-PDMS was increased to a maximum of 230Sm^{-1} for 30.7% CB by weight. Conductive dry adhesives acting as electro-dry-adhesives show an increase in shear bond strength ranging from 400% to 2600% over that of flat CB-PDMS when tests were performed on drywall, PP and PMMA under a range of applied electric fields from 0.8$V\mu m^{-1}$ to 36.4$V\mu m^{-1}$. No difference was noted between tests performed at atmospheric pressure and reduced pressure. Lastly, the unique self pre-loading ability of electro-dry-adhesives was confirmed by using electro-adhesion to apply a preload for 60s followed by grounding the electrodes for 60s to reduce any remaining electrostatic effects. The self-preloading provided by electro-dry-adhesion resulted in an average 1.8kPa increase in shear adhesion when applying an electric field of 36.4$V\mu m^{-1}$. In comparison, directly applying a normal pressure preload to the same sample resulted in approximately the same shear bond strength as applying a 3.33kV voltage across the electrodes.

3.6. Acknowledgement

This work was financially supported by the Natural Sciences and Engineering Research Council of Canada (NSERC)

3.7. References

(1) Autumn, K.; Sitti, M.; Liang, Y. A.; Peattie, A. M.; Hansen, W. R.; Sponberg, S.; Kenny, T. W.; Fearing, R.; Israelachvili, J. N.; Full, R. J. Evidence for van Der Waals Adhesion in Gecko Setae. Proc. Natl. Acad. Sci. U. S. A. 2002, 99, 12252–12256.

(2) Jeong, H. E.; Lee, S. H.; Kim, P.; Suh, K. Y. Stretched Polymer Nanohairs by Nanodrawing. Nano Lett. 2006, 6, 1508–1513.

(3) Ho, A. Y. Y.; Yeo, L. P.; Lam, Y. C.; Rodríguez, I. Fabrication and Analysis of Gecko-Inspired Hierarchical Polymer Nanosetae. ACS Nano 2011, 5, 1897–1906.

(4) Davies, J.; Haq, S.; Hawke, T.; Sargent, J. A Practical Approach to the Development of a Synthetic Gecko Tape. Int. J. Adhes. Adhes. 2009, 29, 380–390.

(5) Glassmaker, N. J.; Himeno, T.; Hui, C.-Y.; Kim, J. Design of Biomimetic Fibrillar Interfaces: 1. Making Contact. J. R. Soc. Interface 2004, 1, 23–33.

(6) Sameoto, D.; Menon, C. A Low-Cost, High-Yield Fabrication Method for Producing Optimized Biomimetic Dry Adhesives. J. Micromechanics Microengineering 2009, 19, 115002.

(7) Krahn, J.; Sameoto, D.; Menon, C. Controllable Biomimetic Adhesion Using Embedded Phase Change Material. Smart Mater. Struct. 2011, 20, 015014.

(8) Greiner, C.; Campo, A. Del; Arzt, E. Adhesion of Bioinspired Micropatterned Surfaces: Effects of Pillar Radius, Aspect Ratio, and Preload. Langmuir 2007, 23, 3495–3502.

(9) Varenberg, M.; Gorb, S. Close-up of Mushroom-Shaped Fibrillar Adhesive Microstructure: Contact Element Behaviour. J. R. Soc. Interface 2008, 5, 785–789.

(10) Del Campo, A.; Greiner, C.; Arzt, E. Contact Shape Controls Adhesion of Bioinspired Fibrillar Surfaces. Langmuir 2007, 23, 10235–10243.

(11) Jeong, H. E.; Suh, K. Y. Nanohairs and Nanotubes: Efficient Structural Elements for Gecko-Inspired Artificial Dry Adhesives. Nano Today 2009, 4, 335–346.

(12) Parsaiyan, H.; Barazandeh, F.; Mehdirezaei, S.; Parsaiyan, M.; Safdari, M. Wide-End Fibers and Their Adhesion Performance in Biological Attachment Systems. Int. J. Adhes. Adhes. 2009, 29, 444–450.

(13) Sameoto, D.; Menon, C. Recent Advances in the Fabrication and Adhesion Testing of Biomimetic Dry Adhesives. Smart Mater. Struct. 2010, 19, 103001.

(14) Kwak, M. K.; Pang, C.; Jeong, H.-E.; Kim, H.-N.; Yoon, H.; Jung, H.-S.; Suh, K.-Y. Towards the Next Level of Bioinspired Dry Adhesives: New Designs and Applications. Adv. Funct. Mater. 2011, 21, 3606–3616.

(15) Lee, H.; Lee, B. P.; Messersmith, P. B. A Reversible Wet/dry Adhesive Inspired by Mussels and Geckos. Nature 2007, 448, 338–341.

(16) Mahdavi, A.; Ferreira, L.; Sundback, C.; Nichol, J. W.; Chan, E. P.; Carter, D. J. D.; Bettinger, C. J.; Patanavanich, S.; Chignozha, L.; Ben-Joseph, E.; et al. A Biodegradable and Biocompatible Gecko-Inspired Tissue Adhesive. Proc. Natl. Acad. Sci. U. S. A. 2008, 105, 2307–2312.

(17) Karp, J. M.; Langer, R. Dry Solution to a Sticky Problem. Science (80-.). 2011, 477, 42–43.

(18) Fujigaya, T.; Haraguchi, S.; Fukumaru, T.; Nakashima, N. Development of Novel Carbon Nanotube/Photopolymer Nanocomposites with High Conductivity and Their Application to Nanoimprint Photolithography. Adv. Mater. 2008, 20, 2151–2155.

(19) Cong, H.; Pan, T. Photopatternable Conductive PDMS Materials for Microfabrication. Adv. Funct. Mater. 2008, 18, 1912–1921.

(20) Liu, C.-X.; Choi, J.-W. Patterning Conductive PDMS Nanocomposite in an Elastomer Using Microcontact Printing. J. Micromechanics Microengineering 2009, 19, 085019.

(21) Niu, X. Z.; Peng, S. L.; Liu, L. Y.; Wen, W. J.; Sheng, P. Characterizing and Patterning of PDMS-Based Conducting Composites. Adv. Mater. 2007, 19, 2682–2686.

(22) Segal, E.; Tchoudakov, R.; Narkis, M.; Siegmann, A. Sensing of Liquids by Electrically Conductive Immiscible Polypropylene/thermoplastic Polyurethane Blends Containing Carbon Black. J. Polym. Sci. Part B Polym. Phys. 2003, 41, 1428–1440.

(23) Lu, J.; Lu, M.; Bermak, A.; Lee, Y. Study of Piezoresistance Effect of Carbon Nanotube-PDMS Composite Materials for Nanosensors. In Procedings of the 7th IEEE Iternational Conference on Nanotechnology August 2-5, 2007, Hong Kong; 2007; pp. 1240–1243.

(24) Buckley, H. F. A Short History of Physics; D. Van Nostrand Company, Inc.: New York, 1927.

(25) Monkman, G. Electroadhesive Microgrippers. Ind. Robot An Int. J. 2003, 30, 326–330.

(26) Monkman, G. J. Robot Grippers for Use With Fibrous Materials. Int. J. Rob. Res. 1995, 14, 144–151.

(27) Monkman, G. J.; Taylor, P. M.; Farnworth, G. J. Principles of Electroadhesion in Clothing Robotics. Int. J. Cloth. Sci. Technol. 1989, 1, 14–20.

(28) Shim, G. Il; Sugai, H. Dechuck Operation of Coulomb Type and Johnsen-Rahbek Type of Electrostatic Chuck Used in Plasma Processing. Plasma Fusion Res. 2008, 3, 051–1 – 051–054.

(29) Yoo, J.; Choi, J.; Hong, S.; Kim, T.; Lee, S. J. Finite Element Analysis of the Attractive Force on a Coulomb Type Electrostatic Chuck. In International Conference on Electrical Machines and Systems; Seoul, 2007; pp. 1371–1375.

(30) Asano, K.; Hatakeyama, F.; Yatsuzuka, K. Fundamental Study of an Electrostatic Chuck for Silicon Wafer Handling. IEEE Trans. Ind. Appl. 2002, 38, 840–845.

(31) Prahlad, H.; Pelrine, R.; Stanford, S.; Marlow, J.; Kornbluh, R. Electroadhesive Robots -— Wall Climbing Robots Enabled by a Novel, Robust, and Electrically Controllable Adhesion Technology. In IEEE International Conference on Robotics and Automation; Pasadena, CA, 2008; pp. 3028–3033.

(32) Yamamoto, A.; Nakashima, T.; Higuchi, T. Wall Climbing Mechanisms Using Electrostatic Attraction Generated by Flexible Electrodes. In International Symposium on Micro-NanoMechatronics and Human Science; Nagoya, Japan, 2007; pp. 389–394.

(33) Pelrine, R. E.; Prahlad, H.; Kornbluh, R. D.; Lincoln, P. D.; Stanford, S. Wall Climbing Robots. United States Patent, No. US 7872850 B2 2011.

(34) Santiago, D.; Rodríguez-Calero, G. G.; Rivera, H.; Tryk, D. a.; Scibioh, M. A.; Cabrera, C. R. Platinum Electrodeposition at High Surface Area Carbon Vulcan-XC-72R Material Using a Rotating Disk-Slurry Electrode Technique. J. Electrochem. Soc. 2010, 157, F189.

(35) Jaeger, R. C. Introduction to Microelectronic Fabrication; Nuedeck, G. W.; Pierret, R. F., Eds.; Second.; Prentice Hall: Upper Saddle River, New Jersey, 2002.

(36) Du Roure, O.; Saez, A.; Buguin, A.; Austin, R. H.; Chavrier, P.; Silberzan, P.; Siberzan, P.; Ladoux, B. Force Mapping in Epithelial Cell Migration. Proc. Natl. Acad. Sci. U. S. A. 2005, 102, 2390–2395.

(37) Lima Burgo, T. A. De; Rezende, C. A.; Bertazzo, S.; Galembeck, A.; Galembeck, F. Electric Potential Decay on Polyethylene: Role of Atmospheric Water on Electric Charge Build-up and Dissipation. J. Electrostat. 2011, 69, 401–409.

(38) Karagozler, M. E.; Campbell, J. D.; Fedder, G. K.; Goldstein, S. C.; Weller, M. P.; Yoon, B. W. Electrostatic Latching for Inter-Module Adhesion, Power Transfer, and Communication in Modular Robots. In 2007 IEEE/RSJ International Conference on Intelligent Robots and Systems; Ieee: San Diego, CA, 2007; pp. 2779–2786.

Chapter 4. Polymeric electro-dry-adhesives for use on conducting surfaces

The content of this chapter has been slightly modified from what first appeared in print in:

Krahn, J M, Pattantyus-Abrahams, A G and Menon, C. Polymeric electro-dry-adhesives for use on conducting surfaces. *Proceedings of the institute of mechanical engineers part L: Journal of materials: Design and Applications* 2013, DOI: 10.1177/1464420713509376

4.1. Abstract

This work presents electro-dry-adhesives, designed for use on conducting surfaces, that synergistically combine biomimetic dry adhesives with mushroom-like fibres and embedded conductive polymer electrodes. Together, the dry adhesive surface and electrodes enable the electro-dry-adhesives to generate greatly improved shear adhesion bond strengths. The electro-dry-adhesives described in this work are fabricated with a poly(dimethylsiloxane) (PDMS) biomimetic dry adhesive surface and embedded interdigitated electrodes manufactured from a carbon black and PDMS composite conductive polymer. The PDMS dry adhesive layer allows the electro-dry-adhesives to be used both passively and actively and the PDMS acts as a dielectric insulator between the electrodes and enables the electro-dry-adhesive to be used on conducting surfaces. In order to compare both the passive and active use of the electro-dry-adhesives, shear adhesion bond strength is measured and compared with voltage potentials from 0 kV up to 3 kV applied across the electrodes with up to a 2.56 times increase in shear adhesion bond strength. The increase in shear adhesion bond strength due to the generation of an induced electrostatic attractive force is compared to the theoretical maximum shear adhesion bond strength at each of the voltages applied.

4.2. Introduction

The primary attachment force mechanism which allows geckos' to climb walls are thought to be Van der Waals' interactions[1] and interest in climbing robots has lead to a growing number of researchers finding new and innovative ways to mimic the setae and spatulae found on the foot pads of the gecko. Synthetic adhesives which rely on Van der Waals' forces are often termed biomimetic dry adhesives. Among the methods used by researchers to fabricate dry adhesives, whether directly or through indirect means such as casting, are moulding of poly(dimethylsiloxane) (PDMS)[2–4], plasma etching[5], nanodrawing[6] and nanoimprinting[7] among others. Common methods of further increasing adhesion include optimizing the aspect ratio, the shape, size and overhang of the mushroom-like cap[8–11] or increasing the density of fibres while reducing the fibre diameter and the spacing between fibres[12,13]. Adapting the stiffness of the backing layer[4,14] and creating hierarchical fibres[15,16] allow dry adhesives to better conform to a surface and increases adhesion to a rough surface. Medically suitable [17,18] or moist environment compatible[19] versions have also been explored.

Interest in conductive polymers has also been increasing steadily with most conductive polymers being fabricated by mixing micro- or nanoscale conductive particles such as silver[20,21], carbon nanotubes[22–24] or carbon black[20,21,25] into various polymers such as PDMS[20,21,23], polypropylene, polyurethanes[25] and UV curable monomers[22]. The overall conductivity of the resulting polymers is determined by the weight percentage of conductive particles within the composite polymer-particle mix. Interest in conductive polymers has been driven largely by interest in flexible circuits[21], sensing of liquids[25] and recently, electro-dry-adhesives[26].

Documented research on electrostatics dates back to the 1700's[27] and continues to be an active area of research with interest in clothing manufacturing[28,29], robot grippers[30], electrostatic chucks and latching[31–34], climbing robots[35–37], and electro-dry-adhesives[26] among others.

Our previous work[26] on electro-dry-adhesives focused on the shear adhesion bond strength of an electro-dry-adhesive device having only a single electrode. A second, separate, electro-dry-adhesive was present but remained stationary during testing and was required to maximize the induced electrostatic force. The shear adhesion bond strength was measured on several different non-conducting surfaces because the entire electro-dry-adhesive sample was conductive[26] and a short-circuit condition did not allow for use on conducting surfaces. Adhesion tests were performed on several different materials to provide a relative comparison of adhesion strength.

The work described within this article explores the shear adhesion bond strength of electro-dry-adhesives designed to be used on conducting surfaces. The electro-dry-adhesives described in this article are fabricated from PDMS with embedded composite electrodes fabricated with carbon black (CB) embedded in PDMS (CB-PDMS) that ensure a dielectric layer remains between the electrodes and a conducting surface. The presence of a dielectric insulating layer ensures that the electro-dry-adhesives may be used on metallic or conducting surfaces. By incorporating interdigitated electrodes onto a single electro-dry-adhesive sample we were able to combine both a positive and negative electrode onto a single device which could be easily scaled in size to make it suitable for climbing robots or similar uses.

4.3. Methods and Materials

In this work, conductive biomimetic dry adhesives were manufactured in a multi-step process. Firstly, biomimetic dry adhesive moulds were fabricated as previously described[4,26,38]. Starting with a 100 mm diameter poly(methyl methacrylate) (PMMA) wafer, the wafer was thoroughly rinsed with de-ionized water (DI water), dried under a stream of N_2 gas and finally placed in a 100 ^{o}C thermal chamber for 1 min to remove any remaining water droplets. After allowing the wafer to cool, a spinner was used to apply an approximately 2 µm thick layer of polydimethylglutarimide resist (PMGI, MicroChem). After allowing the wafer to again cool after performing a pre-exposure bake for 1 min. at

90 ^{o}C, an approximately 10 µm thick layer of AZ 9260 resist resist (AZ Electronic Materials) was spin coated over the PMGI. Once again a prebake was performed, but this time for 60 min at 80 ^{o}C in a thermal chamber. After allowing the wafers to again cool, they were placed in a DI water bath for 30 min in order to rehydrate the resists before exposure to i-line UV light. After exposing to UV light, a post exposure bake was performed for 90 s at 100 ^{o}C. Then, after allowing the wafer to cool, AZ 400K developer mixed with DI water in a 1:4 ratio by volume was used to develop the resist. In order to achieve the mushroom-like overhanging cap, the PMGI layer was overdeveloped until the desired undercut was achieved. After development, the wafers were allowed to sit for a minimum of 4 hours before PDMS (Sylgard 184), mixed in a 10:1 ratio of pre-polymer to catalyst by weight was spread over the surface of the mould with a spinner after having been degassed in a vacuum chamber. Upon curing, a mask was applied to the upper surface of the PDMS, still on the mould, and a mixture of Carbon Black (Vulcan XC-72R) and PDMS (CB-PDMS) was spread over the mask and the cured PDMS. The addition of CB to PDMS, in a mixture of 20% CB by weight, resulted in conductive PDMS. The mask allowed the CB-PDMS to be patterned into interdigitated electrodes and was removed prior to curing the CB-PDMS. After curing, 22 gauge wires were stretched over the surface of the two larger electrodes from which the interdigitated electrodes extended. After spreading a thin layer of CB-PDMS over the wires, the wafer, CB-PDMS and wires were all placed in a thermal chamber to cure the CB-PDMS. Finally, uncured PDMS was spread over the surface of the electrodes and cured for 3 hours at 80 ^{o}C before the final electro-dry-adhesive was removed from the mould. The fabrication of the electro-dry-adhesive device is shown in Figure 4-1.

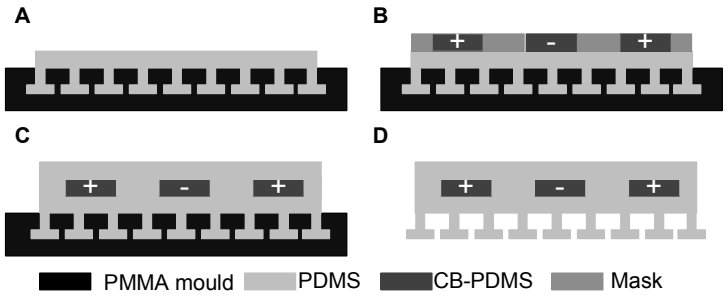

Figure 4-1: Fabrication of the electro-dry-adhesive. A. PDMS is spread over the surface of a mould with micro-scale features and allowed to cure. B. Scotch tape is applied to the surface of the cured PDMS and acts a mask as CB-PDMS is spread over the surface of the mask and PDMS to form the electrodes. The mask material is removed prior to curing leaving CB-PDMS electrodes. C. PDMS is spread over the surface of the sample and encapsulates the CB-PDMS electrodes. D. After curing, the electro-dry-adhesive is removed from the mould and is ready for use.

Using the previously mentioned fabrication method, the mushroom-like fibres on the surface of the electro-dry-adhesive were 15.2 µm in diameter and 12 µm tall. The overall area of the electro-dry-adhesive was 5075 mm^2 and the total area of the electrodes was 2025 mm^2. Each of the interdigitated electrodes average 2.5 mm wide with an average 2.5 mm wide gap between electrodes. The resulting electro-dry-adhesive had an average of one electrode per 507.5 mm^2. The PDMS layer thickness between the electrodes and the surface of the mushroom caps was 100 µm while the electro-dry-adhesive sample was approximately 600 µm thick. Images of the micro-scale mushroom-like fibres can be seen in Figure 4-2.

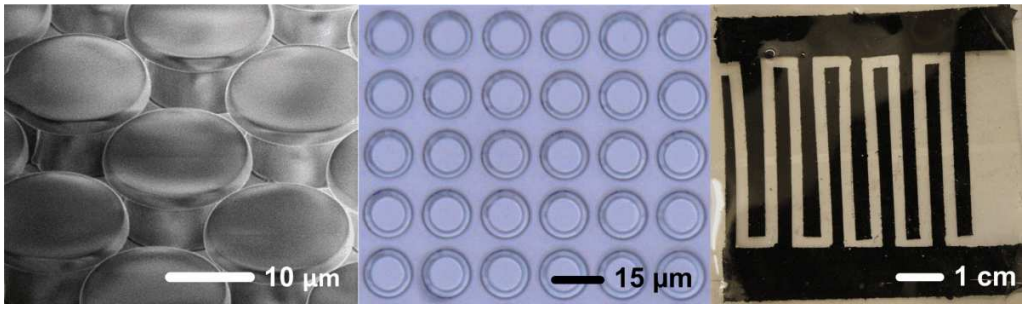

Figure 4-2: A. Scanning Electron Microscope (SEM) image of the surface of the micro-scale electro-dry-adhesive fibres. B. Microscope image of the surface of the of the micro-scale electro-dry-adhesive fibres. The inner circles represent the area of the supporting post and the outer ring represents the overhanging mushroom-like cap. C. Top-view of the fabricated electro-dry-adhesive sample showing the interdigitated electrodes.

In order to test the shear adhesion bond strength of the electro-dry-adhesives, a linear stage (Zaber Technologies, T-LS28-SMV[39]) and load cell (Futek, LRF 400[40]) were used to apply and measure the shear adhesion force. Custom LabView software, developed within our lab, was used to control the speed, distance and direction of the linear stage while recording the shear adhesion force measured by the load cell. Up to 3kV was applied to the electrodes of the electro-dry-adhesive with the assistance of an EMCO (model E101CT) DC-DC voltage convertor. The application of a high voltage potential across the electrodes of the electro-dry-adhesive induced an electrostatic attractive force between the electro-dry-adhesive and the gold-coated surface of a silicon wafer. A diagram of the test setup can be found in Figure 4-3.

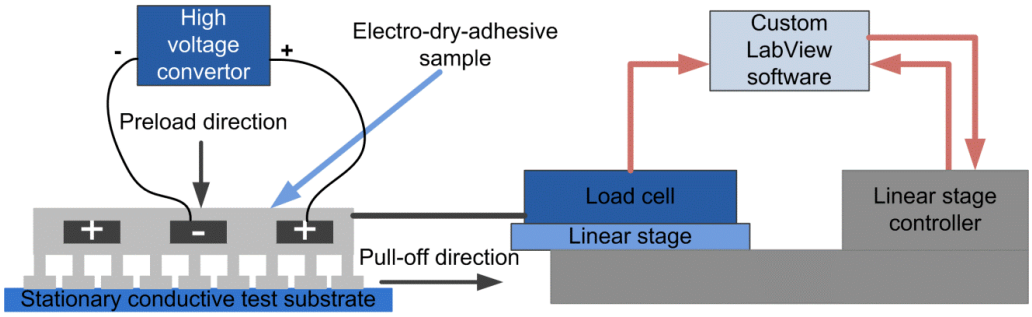

Figure 4-3: Diagram of the setup used to measure the shear adhesion bond strength. During testing the sample was first preloaded with a 5.1 N force in the vertical direction before applying a voltage across the electrodes of the sample for a minimum of 10 s. After grounding the electrodes, the linear stage was used to apply a force in the horizontal direction as the load cell recorded the applied shear force. The speed and direction of the linear stage were controlled by the custom LabView software while at the same time recording the applied shear force to the sample.

Prior to each trial, a 5.1N preloading force was applied to the surface of the electro-dry-adhesive. At the same time, a voltage was applied across the electrodes for a minimum of 10 sec in order to ensure that the electro-dry-adhesive was consistently preloaded throughout all trials by both a preloading force and the electrostatic attractive force generated by the electrodes. After removing the 5.1N preload, turning off the voltage applied to the electrodes and grounding them, the linear stage was activated and the shear adhesion bond strength was measured. During each trial, the speed of the linear stage was set to 100µm-sec^{-1} and the linear stage continued to apply a shear force to the electro-dry-adhesive until after the shear adhesion bond had been broken.

The theoretical maximum normal adhesion pressure, P_{normal} can be estimated from[34]:

$$P_{normal} = \frac{\varepsilon_o \varepsilon_r^2 V^2}{8d^2} \qquad \text{Equation 4-1}$$

Where V is the applied voltage, d is the thickness of the dielectric layer as shown in Figure 4-4, ε_o is the dielectric permittivity of vacuum and ε_r is relative permittivity of the

dielectric coating. In order to compare the maximum theoretical normal adhesion pressure with the measured shear adhesion pressure, P_{shear}, the following relationship can be used:

$$P_{shear} = \mu P_{normal} \qquad \text{Equation 4-2}$$

Where μ is the friction coefficient between the electro-dry-adhesive and the gold-coated silicon wafer which served as the conducting surface.

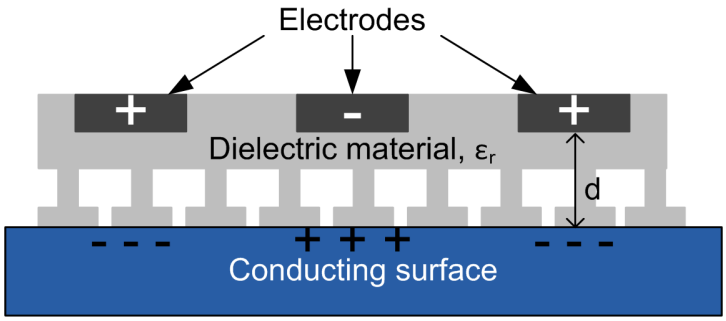

Figure 4-4: Diagram showing the interface between the electro-dry-adhesive and a conducting surface.

4.4. Results and discussion

During the shear adhesion bond strength testing of the electro-dry-adhesive, a minimum of 10 trials were performed with 0kV, 1kV, 2kV and 3kV applied across the interdigitated electrodes of the electro-dry-adhesive sample. When voltages greater than 3kV were applied, the PDMS dielectric layer was overcome and voltage breakdown occurred resulting in a short-circuit condition between the electrodes and the conducting test substrate. During a short-circuit condition, the lack of a charge building up on the dielectric resulted in the loss of the electrostatic attraction force.

In order to be able to determine the effect of the application of a high voltage across the electrodes of the electro-dry-adhesive sample, shear adhesion bond strength tests were performed without a voltage applied. The 0kV tests were used to determine

the friction coefficient between the electro-dry-adhesive and the conducting surface by measuring the shear adhesion bond strength. Since no voltage was being applied to the electrodes, the normal force is due entirely to the 5.1N preload and equation 4-2 was used to estimate the friction coefficient based on the normal pressure being applied and the measured shear adhesion bond strength. The average shear adhesion bond strength was measured to be 0.89 ± 0.17 kPa and the coefficient of friction, μ, was calculated to be 0.46 ± 0.05.

Under an applied voltage of 1 kV, the average shear adhesion bond strength was measured to be 1.27 ± 0.16 kPa which was an average increase of 0.38 kPa or 1.43 times over the tests performed without a voltage applied.

When 2 kV was applied across the electrodes, the average shear adhesion bond strength was 1.74 ± 0.31 kPa which resulted in an increase in the average shear adhesion bond strength of 0.85 kPa or 1.96 times. Lastly, with an applied voltage of 3 kV across the electrodes, the average shear adhesion bond strength was measured to be 2.30 ± 0.37 kPa which corresponds to an increase in shear adhesion bond strength due to the electrostatic forces of 1.41 kPa or 2.56 times. Figure 4-5 shows the average measured shear adhesion bond strength at different applied voltages while Table 4-1 summarizes the measured and theoretical shear adhesion values.

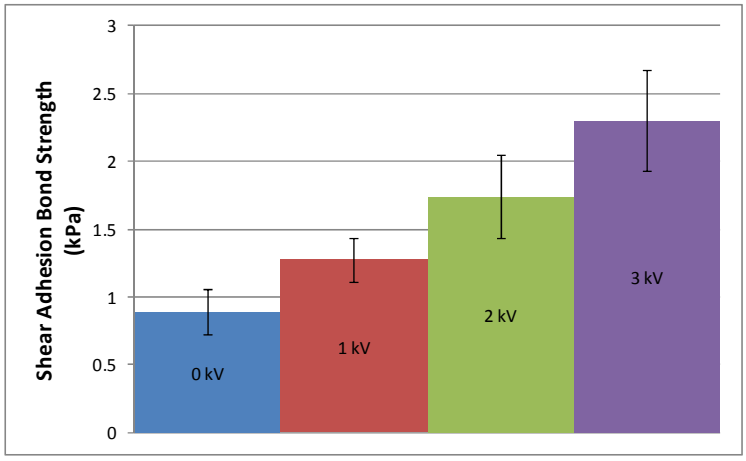

Figure 4-5: Measured shear adhesion bond strength with several different voltages applied across the electrodes. A minimum of ten trials was performed at each voltage and the error bars indicate the standard deviation in the measurements taken at each voltage.

In order to compare the measured increase in shear adhesion bond strength due to the induced electrostatic forces, the average shear adhesion bond strength with 0 kV applied across the electrodes was subtracted from each of the shear bond strength measurements taken with 1 kV, 2 kV or 3kV applied across the electrodes. Using equation 4-1 and equation 4-2, the theoretical maximum shear bond strength was estimated and a comparison between the measured and theoretical shear adhesion bond strength is summarized in Table 4-1 and is shown in Figure 4-6. The measured shear adhesion bond strength at 2 kV was 66% of the theoretical value and the 3 kV was 49% of the theoretical value. The observed difference between the theoretical and measured values is most likely due to variations in the thickness of the dielectric layer (±15 µm), an inability of the electro-dry-adhesive to completely conform to the surface of the gold-coated silicon wafer and voltage losses along the length of the CB-PDMS electrodes since there is some resistance (approximately 135kΩ) along their length.

Table 4-1: Summary of measured and theoretical shear adhesion bond strength

Applied Voltage [kV]	Theoretical [kPa]	Measured [kPa]	Measurement Error [kPa]
0	0	0	.17
1	.32	.39	.16
2	1.28	.85	.31
3	2.88	1.41	0.37

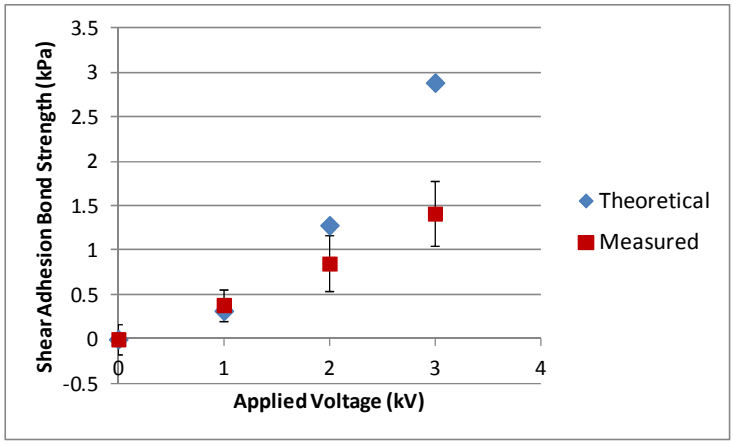

Figure 4-6: Comparison between the theoretical maximum calculated shear adhesion bond strength and the actual measured shear adhesion bond strength. The difference between the two at higher voltages are likely due to variations across the sample in the thickness of the dielectric layer and the inability of the electro-dry-adhesive sample to conform to the surface of the gold-coated silicon wafer and voltage losses along the length of the CB-PDMS electrodes.

4.5. Conclusion

In conclusion, electro-dry-adhesives with embedded interdigitated CB-PDMS electrodes and biomimetic mushroom-like micro-scale fibres were fabricated with PDMS and designed for use on conductive surfaces. Shear adhesion bond strength measurements were performed with voltages between 0 kV and 3 kV applied across the electrodes of the electro-dry-adhesive. The average shear adhesion bond strength with

0 kV applied across the electrodes was measured to be 0.89 ± 0.17 kPa. With 1 kV applied across the electrodes the shear adhesion bond strength was measured to be 1.27 ± 0.16 kPa which was an increase of 0.38 kPa over the shear adhesion bond strength. For shear adhesion bond strength trials with 3 kV and 4 kV applied across the electrodes the shear bond strength increased to 1.74 ± 0.31 kPa and 2.30 ± 0.37 kPa respectively which is an increase in shear bond strength of 0.85 kPa and 1.41 kPa respectively over that measured with 0 kV applied across the electrodes.

4.6. Acknowledgment

This work was financially supported by The Natural Sciences and Engineering Research Council of Canada (NSERC)

4.7. References

(1) Autumn, K.; Sitti, M.; Liang, Y. A.; Peattie, A. M.; Hansen, W. R.; Sponberg, S.; Kenny, T. W.; Fearing, R.; Israelachvili, J. N.; Full, R. J. Evidence for van Der Waals Adhesion in Gecko Setae. Proc. Natl. Acad. Sci. U. S. A. 2002, 99, 12252–12256.

(2) Glassmaker, N. J.; Himeno, T.; Hui, C.-Y.; Kim, J. Design of Biomimetic Fibrillar Interfaces: 1. Making Contact. J. R. Soc. Interface 2004, 1, 23–33.

(3) Sameoto, D.; Menon, C. A Low-Cost, High-Yield Fabrication Method for Producing Optimized Biomimetic Dry Adhesives. J. Micromechanics Microengineering 2009, 19, 115002.

(4) Krahn, J.; Sameoto, D.; Menon, C. Controllable Biomimetic Adhesion Using Embedded Phase Change Material. Smart Mater. Struct. 2011, 20, 015014.

(5) Davies, J.; Haq, S.; Hawke, T.; Sargent, J. A Practical Approach to the Development of a Synthetic Gecko Tape. Int. J. Adhes. Adhes. 2009, 29, 380–390.

(6) Jeong, H. E.; Lee, S. H.; Kim, P.; Suh, K. Y. Stretched Polymer Nanohairs by Nanodrawing. Nano Lett. 2006, 6, 1508–1513.

(7) Ho, A. Y. Y.; Yeo, L. P.; Lam, Y. C.; Rodríguez, I. Fabrication and Analysis of Gecko-Inspired Hierarchical Polymer Nanosetae. ACS Nano 2011, 5, 1897–1906.

(8) Varenberg, M.; Gorb, S. Close-up of Mushroom-Shaped Fibrillar Adhesive Microstructure: Contact Element Behaviour. J. R. Soc. Interface 2008, 5, 785–789.

(9) Del Campo, A.; Greiner, C.; Arzt, E. Contact Shape Controls Adhesion of Bioinspired Fibrillar Surfaces. Langmuir 2007, 23, 10235–10243.

(10) Jeong, H. E.; Suh, K. Y. Nanohairs and Nanotubes: Efficient Structural Elements for Gecko-Inspired Artificial Dry Adhesives. Nano Today 2009, 4, 335–346.

(11) Parsaiyan, H.; Barazandeh, F.; Mehdirezaei, S.; Parsaiyan, M.; Safdari, M. Wide-End Fibers and Their Adhesion Performance in Biological Attachment Systems. Int. J. Adhes. Adhes. 2009, 29, 444–450.

(12) Greiner, C.; Campo, A. Del; Arzt, E. Adhesion of Bioinspired Micropatterned Surfaces: Effects of Pillar Radius, Aspect Ratio, and Preload. Langmuir 2007, 23, 3495–3502.

(13) Ahmadi, S.; Menon, C. A New Model for Predicting Fiber Clumping Phenomenon in Bio-Inspired Dry Adhesives. J. Adhes. 2012.

(14) Greiner, C.; Buhl, S.; del Campo, A.; Arzt, E. Experimental Parameters Controlling Adhesion of Biomimetic Fibrillar Surfaces. J. Adhes. 2009, 85, 646–661.

(15) Sameoto, D.; Menon, C. Recent Advances in the Fabrication and Adhesion Testing of Biomimetic Dry Adhesives. Smart Mater. Struct. 2010, 19, 103001.

(16) Kwak, M. K.; Pang, C.; Jeong, H.-E.; Kim, H.-N.; Yoon, H.; Jung, H.-S.; Suh, K.-Y. Towards the Next Level of Bioinspired Dry Adhesives: New Designs and Applications. Adv. Funct. Mater. 2011, 21, 3606–3616.

(17) Mahdavi, A.; Ferreira, L.; Sundback, C.; Nichol, J. W.; Chan, E. P.; Carter, D. J. D.; Bettinger, C. J.; Patanavanich, S.; Chignozha, L.; Ben-Joseph, E.; et al. A Biodegradable and Biocompatible Gecko-Inspired Tissue Adhesive. Proc. Natl. Acad. Sci. U. S. A. 2008, 105, 2307–2312.

(18) Karp, J. M.; Langer, R. Dry Solution to a Sticky Problem. Science (80-.). 2011, 477, 42–43.

(19) Lee, H.; Lee, B. P.; Messersmith, P. B. A Reversible Wet/dry Adhesive Inspired by Mussels and Geckos. Nature 2007, 448, 338–341.

(20) Cong, H.; Pan, T. Photopatternable Conductive PDMS Materials for Microfabrication. Adv. Funct. Mater. 2008, 18, 1912–1921.

(21) Niu, X. Z.; Peng, S. L.; Liu, L. Y.; Wen, W. J.; Sheng, P. Characterizing and Patterning of PDMS-Based Conducting Composites. Adv. Mater. 2007, 19, 2682–2686.

(22) Fujigaya, T.; Haraguchi, S.; Fukumaru, T.; Nakashima, N. Development of Novel Carbon Nanotube/Photopolymer Nanocomposites with High Conductivity and Their Application to Nanoimprint Photolithography. Adv. Mater. 2008, 20, 2151–2155.

(23) Liu, C.-X.; Choi, J.-W. Patterning Conductive PDMS Nanocomposite in an Elastomer Using Microcontact Printing. J. Micromechanics Microengineering 2009, 19, 085019.

(24) Lu, J.; Lu, M.; Bermak, A.; Lee, Y. Study of Piezoresistance Effect of Carbon Nanotube-PDMS Composite Materials for Nanosensors. In Procedings of the 7th IEEE Iternational Conference on Nanotechnology August 2-5, 2007, Hong Kong; 2007; pp. 1240–1243.

(25) Segal, E.; Tchoudakov, R.; Narkis, M.; Siegmann, A. Sensing of Liquids by Electrically Conductive Immiscible Polypropylene/thermoplastic Polyurethane Blends Containing Carbon Black. J. Polym. Sci. Part B Polym. Phys. 2003, 41, 1428–1440.

(26) Krahn, J.; Menon, C. Electro-Dry-Adhesion. Langmuir 2012, 28, 5438–5443.

(27) Moore, A. D. Introduction. In Electrostatics and its applications; Moore, A. D., Ed.; John Wiley & Sons: Toronto, 1973.

(28) Monkman, G. J. Robot Grippers for Use With Fibrous Materials. Int. J. Rob. Res. 1995, 14, 144–151.

(29) Monkman, G. J.; Taylor, P. M.; Farnworth, G. J. Principles of Electroadhesion in Clothing Robotics. Int. J. Cloth. Sci. Technol. 1989, 1, 14–20.

(30) Monkman, G. Electroadhesive Microgrippers. Ind. Robot An Int. J. 2003, 30, 326–330.

(31) Shim, G. Il; Sugai, H. Dechuck Operation of Coulomb Type and Johnsen-Rahbek Type of Electrostatic Chuck Used in Plasma Processing. Plasma Fusion Res. 2008, 3, 051–1 – 051–054.

(32) Yoo, J.; Choi, J.; Hong, S.; Kim, T.; Lee, S. J. Finite Element Analysis of the Attractive Force on a Coulomb Type Electrostatic Chuck. In International Conference on Electrical Machines and Systems; Seoul, 2007; pp. 1371–1375.

(33) Asano, K.; Hatakeyama, F.; Yatsuzuka, K. Fundamental Study of an Electrostatic Chuck for Silicon Wafer Handling. IEEE Trans. Ind. Appl. 2002, 38, 840–845.

(34) Karagozler, M. E.; Campbell, J. D.; Fedder, G. K.; Goldstein, S. C.; Weller, M. P.; Yoon, B. W. Electrostatic Latching for Inter-Module Adhesion, Power Transfer, and Communication in Modular Robots. In 2007 IEEE/RSJ International Conference on Intelligent Robots and Systems; Ieee: San Diego, CA, 2007; pp. 2779–2786.

(35) Prahlad, H.; Pelrine, R.; Stanford, S.; Marlow, J.; Kornbluh, R. Electroadhesive Robots -— Wall Climbing Robots Enabled by a Novel, Robust, and Electrically Controllable Adhesion Technology. In IEEE International Conference on Robotics and Automation; Pasadena, CA, 2008; pp. 3028–3033.

(36) Yamamoto, A.; Nakashima, T.; Higuchi, T. Wall Climbing Mechanisms Using Electrostatic Attraction Generated by Flexible Electrodes. In International Symposium on Micro-NanoMechatronics and Human Science; Nagoya, Japan, 2007; pp. 389–394.

(37) Pelrine, R. E.; Prahlad, H.; Kornbluh, R. D.; Lincoln, P. D.; Stanford, S. Wall Climbing Robots. United States Patent, No. US 7872850 B2 2011.

(38) Krahn, J.; Liu, Y.; Sadeghi, A.; Menon, C. A Tailless Timing Belt Platform (TBCP-II) Utilizing Dry Adhesives with Mushroom Caps. Smart Mater. Struct. 2011, 20, 11.

(39) Zaber Technologies. Motorized Linear Stages with Built-in Controllers http://www.zaber.com/products/product_group.php?group=T-LS&name=Motorized_Linear_Stage (accessed Oct 11, 2013).

(40) Futek. Tension and Compression Load Cell http://www.futek.com/search.aspx?ws=0&q=lrf400 (accessed Oct 11, 2013).

Chapter 5. Magnetic field switchable dry adhesives

The content of this chapter has been slightly modified from what was originally submitted for publication

> **Krahn J.**, Bovero E., and Menon C. (in press) Magnetic field switchable dry adhesives. Submitted August 1, 2014

5.1. Abstract

A magnetic field controllable dry adhesive device is manufactured. The normal adhesion force can be increased or decreased depending on the presence of an applied magnetic field. If the magnetic field is present during the entire normal adhesion test cycle which includes both applying a preloading force and measuring the pulloff pressure, a decrease in adhesion is observed when compared to when there is no applied magnetic field. Similarly, if the magnetic field is present only during the preload portion of the normal adhesion test cycle, a decrease in adhesion is observed due to an increased stiffness of the magnetically controlled dry adhesive device. When the applied magnetic field is present during only the pulloff portion of the normal adhesion test cycle, either an increase or decrease in normal adhesion is observed depending on the direction of the applied magnetic field.

5.2. Introduction

Since 2000, when evidence that van der Waals' interactions were the main contributors to gecko adhesion force was discovered[1,2], a great number of research groups have spent considerable effort in fabricating synthetic gecko adhesives. The ability of geckos' to adhere to a wide variety of surfaces has inspired researchers to develop synthetic gecko tape which also relies mainly on van der Waals' forces for

adhesion. The first attempts at producing synthetic gecko tape were performed by nanoindenting followed by the moulding of Poly(dimethyl siloxane) (PDMS) in nanoindented cavities[3]. Other fabrication techniques for producing biomimetic dry adhesive fibres soon followed and include electron beam lithography[4], plasma etching[5], photolithography[6,7] and moulding PDMS using commercially available mesh[8]. While some groups have concentrated their efforts on developing new fabrication techniques that allow increased fibre density[9] other researchers have examined the effect of fibre tip shape[10,11], fibre aspect ratio and the addition of an overhanging cap[12–15]. While still others have tried to mimic the structures found on geckos by developing hierarchical structures[16,17] which increases the ability of the gecko fibres to conform to a surface.

Other approaches to increasing adhesion have been presented such as the synergistic combination of electrostatics and gecko tape where embedded particles[24,25] or chemically etched mesh[26] were used as electrodes to generate electrostatic forces. Still other researchers have embedded magnets onto the ends of large macro-scale polymer fibres[27] or dispersed carbonyl iron particles in a PDMS network to form magnetically actuated gecko microridges[28] or beams[29].

In the meantime, another approach to increasing adhesion has been to change the stiffness of the backing layer to resist peeling as described in our earlier work[18] where a phase change material was used to conform to the surface of a spherical probe when in the softer phase but, resist peeling when in a hardened phase. Switchable adhesion has also been achieved with thermally controlled shape memory polymers being used as either a backing layer[19] or for bending the fibres themselves[20]. Switchable adhesion has also been shown through the use of microchannels[21] within a backing layer, contact surface area decrease through a thin film surface collapse[22] or by surface wrinkling[23].

Recently, several research groups have studied the effect of magnetorheological elastomers (MRE) made from PDMS and carbonyl iron particles. In the presence of a magnetic field, the MRE show an increase in shear modulus as the intensity of the magnetic field increases[30,31] and a theoretical model explaining the change in the modulus of MRE due to the presence of a magnetic field has been developed[32,33]. Other recent work on magnetically controlled elastomers includes a magnetic microfluidic mixer where the magnetic elastomer was used as a magnetically controllable valve[34].

In this study, a magnetically controlled dry adhesive device is fabricated by dispersing iron oxide particles in a PDMS matrix. In the presence of an applied magnetic field, the stiffness of the devices' backing layer increases as has been shown previously by others[32,35,36]. The increase in the stiffness of the backing results in increased adhesion because a stiffer backing layer resists peeling. Unlike the magnetic actuated dry adhesives described by Gillies et al.[28], which shows decreased adhesion when the fibres are bent away from the contact surface and is designed for adhering to particles, this work describes adhesion switching due to an increase in the stiffness of the backing layer in the presence of a magnetic field. Our device is designed for potentially adhering to large surface areas as opposed to individual particles. The adhesion provided by our device is dependent on which portion of the normal adhesion test cycle the magnetic field is applied and the direction of the magnetic field, either an increase or decrease in adhesion is observed over the measured normal adhesion force as compared to when no applied magnetic field was present.

5.3. Methods & Materials

5.3.1. Configuration

The magnetically controlled dry adhesive devices used in this study were fabricated from a polymer matrix of PDMS and 20-30 nm Iron Oxide nanoparticles (Fe_3O_4, 3320DX SkySpring Nanomaterials Inc.) herein referred to as Fe-PDMS. The overall structure was composed of a thin layer of mushroom-like dry adhesive fibres fabricated from PDMS. The backing layer, which was constructed of 1.2 mm x 1.2 mm

macro-scale Fe-PDMS posts which were each 1.5 mm tall sandwiched between two thin flat layers of Fe-PDMS. The PDMS micro-structured layer was bonded directly to the Fe-PDMS by a thin layer of Fe-PDMS.

5.3.2. Fabrication

In order to fabricate the magnetically switchable adhesive devices, several fabrication stages were required. First, a mould in which to cast the micro-scale features had to be fabricated in a process that was similar to those reported previously[18,24,39]. The fabrication of the mould used to define the micro-scale feature began with spin-coating a 100mm diameter Poly(methyl methacrylate) (PMMA) wafer with a thin layer of PMGI SF19 resist. After performing a 2 min. soft bake at 100 ^{o}C, a layer of AZ 9260 photoresist was spin-coated over the PMGI layer. The PMMA wafer with the two resist layers was then placed in a thermal chamber and baked for 1 hr. at 80 ^{o}C followed by 90 sec. at 100 ^{o}C. After allowing the wafer to cool, the wafer was soaked in a deionised (DI) water bath for 30 min. After the rehydration step was completed, the photoresist layers were exposed to i-line UV light to transfer the mask pattern to the resist before the resist layers were developed in AZ 400K diluted in a 1:4 ratio by volume with DI water. After achieving the desired undercut, which corresponds to the overhanging mushroom cap of the dry adhesive fibres, a mould with an array of micro-scale holes which define the shape of the mushroom-like dry adhesive fibres was complete.

Once a suitable mould had been fabricated, PDMS (Sylgard 184) was mixed in a 10:1 ratio of prepolymer to curing agent and degassed within a vacuum chamber before being spin coated onto the wafer mould. In the meantime, another mould had been fabricated from PMMA using a laser cutter which cut an array of macro-scale 1.2 mm x 1.2 mm square holes into the 1.5 mm thick PMMA. After bonding the PMMA with the array of macro-scale holes to another flat piece of PMMA, a mould capable of forming 1.2 mm x 1.2 mm by 1.5 mm tall square posts was achieved. After mixing another batch of PDMS, again in a ratio of 10:1 prepolymer to curing agent by weight, 20-30 nm diameter iron oxide particles (Fe_3O_4, 3320DX SkySpring Nanomaterials Inc.) were introduced and thoroughly mixed into the PDMS. The Iron Oxide particles made up 50%

of the total weight of the Fe-PDMS. The choice to fabricate the switchable dry adhesion device using a 50% concentration of Iron Oxide particles was due to two factors: an increased concentration of particles resulted in an increased adhesion switching effect but iron Oxide concentrations greater than 50% were difficult to reliably degas and remove unwanted air pockets during fabrication. After carefully spreading the Fe-PDMS over both the macro-scale featured mould and the cured PDMS on the micro-scale featured mould, the Fe-PDMS was degassed in a vacuum chamber for a period of several hours before finally curing the Fe-PDMS in a thermal chamber at 80 ^{o}C for several hours. After demoulding the cured Fe-PDMS from the macro-scale featured mould, the tips of the 1.2 mm x 1.2 mm posts were bonded to the Fe-PDMS on the unstructured side of the micro-scale featured mould using a small amount of Fe-PDMS. After demoulding from the micro-scale featured mould, the magnetically controlled dry adhesive device was ready for use. A diagram of the completed device is shown in Figure 5-1.

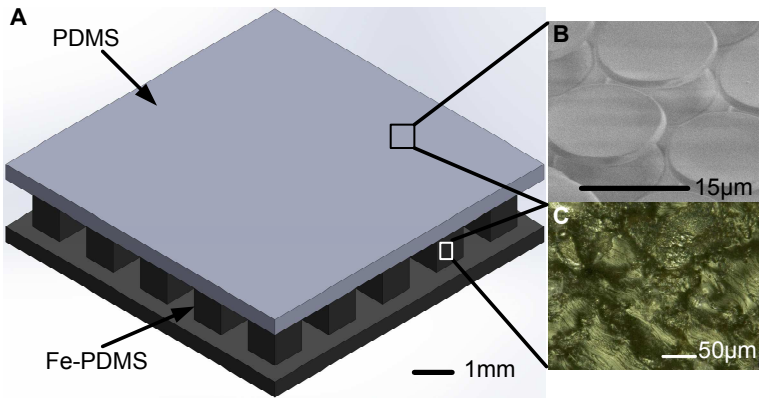

Figure 5-1: A) An illustration of the fabricated device showing the PDMS and Fe-PDMS layers. B) A Scanning Electron Microscope image of the micro-scale features fabricated from PDMS. C) Typical cross-section of the Fe-PDMS layer showing agglomerations of the 20-30 nm Iron Oxide nanoparticles within the PDMS.

5.3.3. Testing

The test setup, as illustrated in Figure 5-2, was composed of the magnetic switchable dry adhesive device placed at the centre of a wire coil. Testing was

performed with either a 6 mm or 12mm diameter spherical glass probe tip mounted to a load cell (Futek, LRF 400) with a Nylon screw that was sufficiently long enough to ensure that any magnetic field applied to the sample did not noticeably affect the load cell reading and any effect of switching the magnetic field on or off on the load cell is below the sensitivity of the load cell. This was confirmed by placing the probe tip at multiple locations both near and away from the surface of the sample under test and switching the magnetic field on and off repeatedly with the magnetic field orientated in both directions. The load cell was mounted on a linear stage (Zaber, T-LS28M-S) which controlled the travelling speed and direction of the probe. The applied magnetic field was produced by a wire coil (APW Company, FC-6489) and was measured using a Hall effect sensor (OHS3150U, OPTEK Technology Inc.).

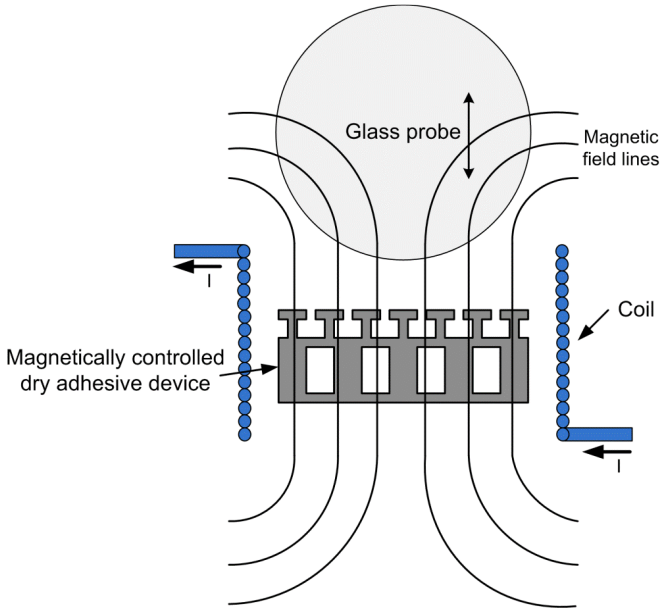

Figure 5-2: A diagram of the test setup. The magnetically controlled dry adhesive device was placed at the centre of a wire coil and normal adhesion force tests were performed without a current applied to the coil and with a current applied to the coil in both directions resulting in two different magnetic field orientations.

5.4. Results and discussion

The overall structure of the device was designed to take advantage of the embedded Iron Oxide particles which, in the presence of a sufficiently strong magnetic

field, caused the overall stiffness of the Fe-PDMS material forming the backing layer to increase, while maintaining the strong adhesive capabilities of PDMS-based dry adhesives. In order to provide a comparison of the adhesion change the magnetic switchable dry adhesive device was capable of providing, a series of tests were performed.

First however, in order to characterise the magnetic field generated by the coil, a Hall Effect sensor (OHS3150U, OPTEK Technology Inc.) was used. The magnetic field profile was measured both from the upper to lower edges of the coil along the central axis of the coil as well as across the diameter of the coil at approximately the midway point between the top and bottom surfaces of the coil. The maximum field strength, as shown in Figure 5-3 was measured to be 0.0126 ± .0009 T at the centre of the coil at a distance of 6.21 ± .01 mm from the upper edge of the coil. As can be seen in Figure 5-3, at the midway point between the upper and lower surfaces of the coil the magnetic field varied across the diameter of the coil from a maximum of 0.0146 ± .0009 T near the edge of the coil to a minimum of 0.0123 ± .0009 T at the centre of the coil. The measurements of the magnetic field strength were performed with the magnetic field in orientation 1 which corresponds to the current moving through the coil in the counter-clockwise direction.

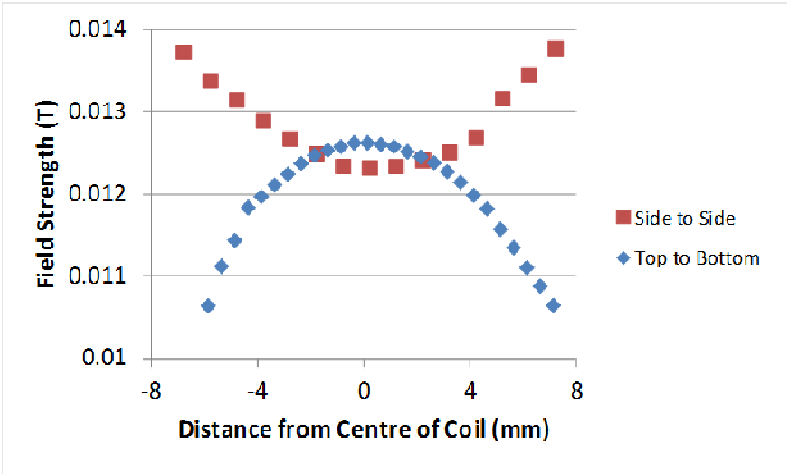

Figure 5-3: The measured change in magnetic field strength from the top surface of the coil to the bottom surface along the central axis of the coil and across the diameter of the coil at the midway point between the upper and lower surfaces of the coil. The measured magnetic field strength was measured to be 0.0133 ± 0.0009 T at the surface of the device during testing.

As described previously, during the fabrication process, Iron oxide particles were mixed into PDMS to form the Fe-PDMS magnetically controlled dry adhesive device. Each Iron Oxide particle acted as a magnetic dipole and, when mixed together and cured in the PDMS, the magnetic dipole of each particle contributed to the net magnetic field of the magnetically controlled dry adhesive device. The net magnetic field of the magnetically controlled dry adhesive device is related to the fabrication process and is due to the mixing process where the particles are oriented in a random fashion and are free to agglomerate before and during curing. As the Fe-PDMS is curing, the particles are free to rotate within the Fe-PDMS and the net effect is that they are able to align themselves with each other and/or with any external magnetic field. The net magnetic field of the magnetically controlled dry adhesive device could be measured using a Hall effect sensor and was determined to be .00023 ± 0.00009 T at the surface of the microscale structures. The South pole of the device was determined to be facing away from the device on the upper surface at an angle, θ, of 38 degrees as shown in Figure 5-4. When the magnetically controlled dry adhesive device was placed in an applied magnetic field, the magnetically controlled dry adhesive device would increase its

stiffness and its height would change as the particles embedded within the PDMS matrix would try and align themselves with the magnetic field as illustrated in Figure 5-4. The dry adhesive fibres on the surface of the magnetically controlled dry adhesive device were 12 µm tall with a 15 µm diameter cap and 1.8 µm thick overhanging cap atop a 12.5 µm diameter post. The centre to centre spacing of the fibres was 20 µm and the adhesive fibres created by the mould are previously shown in Figure 5-1B. The PDMS layer which defined the micro-scale features was 75 µm thick.

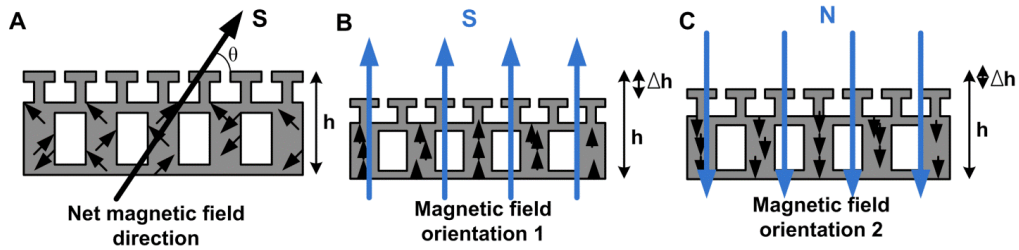

Figure 5-4: A) An illustration of the net magnetic field generated by the iron oxide particles within the Fe-PDMS. Placing the magnetically controlled dry adhesive device in the presence of a sufficiently strong magnetic field in (B) orientation 1 and (C) orientation 2 results in an increase in the stiffness of the Fe-PDMS material.

In order to determine the effective Young's Modulus of the magnetically controlled dry adhesive device, the applied compressive load along with the indentation depth of the spherical indenter were measured. Hertz theory of elastic contact between a spherical indenter and a flat surface, ignoring the effect of the micro-scale features, was used to estimate the effective Young's modulus $E^* = E/(1-\nu^2)$, where $\nu \approx 0.5$ is Poisson's ratio. The Young's modulus of PDMS is approximately 2 MPa. The effective Young's modulus was determined by fitting the experimental data to:

$$F = \frac{4}{3} E^* \sqrt{R d^3} \qquad \text{Equation 5-1}$$

Where F is the applied preload, R is the radius of the indenting sphere and d is the indentation depth[40]. The indentation depth of the glass sphere was directly determined by subtracting the linear stage position when contact with the surface of the device was initiated from the position of the stage at the desired preload depth and was

confirmed to be an accurate determination of the indentation depth of the sphere based on images taken with a digital microscope (Keyence, VHX-2000) fitted with a 100-1000X wide range zoom lens (Keyence, VH-Z100WS).

Figure 5-5A and B show the indentation depth – preload and preload-distance curves respectively for the magnetically controlled dry adhesive device without the magnetic field applied and with the 0.0133 ± 0.0009 T magnetic field applied in both orientation 1 (current flowing counter-clockwise) and in orientation 2 (current flowing clockwise). The sample was loaded at a constant rate of 5μm/s and testing was performed on the same location for each set of tests. Each data point in Figure 5-5 A reflects the average of three separate tests and the error bars indicate the standard deviation. To minimize any residual effect of the presence of the magnetic field on the device on the test results, there was a minimum waiting period of 10 minute between each test and testing was performed in the following order: one test with no applied magnetic field, one test with the magnetic field applied in orientation 1 followed by one test with the magnetic field applied in orientation 2 before performing the second and third set of tests in the same order. After fitting Eq. 1 to the data shown in figures 5, the effective Young's modulus was estimated to be 4.41 ± 0.06 MPa with no magnetic field present and 4.92 ± 0.21 MPa or 4.82 ± 0.16 MPa with the magnetic field present in orientations 1 or 2 respectively. The increase in the effective Young's modulus indicates that the magnetically controlled dry adhesive device becomes stiffer in the presence of an applied magnetic field. Due to the design of the device with a 75μm thick layer of PDMS defining the surface features, the difference in indentation depths under preloading, as seen in Figure 5-5, becomes apparent for preloads greater than ~100mN. Based on the measured magnetic field strength of the coil shown in Figure 5-3, it is unlikely that there is a significant variation in magnetic field strength for the indentation depths at which testing took place. While we were unable to accurately measure the switching speed of the magnetically controlled dry adhesive device, in our experience the effect of switching the magnetic field on or off is immediately noticeable.

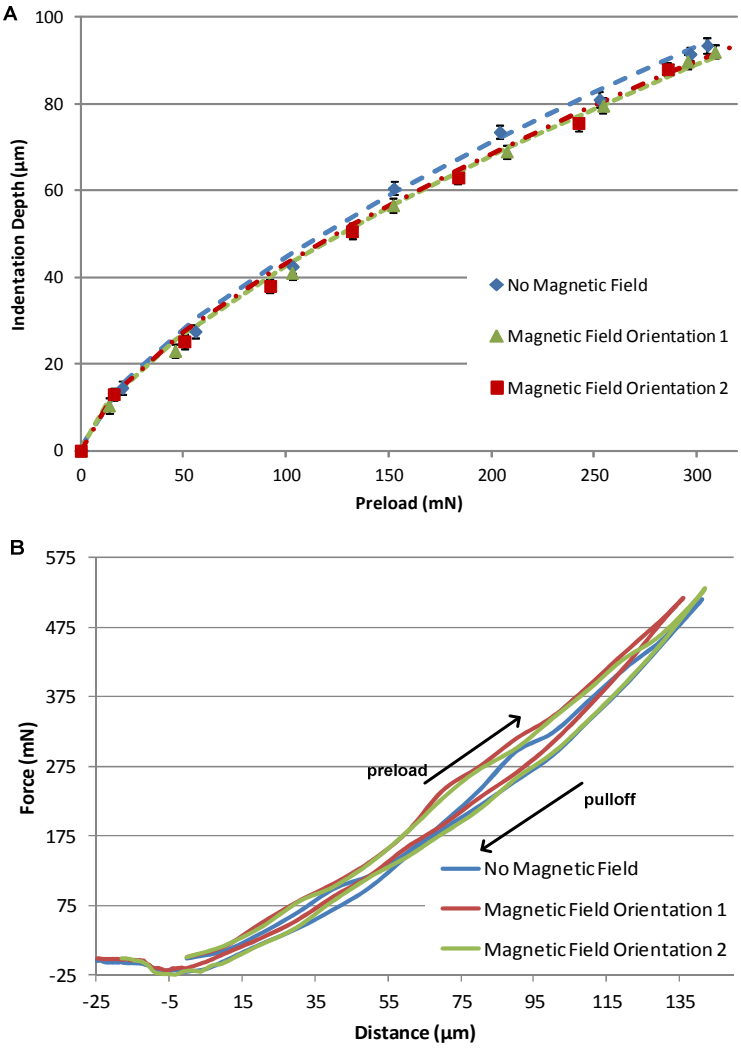

Figure 5-5: A) Preload-Compression curves and B) typical force-distance curves for a 6mm diameter spherical probe indenting the surface of the magnetically controlled adhesive device with no applied magnetic field present and the 0.0133 ± 0.0009 T magnetic field present during preload and pulloff in either orientation 1 or in orientation 2. In A. the dashed lines were fit to the experimental data using Eq. 2 and were used to estimate the Effective Young's modulus. The error bars represent the standard deviation.

In order to compare the effect of the application of a magnetic field on the adhesion provided by the magnetically controlled dry adhesive device, several different series of tests were performed with 20 normal adhesion trials performed for each test.

The average preloading force was the same for all trials and was 311.2 ± 7.4 mN. The preloading force was chosen based on maximizing the magnetic field switching effect of our magnetically controlled dry adhesive device while maximising the adhesion force as tests performed at higher preloads without the magnetic field present did not show a significant increase in adhesion. For each test the preloading force was achieved using a force feedback loop in our custom LabView software which varied the loading rate from 100 µm/s decreasing to as low as 1 µm/s as the measured preload approached the desired preload. Pulloff measurements were all performed with the stage moving at a rate of 200µm/s. Furthermore, the sample was allowed to relax for a minimum of 10 minutes between trials to minimize any residual effects of the presence of the applied magnetic field on the magnetically controlled dry adhesive device and took place over a period of a few days. Multiple sets of trials indicate that the order of testing did not significantly affect the normal adhesion.

For the first set of trials, the normal adhesion pressure was measured using the test setup previously described in Figure 5-2 but without any current flowing through the coil and thus without an applied magnetic field present. The average maximum normal adhesion pressure was measured to be 50.7 ± 2.1 kPa, as shown in Figure 5-6, with an apparent contact area of 2.01 ± .05 mm^2. The apparent contact area of the sphere, A, was calculated based on the measured indentation depth, d, of the glass spherical probe with radius R using:

$$A = 2\pi Rd$$

The second set of tests compared the measured normal adhesion force when the 0.0133 ± 0.0009 T magnetic field was present in either orientation 1 or orientation 2 during the entire normal adhesion test cycle which includes during both preloading and pulloff force measurements. As can be seen in Figure 5-6, under an average applied preloading force of 311.2 ± 7.4 mN the average normal adhesion pressure decreased to 35.2 ± 1.2 kPa with the magnetic field present in orientation 1 and to an average normal adhesion pressure of 40.1 ± 3.4 kPa with the magnetic field applied in orientation 2. The

apparent contact areas were determined by measuring the indentation depth of the spherical probe and found to be 1.86 ± .06 mm^2 and 1.86 ± .05 mm^2 respectively.

The decrease in adhesion observed in the presence of the magnetic field in when it was applied in either direction during both preload and pulloff portions of the adhesion test cycle is due to the increase in stiffness of the magnetically controlled dry adhesive device in the presence of the magnetic field as indicated previously in Figure 5-5. The increased stiffness of the magnetically controlled dry adhesive device results in a smaller contact area for the spherical probe when undergoing the same average 311.2 ± 7.4 mN preload in the presence of the magnetic field as compared to without the applied magnetic field present. The decrease in contact area to achieve the same preload during preloading results in a subsequent decrease in normal adhesion force in the presence of the magnetic field. The difference in adhesion pressure seen between the two magnetic field orientations is likely due to the difference in the stiffness of the device in the presence of the magnetic field in different orientations as the effective Young's modulus is highest when the magnetic field was applied in orientation 1.

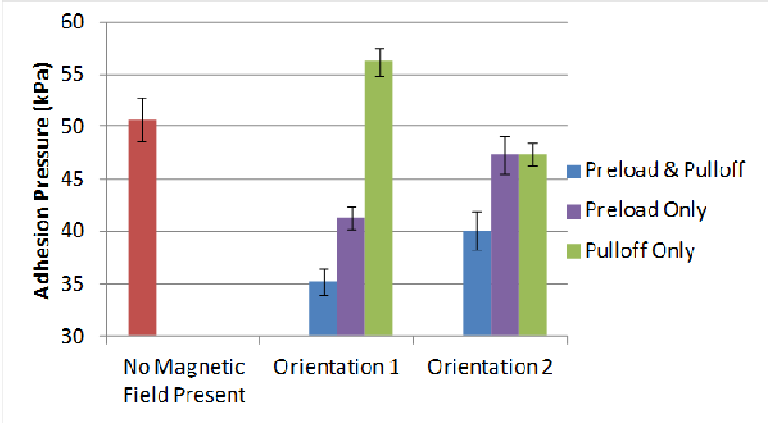

Figure 5-6: A comparison between the normal adhesion force when there was no magnetic field present and when the magnetic field was present in orientation 1 or orientation 2 during both preloading and pulloff, during preload only and during pulloff only. Error bars indicate the standard deviation for each set of measurements.

The third set of normal adhesion tests was performed with the 0.0133 ± 0.0009 T magnetic field present in either orientation 1 or orientation 2 during only the preloading portion of the normal adhesion test cycle. As can be seen in Figure 5-6, a decrease in adhesion was observed with the magnetic field present in either direction. With the 0.0133 ± 0.0009 T magnetic field present in orientation 1 during only the preloading portion of the normal adhesion test cycle, the average normal adhesion pressure was measured to be 41.4 ± 1.3 kPa and, with the magnetic field present in orientation 2 the average normal adhesion pressure was measured to be 47.3 ± 1.9 kPa. The apparent area in contact in each case was determined to be 1.93 ± .05 mm^2 and 1.91 ± .03 mm^2 respectively. As mentioned before, the average preload for all normal adhesion trials was 311.2 ± 7.4 mN. Again, the decrease in normal adhesion force is due to the increased stiffness of the magnetically controlled dry adhesive device in the presence of an applied magnetic field during the preloading portion of the normal adhesion force testing cycle which results in a lower contact area as compared to when no magnetic field was present. A slight increase in normal adhesion force is observed as compared to when the magnetic field is present during both preload and pulloff, which is due to the decrease in the stiffness of the magnetically controlled dry adhesive device during the

pulloff portion of the normal adhesion test cycle. After the desired preload is achieved, the applied magnetic field is switched off and the magnetically controlled dry adhesive device relaxes into its softer phase resulting in a slight increase in contact area which results in an increased adhesion force and adhesion pressure.

The final set of normal adhesion tests involved performing normal adhesion pressure measurements with the applied 0.0133 ± 0.0009 T magnetic field present during only the pulloff portion of the normal adhesion test cycle. As shown in Figure 5-6, over a period of 20 trials for each test, the average normal adhesion pressure was measured to be 56.2 ± 1.3 kPa with the magnetic field present in orientation 1. With the 0.0133 ± 0.0009 T magnetic field present in orientation 2 however, a decrease in the average normal adhesion pressure was observed as compared to when no applied magnetic field was present. The average measured normal adhesion pressure with the magnetic field present in orientation 2 was 47.4 ± 1.1 kPa. The average apparent area in contact was 2.01 ± 0.5 mm^2 with no applied magnetic field present, 1.97 ± 0.3 mm^2 with the magnetic field applied in orientation 1 and 2.04 ± 0.4 mm^2 when applied in orientation 2. An anova analysis was performed to determine if the adhesion results when there was no magnetic field were statistically significant from when the magnetic field was applied in either orientation 1 or 2 during pulloff. The F-value was 12.336 while the $F_{critical}$-value 3.179 indicating that the results were in fact statistically significantly.

In order to ensure that the changes in adhesion observed when the magnetic field was applied during pulloff were not due to the measured contact area being roughly the same size as the macro scale posts forming the backing layer, testing was also performed with a 12.93 mm diameter glass spherical tip. Figure 5-7 compares the adhesion pressure between when there was no applied magnetic field present and when the magnetic field was applied in orientations 1 and 2 during pulloff only. The average preloading force for all three sets of tests was 1.013 ± 0.005N and the average contact area for all tests was 9.66 ± 0.05 mm^2. Each data point shows the average adhesion pressure for 10 tests and the error bars represent the standard deviation.

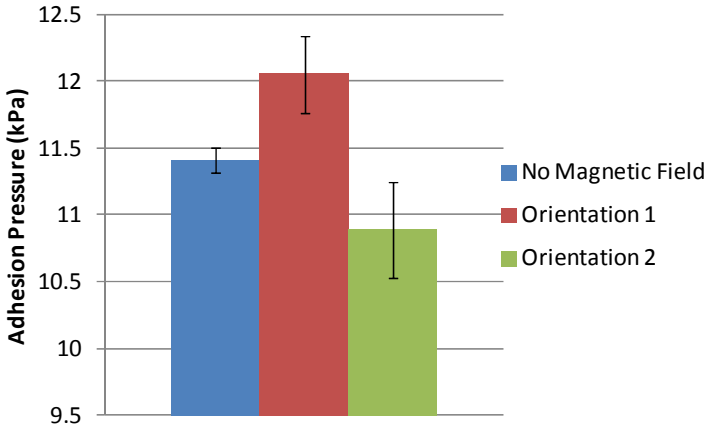

Figure 5-7: A comparison of the average measured adhesion pressure using a 12.93mm diameter spherical glass probe when there was no applied magnetic field present and when the magnetic field was applied during pulloff in both orientations 1 and 2. Errors bars represent the standard deviation.

In order to determine if the increase in adhesion was caused by the change in stiffness of the magnetically controlled dry adhesive device or another process such as an increase or decrease in contact area, normal adhesion testing was performed with a flat PMMA probe. In order to ensure alignment of the flat probe to the magnetically controlled dry adhesive device the flat PMMA with a surface area of 35.08 ± 0.01 mm^2 was gently placed on the surface of the device and then, using the linear stage, was bonded to a nylon screw attached directly to the load cell. After curing, normal adhesion tests were performed as described previously with no applied magnetic field and with the 0.0133 ± 0.0009 T magnetic field applied in either orientation 1 or orientation 2 during preloading. After applying an average preloading force of 1.510 ± .003 N the normal adhesion pressure was measured to be 52.9 ± 0.5 kPa with no applied magnetic field present, 52.3 ± 0.7 kPa with the magnetic field applied in orientation 1 and 52.4 ± 0.4 kPa with the magnetic field applied in orientation 2. In other words, there was no

significant difference in adhesion when the contact area remained constant regardless of the orientation of the magnetic field.

Interestingly, during the adhesion testing with the flat probe it was found that the height of the magnetically controlled dry adhesive device changed depending on if the magnetic field was applied and the direction in which it was applied. The change in the height of the magnetically controlled dry adhesive device was determined by subtracting the linear stage position when the surface of the magnetically controlled dry adhesive device was first contacted from the linear stage position when the desired preload was achieved. With the magnetic field applied in orientation 1 the thickness of the magnetically controlled dry adhesive device increased by an average of 22.7 ± 0.9 µm but decreased by an average of 3.5 ± 1.0 µm with the magnetic field applied in orientation 2 based on 5 tests each.

The increase or decrease in the overall thickness of the magnetically controlled dry adhesive device in the presence of a magnetic field is responsible for an increase or decrease in the contact area of the spherical probe. The increase or decrease in the contact area of the glass probe when the magnetic field is switched on is due to the linear stage (and thus the glass probe) being held stationary and the height of the magnetically controlled dry adhesive device increasing or decreasing. The increased thickness of the magnetically controlled dry adhesive when the magnetic field is in orientation 1 and the glass probe is stationary potentially increases the contact radius from 786.8 µm to 865 µm. Similarly, with the magnetic field applied in orientation 2 when the glass probe is stationary the overall height of the magnetically controlled dry adhesive device decreases and consequently the contact radius is potentially reduced from 799 µm to 786 µm. A diagram outlining the change in contact area is shown in Figure 5-8.

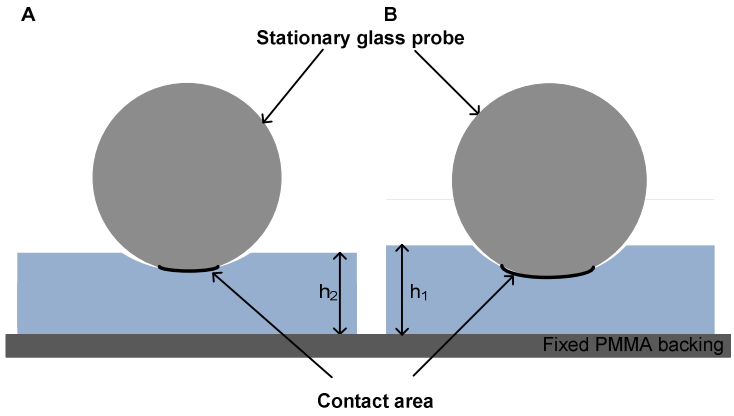

Figure 5-8: A diagram showing the increase in contact area due to the change in height of the device when the magnetic field is applied in orientation 1. A) The sample is preloaded without the applied magnetic field present. B) The magnetic field is switched on in orientation 1 and the height of the device increases resulting in increased contact area because the base of the device is fixed in place and the glass probe remains stationary.

Figure 5-9 compares three typical force vs time curves which show the entire preload-pulloff normal adhesion test cycle when there is no applied magnetic field and when the magnetic field is applied during the pulloff portion of the normal adhesion test cycle in both orientation 1 and orientation 2. Figure 5-9 breaks down the normal adhesion test cycle into three distinct regions: A) the preload is being applied at a constant rate of 50 µm/s, B) The linear stage and glass probe are held stationary and the magnetic field is switched on and C. The linear stage is moving in the reverse direction at a constant rate of 50 µm/s and the pulloff force is being measured. The circled region in the inset of Figure 5-9 shows that there is a small increasing spike in the measured preloading force when the magnetic field is switched on in orientation 1 and a small decreasing spike in the preloading force when the magnetic field is switched on in orientation 2 while the glass probe remains stationary. There is no sharp increase or decrease in the preloading force when there is no applied magnetic field. Note that while the glass probe is stationary the preloading force decreases as the material of the magnetically controlled dry adhesive device relaxes under the applied preload and the rate of decrease of the measured preloading force, except for the increases or decreases in preload due to switching on the magnetic field, is at the same rate for all three cases.

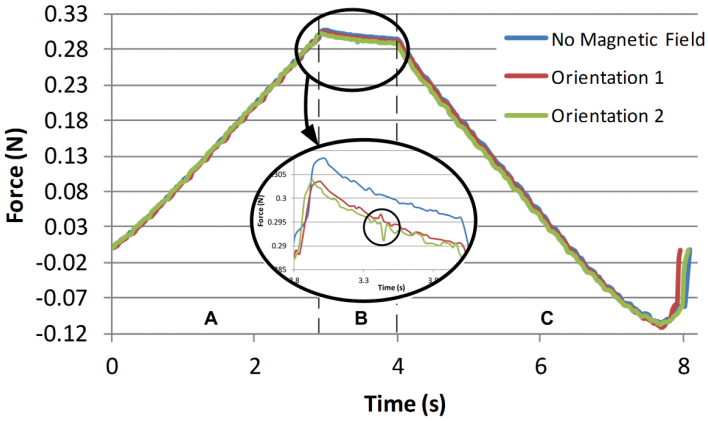

Figure 5-9: Typical force vs. time curves during the entire preload-pulloff normal adhesion test cycle for when there was no applied magnetic field and when the magnetic field was applied in either orientation 1 or orientation 2 during the pulloff portion of the test. Region A shows the increase in force as the magnetically controlled dry adhesive device is being preloaded. Region B shows a slight decrease in force as the sample relaxes while the glass probe is stationary while region C shows the decrease in force during the pulloff portion of the test. Negative forces indicate the device is under tension. The inset shows a close-up view of the change in force with respect to time in region B and the circled region within the inset shows the increase or decrease in force when the magnetic field is switched on resulting in increased or decreased contact area.

In order to compare the effect of the magnetic field at varying strengths in both orientations 1 and 2, a series of tests were performed with a minimum of four trials per test. During each set of trials, normal adhesion force measurements were performed with the magnetic field applied in either orientation 1 or orientation 2 during the pulloff force measurements. The strength of the magnetic field was varied by decreasing the current through the coil and normal adhesion force measurements were performed with magnetic field strengths of 0 T, 0.0031 T, 0.0064 T, 0.0097 T, 0.0115 T and 0.0133 T. As can be seen below in Figure 5-10 A and as summarized in table 1, increasing the magnetic field strength with the magnetic field applied in orientation 1 during pulloff force measurements results in an increase in the normal adhesion force as compared to when

no applied magnetic field was present. In Figure 5-10 B, a decrease in normal adhesion strength is seen as the magnetic field strength is increased and the magnetic field is applied during pulloff force measurements in orientation 2. In both cases, an applied magnetic field strength of 0.0031 T or less appears to have a minimal effect on the measured normal adhesion force.

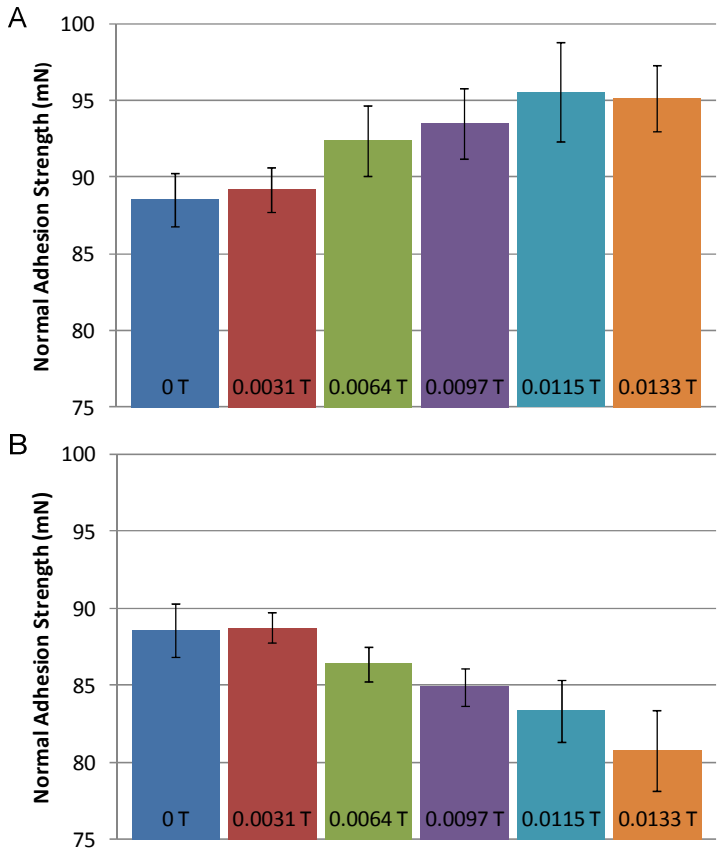

Figure 5-10 A comparison of the change in adhesion strength due to the presence of a magnetic field in (A) orientation 1 and (B) orientation 2. The magnetic field strength for each adhesion measurement is shown at the base of each column.

Table 5-1: Summary of the normal adhesion test results shown in Figure 5-9A and B.

Magnetic Field Strength (T)	Magnetic Field Orientation 1		Magnetic Field Orientation 2	
	Preload Force (mN)	Pulloff Force (mN)	Preload Force (mN)	Pulloff Force (mN)
0	299.6 ± 0.3	88.6 ± 1.8	299.6 ± 0.3	88.6 ± 1.8
0.0031	305.0 ± 1.3	89.2 ± 1.5	301.8 ± 0.5	88.8 ± 1.1
0.0064	307.6 ± 3.8	92.4 ± 4.4	301.9 ± 0.4	86.4 ± 1.2
0.0097	309.8 ± 5.7	93.6 ± 2.3	301.6 ± 0.6	84.9 ± 1.2
0.0115	313.4 ± 7.4	95.6 ± 3.2	302.6 ± 1.0	83.4 ± 2.0
.0133	314.7 ± 6.6	95.1 ± 2.2	304.4 ± 2.0	80.8 ± 2.7

Finally, in order to determine if the adhesion test results previously shown for the protoype magnetically controlled dry adhesive device were repeatable with another device, a second magnetically controlled dry adhesive device was fabricated and normal adhesion tests were performed with the 0.0133 ± 0.0009 T magnetic field present during only the pulloff portion of the adhesion test cycle. Figure 11 compares the % change in adhesion for the first sample (sample 1) and the second sample (sample 2) with the magnetic field applied in either orientation 1 or 2 over a series of 5 trials for each test. The % change in adhesion is compared to the normal adhesion force measurements performed without the applied magnetic present. Note that the overall behaviour of the two samples was similar even though the orientation of the magnetic field that resulted in the greatest % increase in adhesion force was different for each sample. The change in adhesion when in the presence of an applied magnetic field appears to be a function of the net magnetic field of the magnetically controlled dry adhesive device which is a function of the fabrication process. The direction of the net magnetic field of the magnetically controlled dry adhesive device is due to the fabrication process where mixing Iron Oxide particles into PDMS results in randomly aligned Iron Oxide particles within the uncured Fe-PDMS. Prior to curing, the particles are free to rotate within the uncured PDMS and can align themselves with each other or with an external magnetic

field. In the future, a method of fabricating magnetically controlled adhesive devices which optimally improves overall adhesion should be developed and will likely involve curing the Fe-PDMS in the presence of a controlled magnetic field which could result in a stronger net magnetic field over that which is presently observed along a greater change in adhesion in the presence of an applied magnetic field.

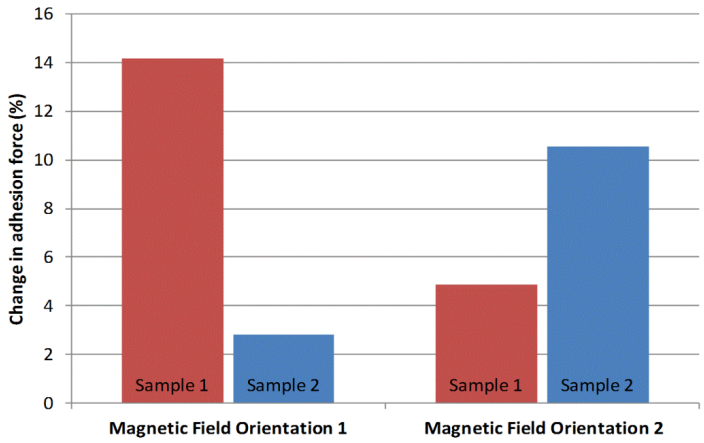

Figure 5-11: A comparison of the % change in adhesion between two magnetically controlled dry adhesive device samples when the samples were in the presence of a magnetic field and when no magnetic field was present. The adhesion data shown previously corresponds to sample 1.

5.5. Conclusion

A method of fabricating magnetically controlled dry adhesive devices was developed. Using a coil, a magnetic field of up to 0.0133 ± 0.0009 T was generated and, when normal adhesion pressure measurements were performed, decreased normal adhesion pressures were measured when the applied magnetic field was present during the entire normal dry adhesive test cycle as compared to when there was no applied magnetic field present. Similarly, a decrease in adhesion was measured when the magnetic field was present during only the preload portion of the normal adhesion test

cycle. In both cases, the decrease in adhesion pressure was due to an increase in the overall stiffness of the magnetically controlled dry adhesive device resulting in a smaller contact area with the spherical glass probe under the same preloading force. When the magnetic field was present during only the pulloff portion of the dry adhesion test cycle, an increase in measured pulloff pressure was observed when the applied magnetic field was in orientation 1 and decreased when the applied magnetic field was in orientation 2. With the magnetic field applied in orientation 1 when the device was preloaded, a spike in preloading force, due to the height of the device changing, is seen as is responsible for increasing the contact area which results in increased adhesion. When the magnetic field in orientation 2 is switched with the device preloaded, a decreasing spike in preload force is observed due to the thickness of the device decreasing and a slight decrease in adhesion pressure is measured as compared to when no applied magnetic field was present. Multiple devices showed similar adhesion characteristics.

5.6. Acknowledgement

This work was financially supported by The Natural Sciences and Engineering Research Council of Canada (NSERC)

5.7. References

(1) Autumn, K.; Sitti, M.; Liang, Y. A.; Peattie, A. M.; Hansen, W. R.; Sponberg, S.; Kenny, T. W.; Fearing, R.; Israelachvili, J. N.; Full, R. J. Evidence for van Der Waals Adhesion in Gecko Setae. Proc. Natl. Acad. Sci. U. S. A. 2002, 99, 12252–12256.

(2) Autumn, K.; Liang, Y. a; Hsieh, S. T.; Zesch, W.; Chan, W. P.; Kenny, T. W.; Fearing, R.; Full, R. J. Adhesive Force of a Single Gecko Foot-Hair. Nature 2000, 405, 681–685.

(3) Sitti, M. High Aspect Ratio Polymer Micro/nano-Structure Manufacturing Using Nanoembossing, Nanomolding and Directed Self-Assembly. In ASME 2003 International Mechanical Engineering Congress and Exposition: Design Engineering, Volumes 1 and 2; Washington, DC, USA, 2003; pp. 293–297.

(4) Geim, A. K.; Dubonos, S. V; Grigorieva, I. V; Novoselov, K. S.; Zhukov, A. A.; Shapoval, S. Y. Microfabricated Adhesive Mimicking Gecko Foot-Hair. Nat. Mater. 2003, 2, 461–463.

(5) Davies, J.; Haq, S.; Hawke, T.; Sargent, J. A Practical Approach to the Development of a Synthetic Gecko Tape. Int. J. Adhes. Adhes. 2009, 29, 380–390.

(6) Sameoto, D.; Menon, C. Direct Molding of Dry Adhesives with Anisotropic Peel Strength Using an Offset Lift-off Photoresist Mold. J. Micromechanics Microengineering 2009, 19, 115026.

(7) Krahn, J.; Liu, Y.; Sadeghi, A.; Menon, C. A Tailless Timing Belt Platform (TBCP-II) Utilizing Dry Adhesives with Mushroom Caps. Smart Mater. Struct. 2011, 20, 115021 (11pp).

(8) Krahn, J.; Menon, C. Characterization of Dry Adhesives Fabricated Using a Novel Mass Production Manufacturing Technique. Macromol. React. Eng. 2013, 7, 632–637.

(9) Greiner, C.; Campo, A. Del; Arzt, E. Adhesion of Bioinspired Micropatterned Surfaces: Effects of Pillar Radius, Aspect Ratio, and Preload. Langmuir 2007, 23, 3495–3502.

(10) Jeong, H. E.; Lee, J.-K.; Kwak, H. N.; Moon, S. H.; Suh, K. Y. Effect of Leaning Angle of Gecko-Inspired Slanted Polymer Nanohairs on Dry Adhesion. Appl. Phys. Lett. 2010, 90.

(11) Spolenak, R.; Gorb, S.; Gao, H.; Arzt, E. Effects of Contact Shape on the Scaling of Biological Attachments. Proc. R. Soc. A 2005, 461, 305–319.

(12) Varenberg, M.; Gorb, S. Close-up of Mushroom-Shaped Fibrillar Adhesive Microstructure: Contact Element Behaviour. J. R. Soc. Interface 2008, 5, 785–789.

(13) Del Campo, A.; Greiner, C.; Arzt, E. Contact Shape Controls Adhesion of Bioinspired Fibrillar Surfaces. Langmuir 2007, 23, 10235–10243.

(14) Parsaiyan, H.; Barazandeh, F.; Mehdirezaei, S.; Parsaiyan, M.; Safdari, M. Wide-End Fibers and Their Adhesion Performance in Biological Attachment Systems. Int. J. Adhes. Adhes. 2009, 29, 444–450.

(15) Jeong, H. E.; Suh, K. Y. Nanohairs and Nanotubes: Efficient Structural Elements for Gecko-Inspired Artificial Dry Adhesives. Nano Today 2009, 4, 335–346.

(16) Kwak, M. K.; Pang, C.; Jeong, H.-E.; Kim, H.-N.; Yoon, H.; Jung, H.-S.; Suh, K.-Y. Towards the Next Level of Bioinspired Dry Adhesives: New Designs and Applications. Adv. Funct. Mater. 2011, 21, 3606–3616.

(17) Sameoto, D.; Menon, C. Recent Advances in the Fabrication and Adhesion Testing of Biomimetic Dry Adhesives. Smart Mater. Struct. 2010, 19, 103001.

(18) Krahn, J.; Sameoto, D.; Menon, C. Controllable Biomimetic Adhesion Using Embedded Phase Change Material. Smart Mater. Struct. 2011, 20, 015014.

(19) Kim, S.; Sitti, M.; Xie, T.; Xiao, X. Reversible Dry Micro-Fibrillar Adhesives with Thermally Controllable Adhesion. Soft Matter 2009, 5, 3689.

(20) Reddy, S.; Arzt, E.; del Campo, a. Bioinspired Surfaces with Switchable Adhesion. Adv. Mater. 2007, 19, 3833–3837.

(21) Arul, E. P.; Ghatak, A. Control of Adhesion via Internally Pressurized Subsurface Microchannels. Langmuir 2012, 28, 4339–4345.

(22) Nadermann, N.; Ning, J.; Jagota, A.; Hui, C.-Y. Active Switching of Adhesion in a Film-Terminated Fibrillar Structure. Langmuir 2010, 26, 15464–15471.

(23) Jeong, H. E.; Kwak, M. K.; Suh, K. Y. Stretchable, Adhesion-Tunable Dry Adhesive by Surface Wrinkling. Langmuir 2010, 26, 2223–2226.

(24) Krahn, J.; Menon, C. Electro-Dry-Adhesion. Langmuir 2012, 28, 5438–5443.

(25) Krahn, J. M.; Pattantyus-Abraham, A. G.; Menon, C. Polymeric Electro-Dry-Adhesives for Use on Conducting Surfaces. Proc. Inst. Mech. Eng., Part L 2013, 228, 109–114.

(26) Ruffatto III, D.; Parness, A.; Spenko, M. Improving Controllable Adhesion on Both Rough and Smooth Surfaces with a Hybrib Electrostatic/gecko-like Adhesive. J. R. Soc. Interface 2014, 11, 20131089.

(27) Berengueres, J.; Takahashi, K. Magnetic Hair for Wall Mobility. In Proceedings of the 2006 IEEE/RSJ International Conference on Inteligent Robots and Systems; Beijing, 2006.

(28) Gillies, Andrew, G.; Kwak, J.; Fearing, R. S. Controllable Particle Adhesion with a Magnetically Actuated Synthetic Gecko Adhesive. Adv. Funct. Mater. 2013, 23, 3256–3261.

(29) Northern, M. T.; Greiner, C.; Arzt, E.; Turner, K. L. A Gecko-Inspired Reversible Adhesive. Adv. Mater. 2008, 20, 3905–3909.

(30) Tian, T. F.; Zhang, X.; Li, W.; Alici, G.; Ding, J. Study of PDMS Based Magnetorheological Elastomers. J. Phys. 2013, 412, 1–8.

(31) Li, W.; Nakano, M. Fabrication and Characterization of PDMS Based Magnetorheological Elastomers. Smart Mater. Struct. 2013, 22, 055035–1–055035–055037.

(32) Varga, Z.; Filipcsei, G.; Zrínyi, M. Magnetic Field Sensitive Functional Elastomers with Tuneable Elastic Modulus. Polymer (Guildf). 2006, 47, 227–233.

(33) Filipcsei, G.; Csetneki, I.; Szilágyi, A.; Zrínyi, M. Magnetic Field-Responsive Smart Polymer Composites. Adv. Polym. Sci. Polym. Sci. 2007, 206, 137–189.

(34) Li, J.; Zhang, M.; Wang, L.; Li, W.; Sheng, P.; Wen, W. Design and Fanbrication of a Microfluidic Mixer from Carbonyl Iron-PDMS Composite Membrane. Microfluid. Nanofluid 2011, 10, 919–925.

(35) Varga, Z.; Filipcsei, G.; Szilágyi, A.; Zrínyi, M. Electric and Magnetic Field-Structured Smart Composites. Macromol. Symp. 2005, 227, 123–134.

(36) Varga, Z.; Filipcsei, G.; Zrínyi, M. Smart Composites with Controlled Anisotropy. Polymer (Guildf). 2005, 46, 7779–7787.

(37) Long, R.; Hui, C.-Y.; Kim, S.; Sitti, M. Modeling the Soft Backing Layer Thickness Effect on Adhesion of Elastic Microfiber Arrays. J. Appl. Phys. 2008, 104, 044301.

(38) Kim, S.; Sitti, M.; Hui, C.-Y.; Long, R.; Jagota, A. Effect of Backing Layer Thickness on Adhesion of Single-Level Elastomer Fiber Arrays. Appl. Phys. Lett. 2007, 91, 161905.

(39) Krahn, J.; Menon, C. Dry Adhesives with Sensing Features. Smart Mater. Struct. 2013, 22, 085010.

(40) Del Campo, A.; Greiner, C.; Arzt, E. Contact Shape Controls Adhesion of Bioinspired Fibrillar Surfaces. Langmuir 2007, 23, 10235–10243.

Chapter 6. Dry adhesives with sensing features

The content of this chapter has been slightly modified from what first appeared in print in:

> Krahn, J and Menon, C. Dry adhesives with sensing features. *Smart Materials and Structures* 2013, 22, 085010 (9pp)

6.1. Abstract

Geckos are capable of detecting detachment of their feet. Inspired by this basic observation, a novel functional dry adhesive is proposed, which can be used to measure the instantaneous forces and torques acting on the adhesive pad. Such a novel sensing dry adhesive could potentially be used by climbing robots to quickly realize and respond appropriately to catastrophic detachment conditions. The proposed torque and force sensing dry adhesive was fabricated by mixing Carbon Black (CB) and Polydimethylsiloxane (PDMS) to form a functionalized adhesive with mushroom caps. The addition of CB to PDMS resulted in conductive PDMS which, when under compression, tension or torque, resulted in a change in the resistance across the adhesive patch terminals. The proposed design of the functionalized dry adhesive enables distinguishing an applied torque from a compressive force in a single adhesive pad. A model based on beam theory was used to predict the change in resistance across the terminals as either a torque or compressive force was applied to the adhesive patch. Under a compressive force, the sensing dry adhesive was capable of measuring compression stresses from 0.11 Pa to 20.9 kPa. The torque measured by the adhesive patch ranged from 2.6 mN-m to 10 mN-m at which point the dry adhesives became detached. The adhesive strength was 1.75 kPa under an applied preload of 1.65 kPa for an adhesive patch with an adhesive contact area of 7.07 cm^2.

6.2. Introduction

Ever since the discovery that the ability of geckos to adhere to a wide range of surfaces was largely due to Van der Waals forces[1], there have been a wide range of advances in the development of synthetic gecko-adhesives which have come to be known as biomimetic dry adhesives. Over the last decade, there have been several different approaches to manufacturing biomimetic dry adhesives which include moulding polydimethylsiloxane (PDMS)[2–4], plasma etching[5] and nano-imprinting[6] among others. When relying on Van der Waals forces, increased adhesion is a direct result of several factors including material type and area in contact. One method to increase adhesion is to use a hierarchical approach which enables better conformation and attachment to surfaces[7,8] while other approaches are to vary the stiffness of the backing layer[4], increase fibre density while reducing the diameter of individual fibres[9], varying the aspect ratio and the addition of a overhanging mushroom cap[10–13].

Meanwhile, other research groups have been concentrating their efforts on the manufacture and development of conductive polymers. Typically, polymeric materials such as polypropylene or polyurethanes[14], PDMS[15–18] or UV-curable monomers[17] have been made conductive by mixing nano- or micro-sized particles into the uncured polymer. While many possibilities exist, the particles commonly added to make polymers conductive are either silver[16,17], carbon black (CB)[14,16–18] or carbon nanotubes[15,19,20] or some combination of these where the overall conductivity of the particle-polymer composite is a direct result of the conductivity of the particles and the percentage by weight of the particles added to the polymer.

Conductive polymers, such as PDMS with embedded carbon black particles (CB-PDMS), have been used in the fabrication of many different devices ranging from flexible circuits[21,22], strain gauges/sensors[23,24], pressure sensors[25] and artificial hair sensors[26]. Most sensing devices made from conductive polymers rely on a relatively low concentration of conductive particles which, when the devices are compressed or flexed, result in a relative change in the conductivity across the device as the particles move either closer or further apart within the polymer matrix.

While there has been significant research into developing force sensing resistors, to the best of our knowledge this is the first time that biomimetic dry adhesives and force sensing resistors have been fabricated as a single integrated adhesive patch. Designed for use by climbing robots or for being embedded in gloves for climbing vertical surfaces, a torque and force sensor which integrates both an attachment method such as gecko-like dry adhesives with the ability to monitor forces and torques applied to the adhesives could allow promptly detecting and responding to detachment and preload conditions.

6.3. Methods and materials

6.3.1. Configuration

The devices used in this study were fabricated from a mix of PDMS and carbon black particles with two dry adhesive layers bridged by three groups of macro-scale posts. Four macro-scale 1 mm x 1 mm square posts which were approximately 1 mm tall were arranged around the centre of the adhesive patch at a distance of 2 mm from the centre. These four posts form the central region of the Torque and Force Sensing (TFS) adhesive patch. The two outer regions were symmetrically opposite across the centre of the adhesive patch and are each formed from two rows of 12 square posts which were also 1 mm x 1 mm and 1 mm tall. The posts were arranged at the outer edge of the adhesive patch and at a distance of 13 mm from the centre of the adhesive patch. The base layer of CB-PDMS dry adhesive forms the grounding layer during testing while three separate strips of CB-PDMS were attached to the top of the posts and form the other three contact points for the adhesive patch. As the adhesive patch undergoes a torsion or compression the bending and compression of the posts result in a change in the resistance measured across each set of posts. The central set of posts is equivalent to 4 resistors in parallel and the outer sections of posts are each equivalent to 23 resistors connected in parallel by the contact points. The arrangement of the resistance varying posts ensures the measured resistance across individual posts under compression for all three sections to be similar. Under torsion however, the tips of the four central posts undergo a much lower deflection than the forty-six posts arranged around the perimeter. This results in the resistance change across the outer posts being larger than that across the inner posts and results in a method of measuring both the

applied torsion and compression. The differences in the resistance changes across the central and outer sections provide a method of determining if the variation in resistance is caused by a torsion or compression. Figure 6-1A shows a scanning electron microscope image (SEM) of the micro-scale biomimatic dry adhesive fibres while Figure 6-1B shows a three dimensional diagram of the conductive regions of the TFS. Note that the overall diameter of the TFS is 3 cm. Figure 6-1C shows the TFS adhesive patch being used by a spider-like robot.

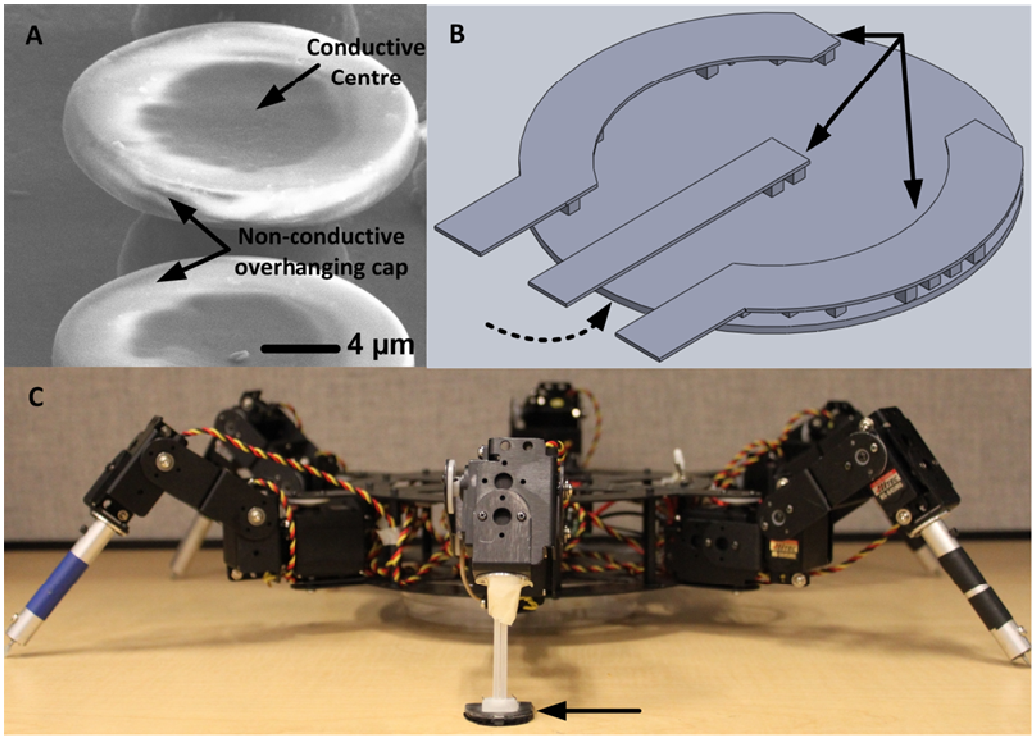

Figure 6-1: ***A.*** **Scanning electron microscope image of the biomimetic dry adhesive fibres with overhanging mushroom cap used as the adhesive layer in the Torque and Force Sensing (TFS) dry adhesive patch. B. TFS dry adhesive patch with a 3cm diameter. For clarity, only the CB-PDMS regions are shown. The solid arrows indicate the 3 sections of macro-scale posts and electrical contacts while the dashed arrow indicates the location of the micro-scale posts with mushroom caps on the underside. A second non-conducting PDMS dry adhesive layer (not shown) would normally form the top layer of the adhesive patch. C. Potential use for the TFS dry adhesive as an attachment device for a climbing robot as indicated by the arrow.**

6.3.2. Fabrication

Force sensing biomimetic dry adhesive resistors were manufactured in several steps based on the processes designed for the fabrication of two-layer dry adhesives[27]. Firstly, PDMS (Sylgard 184) was thoroughly mixed in a 10:1 ratio of prepolymer to curing agent. The desired amount of Carbon Black (Vulcan XC-72R), determined by the desired material conductivity as characterised in our previous work[18], was then thoroughly mixed into the previously prepared and uncured PDMS resulting in a composite of CB and PDMS (CB-PDMS). The diameter of the CB particles was 20-50 nm[28]. The thoroughly mixed CB-PDMS was then evenly spread over a mould created

from poly(methyl methacrylate) (PMMA) by a laser cutter which forms an array of macro-scale 1 mm x1 mm square posts which are 1 mm tall. After the CB-PDMS was spread over the array of macro-scale posts and had been degassed to remove any trapped air from within the CB-PDMS mixture, the CB-PDMS was baked at 80 ^{o}C for a minimum of 1 hour to allow the CB-PDMS to cure. Once the array of macro-scale posts had been cured, it was carefully removed from the mould and cut into the desired shape. The manufacturing steps for the central layer of the TFS may be seen in Figure 6-2.

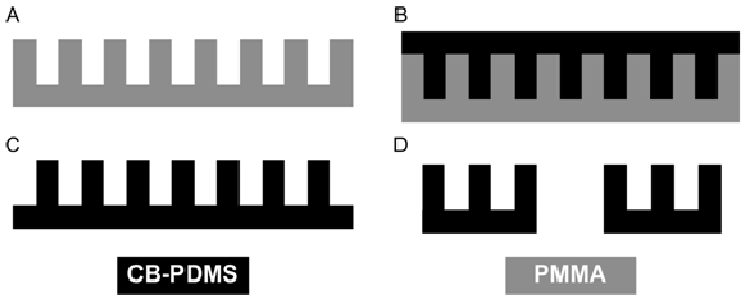

Figure 6-2: A. PMMA mould manufactured using a laser cutter to form an array of 1 mm x1 mm by 2 mm tall macro-scale posts. B. CB-PDMS mixed, spread over the mould and degassed in a vacuum chamber. C. Cured array of macro-scale posts. D. Strips of macro-scale posts manufactured from CB-PDMS.

Meanwhile, a second batch of CB-PDMS is mixed which may have a different ratio of CB to PDMS than the first depending on the desired resistivity of the grounding layer. The micro-scale mushroom-like features which form the dry adhesive structures were formed by spreading the CB-PDMS composite over the surface of a mould capable of reliably reproducing mushroom-like features followed by degassing in a vacuum chamber. Based on the work previously presented[3,4], the manufacturing process began by spin-coating a100 mm diameter PMMA wafer with a layer of PMGI SF19 resist. After baking for 2min. at 100 ^{o}C, a layer of AZ 9260 photoresist was spin-coated on top of the PMGI followed by baking for 1hr. at 80 ^{o}C and 90sec. at 100 ^{o}C. After cooling, the PMMA wafer was allowed to soak for 30min. in deionised (DI) water. After re-hydrating, the photoresist layers were exposed to i-line UV light before the resist was developed in AZ 400K developer diluted 1:4 with DI water by volume. After developing the resist to achieve the desired undercut, the 100 mm diameter mould was composed of arrays of micro-scale mushroom-like features which were 10.5μm tall with a 9.3μm diameter post.

Atop the post sits the 1.8μm thick 17.8μm diameter overhanging mushroom-like cap. The centre to centre spacing of these structures within the array is 20μm. A Scanning Electron Microscope (SEM) image of these structures was previously shown in Figure 6-1A. As indicated in Figure 6-1A, the post and backing layer are filled with the CB-PDMS composite forming the conductive centre. The rim of the overhanging mushroom cap however is composed of only PDMS and is non-conducting. The overhanging cap forms after the CB-PDMS has been spread over the surface of the mould and, during the degassing period, some of the PDMS from within the CB-PDMS seeps into the region of the mould forming the mushroom cap. Our previous work indicates that there is no discernible suction effect caused by the inset central region[18].

After degassing the CB-PDMS on the dry adhesive mould, the strips of previously prepared large scale posts are placed atop the uncured CB-PDMS already spread over the dry adhesive mould with only the tips of the large scale posts in contact with the backing layer of the dry adhesive sheet. Both the moulded, but uncured, CB-PDMS dry adhesive sheet and the strips of large-scale posts are then placed within an 80 ^{o}C thermal chamber for 3hrs to allow the CB-PDMS composite structure to fully cure. Upon curing, the CB-PDMS force sensing dry adhesives are fully formed and easily peel from the dry adhesive mould. Figure 6-3 outlines the step by step manufacturing process for the force sensing dry adhesive patches. Creating a TFS with adhesives on both sides can be done by simply mixing PDMS in a 10:1 ratio of prepolymer to curing agent and applying a thin layer of the uncured PDMS to the back side of a previously moulded adhesive sheet trimmed to the desired size and shape. It is important that the second layer be non-conducting in order to ensure that the electrical contacts remain separated. Carefully seating the contact layer of the TFS into the uncured PDMS layer and allowing the layers to cure together forms a single adhesive patch with dry adhesive structures on both the top and bottom surfaces.

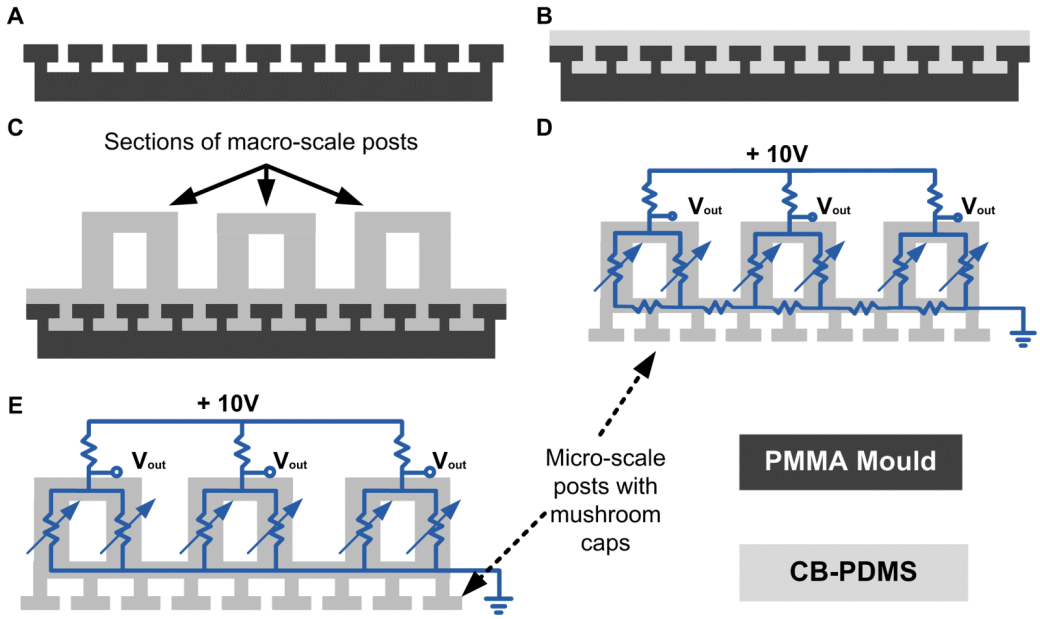

Figure 6-3: **A. 100 mm diameter PMMA mould used to define an array of micro-scale mushroom-like dry adhesive structures. B. CB-PDMS spread over the PMMA mould and degassed. C. Strips of large-scale CB-PDMS posts (indicated by solid arrows) placed on the backing layer of the CB-PDMS dry adhesive structures. D. Fully cured force sensing dry adhesive patch with micro-scale mushroom-like posts (indicated by the dashed arrow). The internal resistance model of the CB-PDMS when used on a non-conducting surface is also shown. E) Internal resistance model for the CB-PDMS when the TFS is used on a conducting surface.**

6.3.3. Modelling

In order to provide some understanding into how the resistance across the TFS changes as the structures undergo a torque, an analytic model using beam theory was developed with the individual posts which form the variable resistors being modelled as a fixed-guided beam as shown in Figure 6-4A.

As briefly described previously, the basic structure of the TFS was composed of a flat layer of CB-PDMS, which composes the grounding layer and doubles as a dry adhesive layer. Atop the base layer, three sections of posts are arranged as shown in Figure 6-4B with the dashed boxes indicating the tip deflection as the top layer of the TFS is twisted as a clockwise torque is applied. This arrangement allows the user to measure a change in the resistance across the sections of posts as the adhesive patch

is either compressed or a torque is applied. Atop each of the three sections of posts, which act as resistors in parallel, is a layer of CB-PDMS that provides an electrical contact surface. When the adhesive patch is compressed evenly across its upper surface, all three sections of posts are compressed in a similar fashion and the resistance change across each post is similar in magnitude. However, as a torque is applied, the tops of the posts composing the outer sections which form the outer ring deflect more than those in the centre section. This difference in the amount of tip deflection results in a greater change in resistance across the posts forming the outer two sections than for the posts in the centre section. This difference in the resistance change between the outer and inner sections can be used to determine if the forces applied to the adhesive patch are compressive or not.

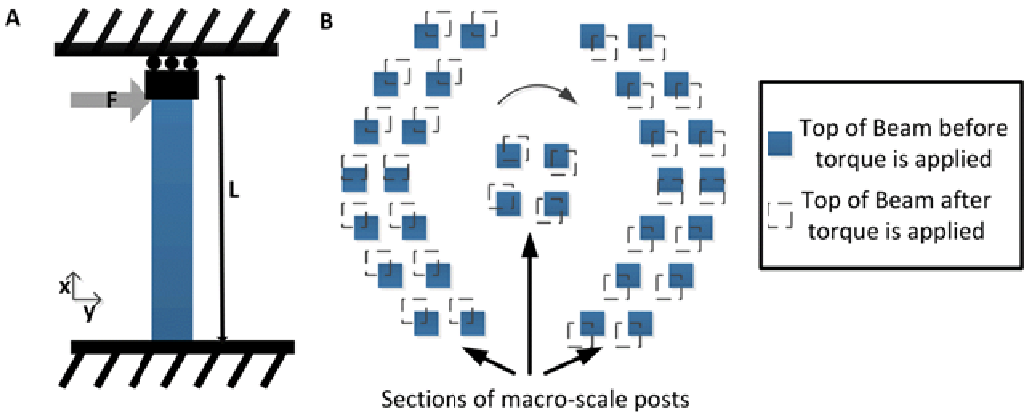

Figure 6-4: A. Fixed-guided beam model used to predict the tip deflection of the posts making up the TFS. B. Top view of the three sections of posts which form the variable resistors of the TFS adhesive patch. When the adhesive patch is subject to a torque, the tips of the outermost posts (blue squares) deflect more than those in the centre region as indicated by the dashed squares when a torque is applied in the direction of the arrow.

An analytical model based on the model of a fixed-guided beam was developed to predict the change in resistance across each post as a torque was applied to the top of the TFS adhesive patch causing the tips of the posts to deflect. For a fixed-guided beam, the boundary conditions at the fixed end are given by (see reference frame shown in Figure 6-4A:

$$x = 0; y = 0; \qquad \text{Equation 6-1}$$

At the guided end of the beam, the boundary conditions are given by:

$$x = L;\ \frac{dy}{dx} = 0 \qquad \text{Equation 6-2}$$

The relationship between the bending moment of a fixed-guided beam and the beam deflection is given by:

$$EI\frac{d^2y}{dx^2} = -Fx + \frac{FL}{2} \qquad \text{Equation 6-3}$$

After integrating both sides of equation 6-3 and applying the boundary conditions shown in (1) and (2), the displacement at any point along the beam is given by:

$$y(x) = \frac{Fx^2}{12EI}(3L - 2x) \qquad \text{Equation 6-4}$$

Under the assumption that the upper and lower sections maintain the same separation throughout the twisting action, the length of the beam must increase slightly by δL as the tip of the post are deflected. An estimate for the increase in the length of the beam can be arrived at by treating the upper and lower halves of the beam under deflection as arcs of constant radius, R for a given force. Geometric considerations can then be used to determine the length of the arc, S, formed by each half of the beam and thus the total increase in the length of the beam δL is given by:

$$\delta L = 2S - L \qquad \text{Equation 6-5}$$

Experimental measurements relating the change in length of a single post to the change in resistivity over the length of the post can be used to estimate the change in the resistance of the adhesive patch as a torque is applied to the upper surface.

6.4. Results and discussion

In order to obtain a relationship between the change in resistivity, ρ, and the increase in the length of a single post, a test was performed a minimum of 6 times on a 1 mm thick by 2 mm wide by 8 mm long rectangular beam composed of CB-PDMS. Both ends of the sample were clamped and electrical contacts attached leaving the gap between both contacts and clamps at either end of the sample at 2 mm. A linear stage (Zaber technologies, T-LS) with an attached load cell (FUTEK, LRF400) was used to stretch the sample while monitoring the applied force. A data acquisition card (National Instruments, NI USB-6259) was used to measure the change in voltage across the sample which acted as a variable resistor within a simple voltage divider as shown in Figure 6-5A. Custom LabView software was used to control the linear stage while recording both the change in voltage across the sample and the distance travelled by the linear stage. Using this setup which is illustrated in Figure 6-5B, a relationship between the increase in length of the sample and the resistivity was determined. Where the resistivity of the sample is related to the resistance, R, across the sample and the sample dimensions by:

$$\rho = \frac{RV}{(L+\delta L)^2} \qquad \text{Equation 6-6}$$

In equation 6-6, V is the sample volume which is considered to be constant even though the sample length is increasing by δL and L is the distance between the clamps and contacts arranged at either end of the sample.

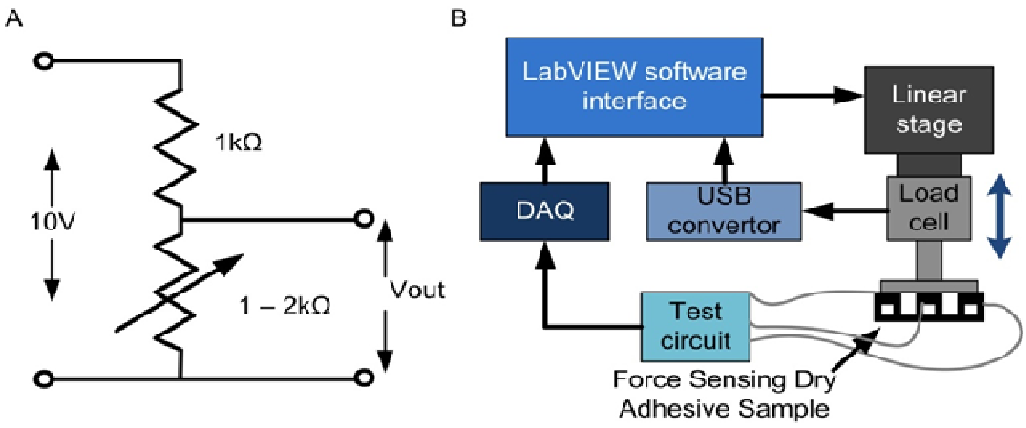

Figure 6-5: A. Expanded view of the test circuit shown in (B). B. Block diagram of the test setup used to measure both the applied normal force and the change in voltage across the force sensing dry adhesive due to the applied pressure. A similar setup was used to measure the change in resistance as a torque was applied to the TFS.

The relationship between the increase in length of the sample and the resistivity of the sample is shown in Figure 6-6 where the error bars indicate the standard deviation of the measurements over a minimum of 6 trials. The parabolic equation which was fit, with an R^2 value of 1, to the average measured resistivity during the 6 trials is shown below:

$$\rho = \alpha\delta L^2 - \beta\delta L + \gamma \qquad \text{Equation 6-7}$$

Where α=0.941, β=5.343 and γ=16.665. After solving equation 6-6 for the change in resistance and substituting in equation 6-7 for the change in the resistivity, the following relationship was used to estimate the change in the resistance as the length of a single post was increased by δL. δL is in mm and the change in resistance, R, is in Ω.

$$R = \frac{(L+\delta L)^2}{V}(\alpha\delta L^2 - \beta\delta L + \gamma) \qquad \text{Equation 6-8}$$

When compressed, the change in the resistance due to the compression of the posts is approximated by:

$$R = \frac{(L-\delta L)^2}{V}(\alpha \delta L^2 - \beta \delta L + \gamma) \qquad \text{Equation 6-9}$$

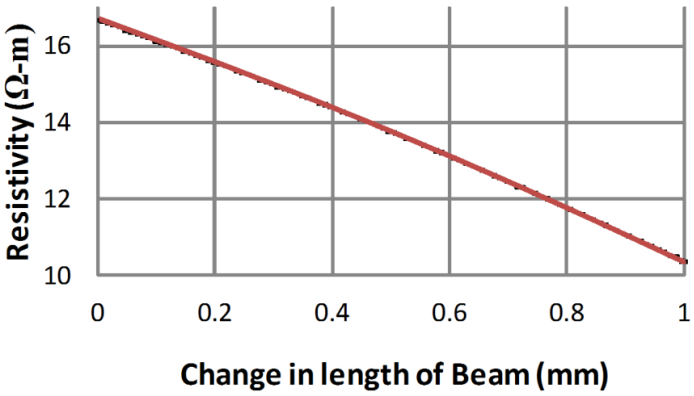

Figure 6-6: The change in resistivity of the sample as the beam is extended using a linear stage. This data was used to form a model to predict the change in the resistance across a single post as a torque was applied to the TFS. The small error bars indicate the standard deviation of the resistivity measurements. The maximum error was 0.073 Ω-m.

Using a setup similar to that shown previously in Figure 6-5b, a linear stage was used to apply a torque to the top layer of the TFS adhesive patch while the change in voltage across the three sections of posts was measured using the data acquisition card. The change in resistance across the centre posts and one of the outer sections of posts is shown in Figure 6-7A with the initial resistance adjusted to zero in order to accurately compare the change in resistance between the centre and outer regions. As can be seen, for the centre posts the application of a torque to the sample results initially in a decrease in the resistance across the contacts as the individual posts begin by bending slightly before beginning to be stretched. The stretching of the posts due to the deflection of their tips results in a sharp increase in the resistance. After reaching a

maximum resistance when a maximum torque of 9.7mN-m is applied to the sample, the direction of the linear stage was reversed and returned to its initial start position. Reversing the direction of the linear stage results in a decrease in the applied torque and thus a sharp decrease in the resistance measured across the posts. When the resistance decreases to approximately 0.6Ω the posts reverse the bending motion which results in a sharp increase (second peak) in resistance. After a total of 31sec. had elapsed the linear stage stops all movement and the resistance across the centre posts gradually reduces as the sample relaxes to its pre-torque condition. For the outer set of posts however, the point when the posts begin to bend occurs much more quickly and the decrease in resistance as the post begin to bend is much less noticeable as the effect of stretching the posts greatly overwhelms any decrease in resistance as the beams begin to bend. The effect of stretching the posts is greater for the outer sections of posts as they are under a greater rotational displacement and thus undergo a greater deflection of their tips than the inner posts. As the linear stage reverses and eventually stops at approximately the 30sec. mark, the resistance across the outer posts decreases swiftly. When the linear stage ceases its motion, the resistance across the outer posts slowly continues to decreases as the material continues to relax over a period of about 50sec. for both the centre and outer sections of posts. Figure 6-7B shows the average measured change in resistance, measured during eleven separate trials, due to the average estimated increase in the length of each post along with the analytical model introduced previously as equation 6-9.

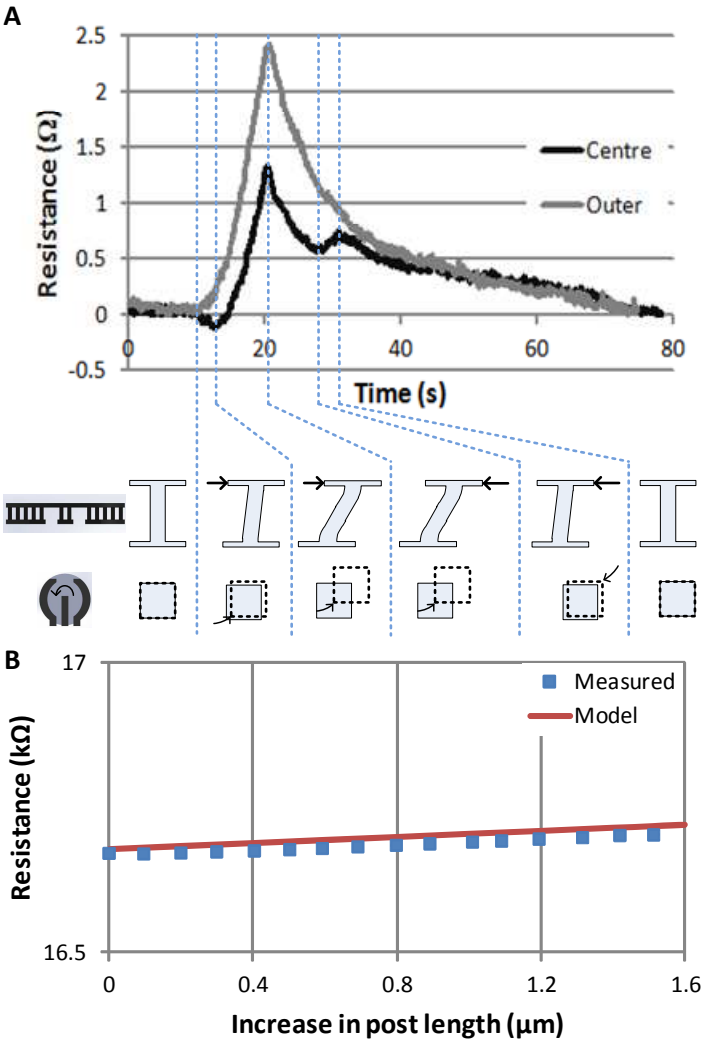

Figure 6-7: **A. The variation in the resistance across the centre and outer sections of the TFS. As can be observed, the outer section undergoes a greater torque than the centre section which results in a greater change in resistance and no decrease in the resistance as the individual post begin to bend under the applied torque. The increase in resistance is caused by the posts being stretched as their tips undergo a rotational displacement as is illustrated form both the side and top view below the figure. B. Comparison between the actual measured change in resistance and the estimated change in resistance with an increase in post length caused by applying a torque to the upper surface of the TFS.**

Since the design of the TFS adhesive patch allows for measuring both compression and torque, the setup previously shown in Figure 6-5B was used to

measure the change in resistance as a linear stage and load cell were used to apply a constantly measured force to compress the TFS adhesive patch at a rate of 20µm/sec. Figure 6-8 shows the measured resistance change as the TFS was compressed over several trials. The double peak in the decrease in resistance, which is most noticeable for the centre section of posts, is due to the posts within each section beginning to buckle under the applied force. This effect is more noticeable for the centre section of the TFS because there are only 4 posts in that section while the outer sections are each made up of 23 posts. After reaching the limit of its forward motion the linear stepper stage is reversed and the compression force is reduced resulting in a steep rise in the resistance across the TFS as the material relaxes. As can be seen in Figure 6-8, after the first compression/relaxation cycle the resistance across the TFS is higher than the initial resistance which is likely due to stresses remaining within the material. During subsequent compression/relaxation cycles the resistance across the TFS is a little lower than the resistance measured before each cycle and the peak decrease in resistance is also slightly lower for each cycle. Again, this phenomenon is likely because, during these trials, the material is not able to completely relax between cycles. The applied force in each trial was 762±10 mN.

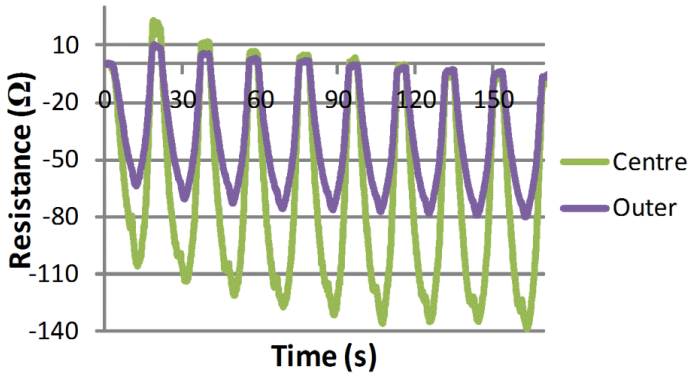

Figure 6-8: Change in resistance across both the centre and one of the outer sections of posts that make up the TFS under multiple compression forces. To aid in a comparison between the change in resistance across both the centre and outer regions the initial resistance has been adjusted to 0 Ω.

In order to determine the time required for the CB-PDMS material making up the TFS to completely relax after a single trial, several trials were performed under different

loading conditions and the change in resistance across the sample was recorded after a single compression/relaxation cycle. For an applied compression force of 762±10 mN, the time required for the material to completely relax was found to be about 21 sec. For an applied compression force of 14.8 N, as shown in Figure 6-9A, the time required for the material to completely relax after being compressed was 382 sec.

After performing four series of tests with a minimum of 7 tests each, such as previously shown in Figure 6-8, the average change in resistance as the sample was compressed was determined. Figure 9B shows the average change in resistance along with the estimated change in resistance as calculated using equation 6-9 as the sample was compressed. Equation 6-9 overestimates the change in resistance because it is based on the change in resistance as a beam was stretched while the actual measured change in resistance shown in Figure 6-9B is due to the TFS being compressed.

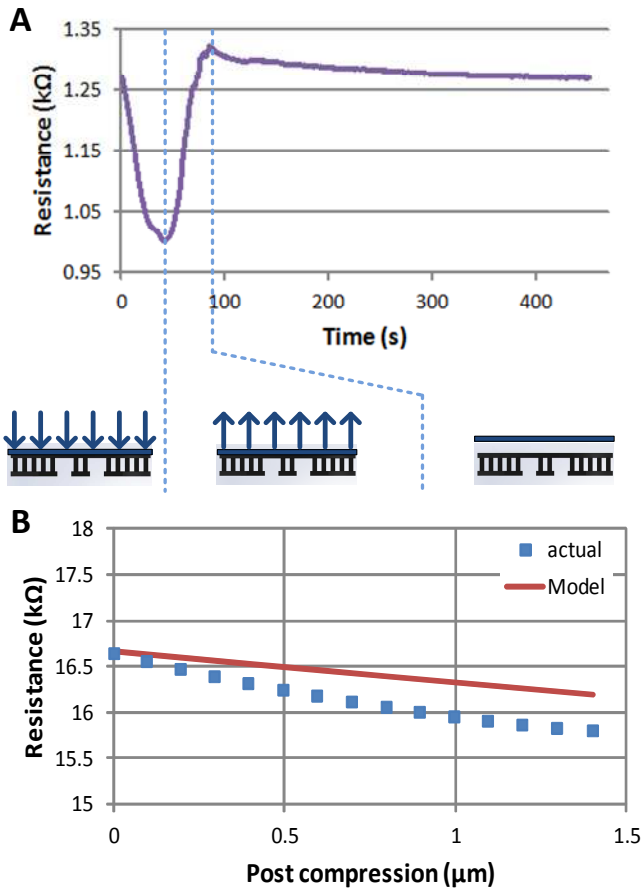

Figure 6-9: **A. The variation in resistance as the TFS is compressed and then allowed to relax. In the first 48 sec. the TFS is compressed by the linear stage followed by the direction of the stage being reversed. After 92 sec. had passed the linear stage is detached from the TFS as illustrated below the plot and the resistance across the outer terminal of the TFS spikes sharply before slowing decreasing again as the posts relax. The applied force was 14.8 N. B. A comparison of the actual measured change in the resistance across a single post making up the TFS and the single beam under compression model.**

When under tension, the TFS can detect when adhesive detachment occurs. In order to show this, a linear stage was used to compress the TFS and provide a preload to the adhesive surfaces as previously discussed. For the trial shown in Figure 6-10, only the effect of tension on the TFS is shown. It should also be noted that for ease in understanding the effect of tension on the increase in resistance across the terminals of the TFS, the initial resistance across the terminals was adjusted to 0 Ω. After reaching the desired preload force, in this case 871±10 mN, the direction of the linear stage was

then reversed until adhesive detachment occurred. As the tension on the TFS begins to increase, the resistance across the terminals also increases until, after approximately 10 sec. had elapsed, the adhesive began to detach. After the adhesive begins to detach the resistance continues to increase, albeit at a slower rate until, at the point of complete detachment, there is a large spike in the resistance which can be seen at approximately the 40 sec. mark in Figure 6-10. At the point of detachment, the tension on the TFS was measured to be 920±10 mN. After the adhesives are fully detached the resistance across the TFS decreases as the material relaxes and, after approximately 80 sec. had elapsed, the CB-PDMS material making up the TFS was fully relaxed.

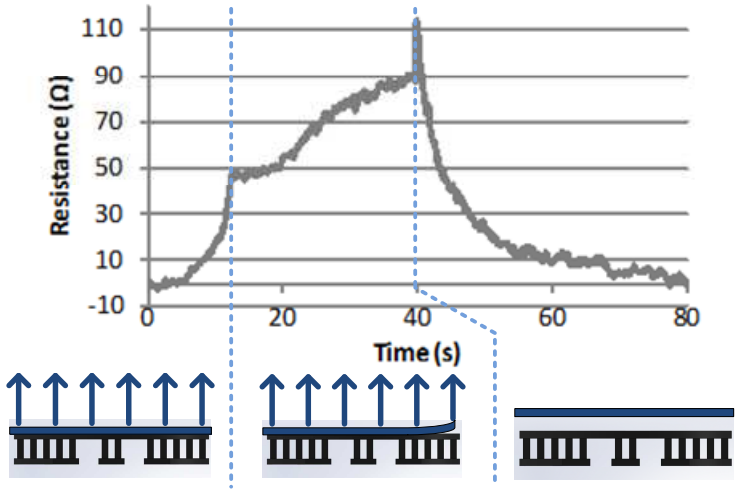

Figure 6-10: The resistance change across the TFS while under tension. In this case, a maximum tension of 920±10 mN results in complete adhesive detachment which is indicated by the large, sharp, spike in resistance to approximately 115 Ω. The change in the rate of increasing resistance after approximately 10sec. had passed is due to the adhesive starting to detach as illustrated below the plot.

6.5. Conclusion

Force sensing dry adhesives were manufactured which were capable of measuring an applied compressive stress ranging from 0.11 Pa to 20.9 kPa as well as a torques ranging from 2.6 mN-m to 10 mN-m. The design of the TFS allows the user to distinguish whether a torque, tension or a compressive force is applied based on a

comparison of the resistance change across the central and outer sections of posts. A beam model was used to validate the supposition that under an applied torque, the individual posts which make up different sections of the force sensing dry adhesive are stretched. Using the measured change in resistance across a single beam as it was extended and relating these measurements to the change in length of the posts as a torque was applied, resulted in a model which closely approximated the change in resistance across a post as a torque was applied. Similarly, a model was developed in order to predict the change in resistance across a single post making up the TFS as the adhesive patch was compressed. Future work on the TFS should include ensuring a method for uniform force distribution such as embedding stiff plates on the upper and lower surfaces or adding additional macro-scale posts formed from non-conducting PDMS. Additionally, since the CB-PDMS is a viscoelastic material, additional research should be performed in order to reduce the relaxation time of the TFS by selecting and incorporating a more suitable material than CB-PDMS.

6.6. Acknowledgement

This work was financially supported by The Natural Sciences and Engineering Research Council of Canada (NSERC)

6.7. References

(1) Autumn, K.; Sitti, M.; Liang, Y. A.; Peattie, A. M.; Hansen, W. R.; Sponberg, S.; Kenny, T. W.; Fearing, R.; Israelachvili, J. N.; Full, R. J. Evidence for van Der Waals Adhesion in Gecko Setae. Proc. Natl. Acad. Sci. U. S. A. 2002, 99, 12252–12256.

(2) Hui, C.-Y.; Glassmaker, N. J.; Tang, T.; Jagota, a. Design of Biomimetic Fibrillar Interfaces: 2. Mechanics of Enhanced Adhesion. J. R. Soc. Interface 2004, 1, 35–48.

(3) Sameoto, D.; Menon, C. Direct Molding of Dry Adhesives with Anisotropic Peel Strength Using an Offset Lift-off Photoresist Mold. J. Micromechanics Microengineering 2009, 19, 115026.

(4) Krahn, J.; Sameoto, D.; Menon, C. Controllable Biomimetic Adhesion Using Embedded Phase Change Material. Smart Mater. Struct. 2011, 20, 015014.

(5) Davies, J.; Haq, S.; Hawke, T.; Sargent, J. A Practical Approach to the Development of a Synthetic Gecko Tape. Int. J. Adhes. Adhes. 2009, 29, 380–390.

(6) Ho, A. Y. Y.; Yeo, L. P.; Lam, Y. C.; Rodríguez, I. Fabrication and Analysis of Gecko-Inspired Hierarchical Polymer Nanosetae. ACS Nano 2011, 5, 1897–1906.

(7) Sameoto, D.; Menon, C. Recent Advances in the Fabrication and Adhesion Testing of Biomimetic Dry Adhesives. Smart Mater. Struct. 2010, 19, 103001.

(8) Kwak, M. K.; Pang, C.; Jeong, H.-E.; Kim, H.-N.; Yoon, H.; Jung, H.-S.; Suh, K.-Y. Towards the Next Level of Bioinspired Dry Adhesives: New Designs and Applications. Adv. Funct. Mater. 2011, 21, 3606–3616.

(9) Greiner, C.; Campo, A. Del; Arzt, E. Adhesion of Bioinspired Micropatterned Surfaces: Effects of Pillar Radius, Aspect Ratio, and Preload. Langmuir 2007, 23, 3495–3502.

(10) Varenberg, M.; Gorb, S. Close-up of Mushroom-Shaped Fibrillar Adhesive Microstructure: Contact Element Behaviour. J. R. Soc. Interface 2008, 5, 785–789.

(11) Jeong, H. E.; Suh, K. Y. Nanohairs and Nanotubes: Efficient Structural Elements for Gecko-Inspired Artificial Dry Adhesives. Nano Today 2009, 4, 335–346.

(12) Parsaiyan, H.; Barazandeh, F.; Mehdirezaei, S.; Parsaiyan, M.; Safdari, M. Wide-End Fibers and Their Adhesion Performance in Biological Attachment Systems. Int. J. Adhes. Adhes. 2009, 29, 444–450.

(13) Del Campo, A.; Greiner, C.; Arzt, E. Contact Shape Controls Adhesion of Bioinspired Fibrillar Surfaces. Langmuir 2007, 23, 10235–10243.

(14) Segal, E.; Tchoudakov, R.; Narkis, M.; Siegmann, A. Sensing of Liquids by Electrically Conductive Immiscible Polypropylene/thermoplastic Polyurethane Blends Containing Carbon Black. J. Polym. Sci. Part B Polym. Phys. 2003, 41, 1428–1440.

(15) Liu, C.-X.; Choi, J.-W. Patterning Conductive PDMS Nanocomposite in an Elastomer Using Microcontact Printing. J. Micromechanics Microengineering 2009, 19, 085019.

(16) Niu, X. Z.; Peng, S. L.; Liu, L. Y.; Wen, W. J.; Sheng, P. Characterizing and Patterning of PDMS-Based Conducting Composites. Adv. Mater. 2007, 19, 2682–2686.

(17) Cong, H.; Pan, T. Photopatternable Conductive PDMS Materials for Microfabrication. Adv. Funct. Mater. 2008, 18, 1912–1921.

(18) Krahn, J.; Menon, C. Electro-Dry-Adhesion. Langmuir 2012, 28, 5438–5443.

(19) Fujigaya, T.; Haraguchi, S.; Fukumaru, T.; Nakashima, N. Development of Novel Carbon Nanotube/Photopolymer Nanocomposites with High Conductivity and Their Application to Nanoimprint Photolithography. Adv. Mater. 2008, 20, 2151–2155.

(20) Lu, J.; Lu, M.; Bermak, A.; Lee, Y. Study of Piezoresistance Effect of Carbon Nanotube-PDMS Composite Materials for Nanosensors. In Procedings of the 7th IEEE Iternational Conference on Nanotechnology August 2-5, 2007, Hong Kong; 2007; pp. 1240–1243.

(21) Yu, W. J.; Lee, S. Y.; Chae, S. H.; Perello, D.; Han, G. H.; Yun, M.; Lee, Y. H. Small Hysteresis Nanocarbon-Based Integrated Circuits on Flexible and Transparent Plastic Substrate. Nano Lett. 2011, 11, 1344–1350.

(22) Sekitani, T.; Yokota, T.; Kuribara, K.; Someya, T. Simultaneous Characterization of Mechanical and Electrical Performances of Ultraflexible and Stretchable Organic Integrated Circuits. In 2012 IEEE International Conference on Microelectronic Test Structures (ICMTS); 2012; pp. 206–210.

(23) Lu, N.; Lu, C.; Yang, S.; Rogers, J. Highly Sensitive Skin-Moutable Strain Guages Based Entirely on Elastomers. Adv. Funct. Mater. 2012, 22, 4044–4050.

(24) Yamada, T.; Hayamizu, Y.; Yamamoto, Y.; Yomogida, Y.; Izadi-Najafabadi, A.; Futaba, Don, N.; Hata, K. A Stretchable Carbon Nanotube Strain Sensor for Human-Motion Detection. Nat. Nanotechnol. 2011, 6, 296–301.

(25) Yaul, F. M.; Bulovic, V.; Lang, J. H. A Flexible Underwater Pressure Sensor Array Using a Conductive Elastomer Strain Guage. J. Microelectromechanical Syst. 2012, 21, 897–907.

(26) Han, J.-E.; Kim, D.; Yun, K.-S. All-Polymer Hair Structure with Embedded Three-Dimensional Piezorestive Force Sensors. Sensors Actuators A Phys. 2012, 188, 89–94.

(27) Li, Y.; Ahmed, A.; Sameoto, D.; Menon, C. Abigaille-II: Towards the Development of a Spider-Inspired Climbing Robot. Robotica 2012, 30, 79–89.

(28) Santiago, D.; Rodríguez-Calero, G. G.; Rivera, H.; Tryk, D. a.; Scibioh, M. A.; Cabrera, C. R. Platinum Electrodeposition at High Surface Area Carbon Vulcan-XC-72R Material Using a Rotating Disk-Slurry Electrode Technique. J. Electrochem. Soc. 2010, 157, F189.

Chapter 7. Characterization of dry adhesives fabricated using a novel mass production manufacturing technique

The content of this chapter has been slightly modified from what first appeared in print in:

Krahn, Jeffrey and Menon, Carlo. Characterization of dry adhesives fabricated using a novel mass production manufacturing technique. *Macromolecular Reaction Engineering* 2013, 7(11), 632-637

7.1. Abstract

Synthetic dry adhesives, designed to mimic the fibrillar structures found on geckos, have been fabricated using many different techniques ranging from indenting wax to involving photo lithography and laser writing. While these techniques have been successful in the fabrication of small dry adhesive samples, they are often costly, time consuming and require specialized equipment. In this study a novel fabrication technique is proposed which utilizes readily available commercial wire mesh screens as a straight forward method of producing synthetic dry adhesives outside of a cleanroom or highly specialized facilities. The normal adhesion pressure of the dry adhesives fabricated using the wire mesh screens is examined and compared to the normal adhesion pressure of flat PDMS.

7.2. Introduction

Geckos are able to adhere to a wide range of surfaces using hierarchical fibrillar structures which rely on van der Waals' forces for adhesion. The hierarchical fibrillar structures found on the tips of the geckos' toes allow the close surface-surface contact necessary for van der Waals' forces to occur[1]. The hierarchical structures also allows

relatively stiff materials to conform to rough surfaces thus improving contact area and increasing the adhesion force due to van der Waals' interactions. These simple observations have inspired many different groups to design and develop synthetic gecko adhesives, often called dry adhesives, for use with climbing robots[2–5] where fast, reliable and strong adhesion is required[6–9].

There have been many different approaches to the fabrication of dry adhesives. While many of the fabrication techniques involve a molding technique[5,10–14] often casting polymers such as poly(dimethylsiloxane) (PDMS)[10,11,15], the fabrication of the molds and dry adhesives often require specialized equipment and processes found in cleanrooms and laboratories such as photo lithography[13,14], deep reactive ion etching (DRIE)[16–19], nano-drawing[20], direct laser writing[21], e-beam lithography[22] and plasma etching[23,24]. The use of such specialized equipment often results in uniform arrays of nano- or micro-scale fibrillar structures. However, the overall dimensions of the dry adhesives and moulds tend to be relatively small and costly to fabricate which does not translate well to commercial fabrication where large-scale production techniques are necessary to reduce costs and improve throughput.

Several groups have found simpler fabrication techniques which have made use of indenting wax using nano-indenters and Atomic Force Microscope (AFM) tips[1,25]. More recently, a hybrid micro-machining process was developed that allows the fabrication of mould cavities for densely packed wedge-shaped dry adhesives using a standard CNC milling machine to indent wax with the tip of a knife blade[26]. While these techniques have proven useful for the fabrication of dry adhesive samples, a fast, inexpensive and simpler method for dry adhesive fabrication is needed if dry adhesives are to be commercially manufactured or produced in high quantities.

This study examines the normal adhesion properties of dry adhesives with an overhanging mushroom-like cap fabricated using a simple, yet novel, technique which

may, in the future, be translatable into mass production. Using wire mesh screens which are readily available commercially and which can be ordered in a variety of sizes, the mesh is secured to a thin layer of pre-cured PDMS. After the mesh is secured in place, a thin layer of PDMS is spread over the surface of the mesh and then scraped off using a straight blade before the final curing step. After curing, the mesh is removed from the cured PDMS leaving micro-scale mushroom-like dry adhesive structures with overhanging caps.

7.3. Methods and materials

In this study, dry adhesives were made using a technique which could easily be scaled for mass manufacturing of dry adhesives. The dry adhesives examined in this study were fabricated by first rinsing a sheet of Poly(methyl methacrylate) (PMMA) with DI water followed by drying with N_2 before placing the PMMA in a thermal chamber at 100 ^{o}C for 1 min to remove any remaining moisture. After drying the PMMA sheet, PDMS, already degassed in a vacuum chamber and mixed in the ratio of 10 parts pre-polymer to 1 part curing agent, was evenly distributed over the surface of the PMMA and allowed to sit for several minutes on a flat level surface. Allowing the PDMS so sit for several minutes resulted in a thin even coating of PDMS over the entire surface of the PMMA. The PMMA and PDMS were then placed in a thermal chamber set at 80 ^{o}C and allowed to cure for 1 hr. After allowing the cured PDMS to cool, a commercially available mesh sheet (Ted Pella Inc.) made from interwoven micro-scale wires or threads was placed atop the PDMS and stretched and held in place using tape. After securing the mesh, a small amount of premixed PDMS was poured and spread over the surface of the mesh. After degassing in a vacuum chamber for 30 min, a razor blade was used to scrape off the excess PDMS resulting in a very thin layer of PDMS remaining on the surface of the mesh. The PMMA, PDMS and mesh were then placed in a thermal chamber set at 80^{o} C for 3 hrs. to allow the PDMS to fully cure. Once the PDMS had cooled, the mesh was carefully removed from the surface of the PDMS resulting in the formation of mushroom-like structures on the surface of the PDMS. After peeling the PDMS dry adhesive sheet from the PMMA substrate, the dry adhesive was ready for use. A diagram of the manufacturing process can be seen in Figure 7-1. It should be

noted that the overhanging caps are formed by tearing the thin layer of PDMS covering the mesh as the mesh is removed and results in non-uniform overhanging caps.

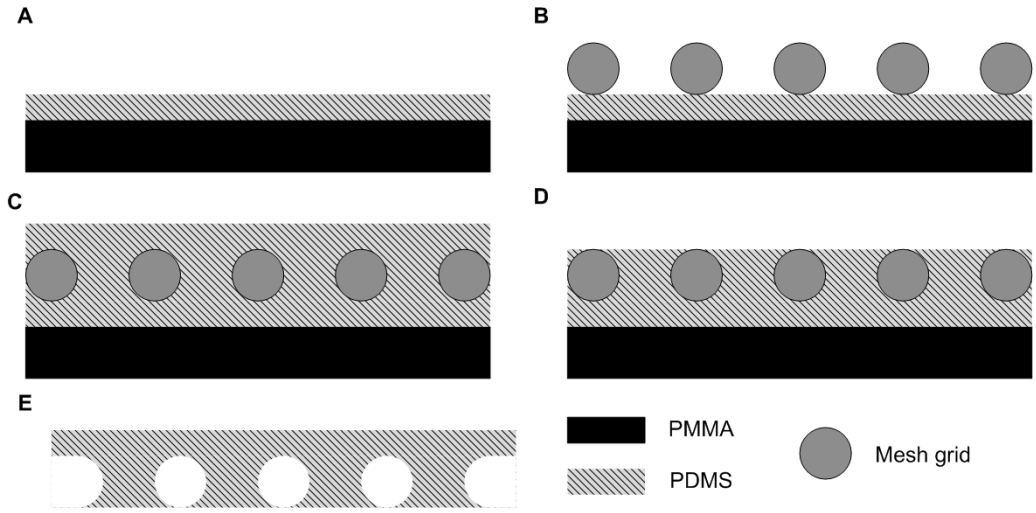

Figure 7-1: Manufacturing processing steps. A. PMMA is coated with a thin layer of PDMS and allowed to cure. B. Mesh grid is placed on top of the cured PDMS and stretched tightly. C. PDMS is poured over the mesh grid and degassed. D. Excess PDMS is scraped off the surface of the mesh grid and allowed to cure in place. E. The mesh grid and PMMA backing layer are removed leaving the PDMS dry adhesive sheet with flat topped mushroom-like structures.

The mushroom-like structures were then examined using a Scanning Electron Microscopes (SEM) as can be seen in Figure 7-2, which shows the dry adhesive structures formed using a Nylon 150 mesh. Figure 7-3 shows a SEM image of the dry adhesive structures formed using a Stainless Steel 150 (SS 150) mesh.

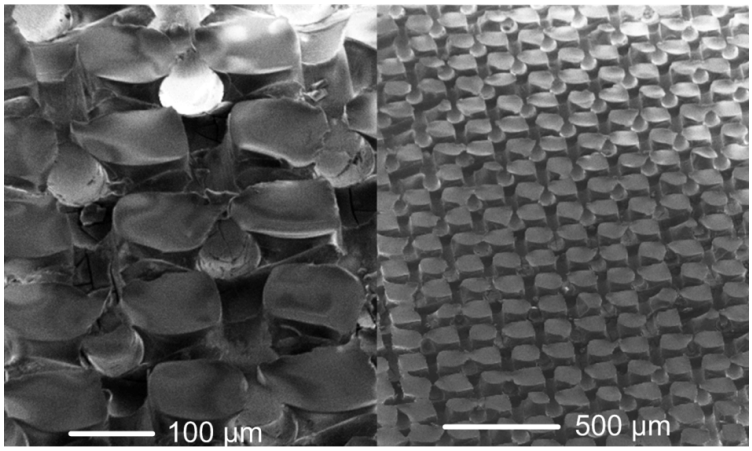

Figure 7-2: Scanning Electron Microsope (SEM) image of dry adhesive fibres fabricated using a Nylon 150 mesh.

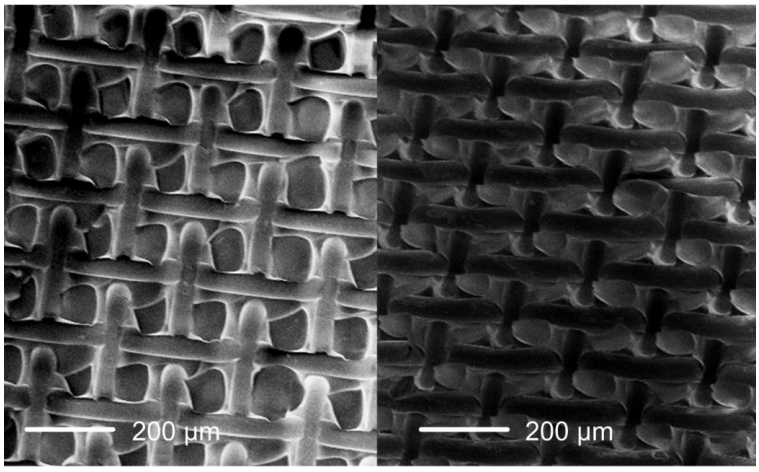

Figure 7-3: SEM image of dry adhesive structures formed using a stainless steel 150 mesh.

In order to test the adhesive abilities of the dry adhesives, a 6 mm spherical sapphire probe tip was attached directly to a load cell (FUTEK, LRF400) which, in turn, was fastened directly to a linear stage (Zaber Technologies, T-LS). A custom LabVIEW interface was used to control the motion of the linear stage and provide force feedback control during testing while recording the stage position, stage speed and the force measured by the load cell. A diagram of the test setup can be seen in Figure 7-4.

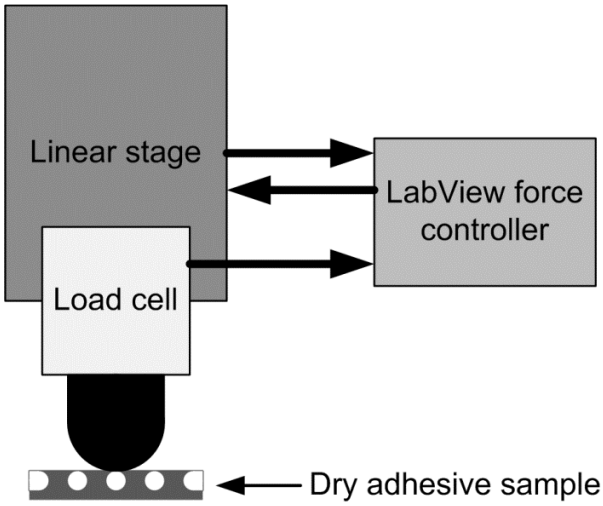

Figure 7-4: Diagram of the normal adhesion test setup.

7.4. Results and discussion

In order to study the normal adhesion of the dry adhesives, samples were prepared as previously discussed. Using a 6 mm diameter spherical sapphire probe attached directly to a load cell, an average preload force of 306 ± 8 mN was applied to each of the five samples: flat PDMS and dry adhesives made using Stainless Steel 150 (SS 150) mesh, Nylon 150 mesh, Polyester 300 (Poly 300) mesh and Polyester 400 (Poly 400) mesh. All meshes were purchased from Ted Pella Inc. and each dry adhesive sample was prepared as previously discussed. A minimum of eight trials was performed for each sample.

In order to estimate the area of the dry adhesive surface in contact with the sapphire probe, the distance the linear stage travelled while applying a preload to each of the samples was recorded. By subtracting the linear stage position upon first contact of the probe with the sample from the linear stage position at the maximum preload, the indentation depth of the tip of the spherical probe was determined. Using the radius of

the spherical probe, R, and the indentation depth, d, the apparent contact area, Asph, of the spherical probe tip with the dry adhesive sample was determined using:

$$A_{sph} = 2\pi Rd \quad (1)$$

For the flat PDMS sample, the apparent area in contact was the same as the actual area in contact. For the dry adhesives however, the actual area in contact during testing was estimated from the dimensions of the wire/thread and the width of the square openings in the mesh, which formed the overhang during the removal of the mesh during fabrication, as specified by the manufacturer[27] and can be seen in Table 7-1. The actual area in contact was used in the determination of the preload pressure and pull-off pressure. It should also be noted that the wire or thread diameter controls the spacing between the dry adhesive fibres as well as the height of the fibres whereas the dimensions of the opening determines the size of the cap and supporting structure.

Table 7-1: Summary of the wire/thread diameter, cross-sectional opening width which is directly related to the area of the overhanging cap, and the approximate percentage of the total area of the adhesive making up the mushroom-like overhanging cap. The openings were square for all of the meshes[27].

Sample	Wire/Thread diameter [µm]	Opening width [µm]	Resulting adhesive area [% total area]	Aspect ratio of the fibres [height:width]
Flat	-----	-----	100	-----
SS 150	66	104	37.4	66:104
Nylon 150	76	100	32.3	76:100
Poly 300	41	41	25	1:1
Poly 400	43	28	15.6	43:28

For the dry adhesives manufactured from the SS 150 mesh, the fibres were 66 µm tall and were supported on posts 104 µm wide resulting in short, chubby structures. During adhesion testing, the average preload force was measured to be 307 ± 3 mN with the sapphire probe indenting the surface by an average depth of 13 ± 1 µm. The measured indentation depth corresponds to an average actual area in contact of 0.094 ±

0.007 mm^2 and resulted in the lowest average normal adhesion pressure of 118 ± 22 kPa for the dry adhesives tested.

During testing, the dry adhesives made using the Nylon 150 mesh, which were 76 µm tall with 100 µm wide supporting posts, underwent an average preload force of 307 ± 8 mN with the sapphire tip indenting the dry adhesive surface 12.7 ± 0.3 µm. This resulted in an average actual contact area of 0.077 ± 0.002 mm^2 and an average normal adhesion pressure of 240 ± 12 kPa.

The 41 µm tall dry adhesives which were fabricated from the Poly 300 mesh were supported on 41 µm wide posts and underwent a preloading force of 305 ± 6 mN. The average measured indentation depth was 14 ± 1 µm and corresponds to an average actual contact area of 0.041 ± 0.003 mm^2. The dry adhesives fabricated from the Poly 300 mesh had the highest average normal adhesion pressure which was measured to be 350 ± 51 kPa.

The dry adhesives fabricated using the Poly 400 mesh were 43 µm tall supported on 28 µm wide posts. Under an average preloading force of 307 ± 4 mN, the sapphire tip indented the surface of the adhesives by 12.8 ± 0.7 µm and resulted in an average actual contact area of 0.060 ± 0.003 mm^2. The average normal adhesion pressure was 184 ± 19 kPa.

Lastly, in order to show an improvement in adhesion pressure of the dry adhesives over flat PDMS, a flat PDMS sample was preloaded with an average preloading force of 307 ± 6 mN. Since the PDMS was unstructured, the actual and apparent contact areas were the same at 0.19 ± 0.02 mm^2 when indented by the probe to an average depth of 10 ± 1 µm. This resulted in the lowest measured average adhesion pressure at 50 ± 6 kPa.

Figure 7-5 shows a comparison of the adhesion pressure for all of the samples tested under an average preloading force for all samples of 306 ± 8 mN. The adhesion pressure for the dry adhesive samples varies from sample to sample due to a number of reasons. During the fabrication process, the thin layer of PDMS coating the mesh is torn as the mesh is removed. The tearing of the caps results in non-uniform overhanging caps with somewhat ragged edges as were shown in Figure 7-2 and Figure 7-3 and likely accounts for some variations in adhesion pressure seen for the dry adhesive samples. Another factor affecting the adhesion pressure is the ability of the dry adhesive fibres to comply to the surface of the spherical probe. Since all of the dry adhesives are manufactured from different meshes, they all have different aspect ratios as previously shown in Table 7-1. Higher aspect ratio fibres having a greater ability for the posts to deform and the dry adhesive surface to comply to the surface of the spherical probe resulting in higher adhesion pressures. Interestingly, the dry adhesives fabricated using the Poly 300 mesh, with a 1:1 aspect ratio, had the highest measured adhesion while the highest aspect ratio dry adhesives, fabricated from the Poly 400, had slightly decreased adhesion pressure. The slight decrease in adhesion pressure for the dry adhesives fabricated from the Poly 400 mesh may be due to the way the PDMS overhanging caps tear during the removal of the mesh. During mesh removal, the smaller caps may be subject to greater tearing due to the decreased geometry. Overall, the average adhesion pressure with the structured dry adhesives, 223 ± 17 kPa, was greater than for flat PDMS which was 50 ± 6 kPa. An ANOVA analysis was performed to ensure that the difference in adhesion pressure between all samples was statistically significant. The computed F ratio, as a result of the ANOVA analysis, was 234.7546 while the critical F value, F_{α,ν_1,ν_2}, where α is 1 minus the confidence interval, ν_1 is the number of adhesive samples minus 1 and ν_2 is the total number of tests performed minus the number of adhesive samples. For the adhesive testing described, the critical F value read from a standard F distribution table for $F_{0.05,\ 4,\ 50}$, was 2.5572 indicating that the difference in adhesion pressures between samples was statistically significant.

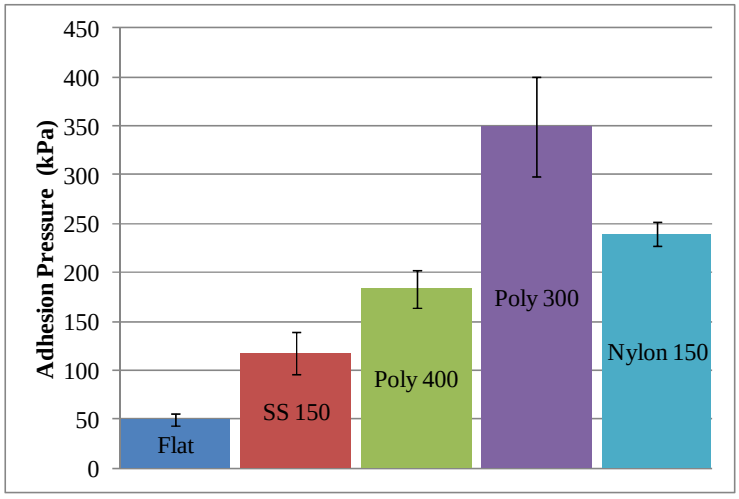

Figure 7-5: A comparison of the adhesion pressure for all of the samples tested. The error bars represent the standard deviation. The applied preload force was 306 ± 8 mN.

Figure 5-6 shows the relationship between the actual area in contact and the normal adhesion pressure. In all cases, as can be seen in Figure 7-5 and Figure 7-6, the structured dry adhesives all showed increased adhesion pressure over the flat PDMS. Figure 5-7 compares the indentation depth of the probe for all of the tested samples under an average applied preload of 306 ± 8 mN. The dry adhesive samples require a greater indentation depth over the flat PDMS sample due to the reduced area in contact since only the flat tops of the fibres contact the probe. Also, the shape of the fibres reduces the stiffness of the dry adhesive sheets which requires a greater indentation depth to achieve the same preload.

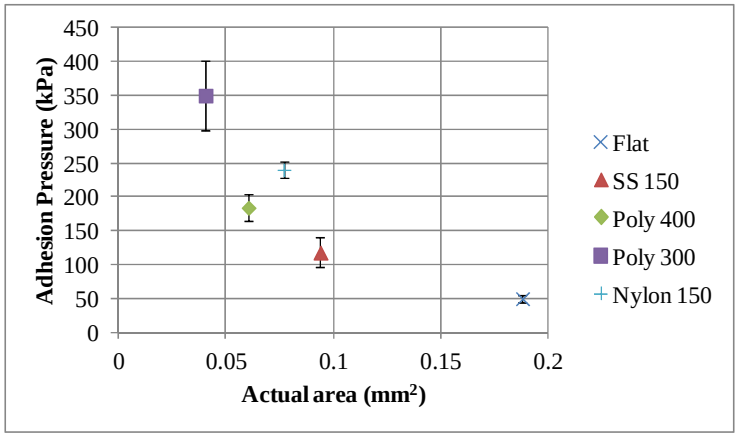

Figure 7-6: **The relationship between the actual area in contact and the adhesion pressure. Due to the higher adhesion pressure, in all cases the dry adhesives had increased adhesion pressure over the flat PDMS even though the flat PDMS had the largest area in contact.**

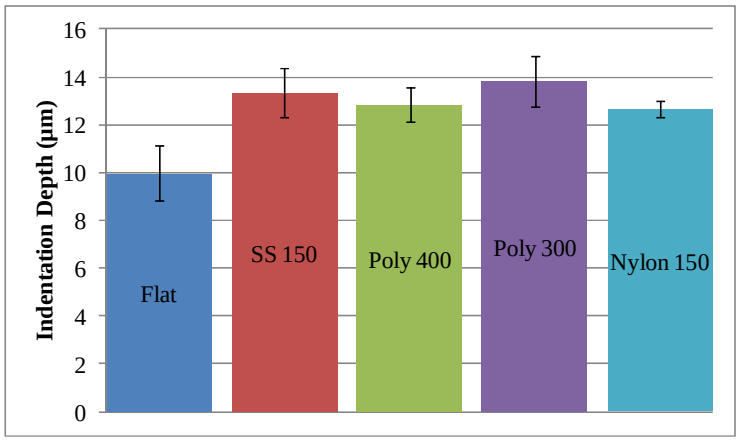

Figure 7-7: **The variation in the indentation depth of the spherical sapphire sphere. The mushroom-like structures of the dry adhesive samples results in a greater indentation depth when compared to flat PDMS due to the lower actual area in contact for the dry adhesives. The average applied preload force was 306 ± 8 mN.**

7.5. Conclusion

A novel method of manufacturing dry adhesives, which could easily and inexpensively be translated to a high throughput manufacturing process, was developed. The novel fabrication process can be performed easily without requiring costly and time consuming cleanroom fabrication processes or equipment such as E-beam lithography, photo lithography, plasma etching or other highly specialized processes. Several different commercially available meshes were used to fabricate dry adhesives with overhanging mushroom caps. The normal adhesion pressure for the dry adhesive samples was measured and compared to flat unstructured PDMS. Of the meshes used to fabricate the dry adhesives, the polyester 300 mesh had the greatest average normal adhesion pressure at 350 ± 51 kPa. The adhesion pressure for dry adhesives made with the polyester 400, nylon 150 and stainless steel 150 meshes were 184 ± 19 kPa, 240 ± 12 kPa and 118 ± 22 kPa respectively while flat PDMS showed the lowest adhesion pressure at 50 ± 6 kPa. There are several drawbacks to the manufacturing of adhesives using the method described in this report including a minimum resolution, a low density of fibres, and a non-uniform post geometry depending on the interwoven mesh types available. However, electroformed meshes could be used to overcome the drawbacks of using woven meshes resulting in a higher density of fibres and uniform post geometry.

7.6. Acknowledgement

This work was financially supported by the Natural Sciences and Engineering Research Council of Canada (NSERC) and made use of 4D LABS shared facilities supported by the Canada Foundation for Innovation (CFI), British Columbia Knowledge Development Fund (BCKDF), Western Economic Diversification Canada, and Simon Fraser University.

7.7. References

(1) Autumn, K.; Sitti, M.; Liang, Y. A.; Peattie, A. M.; Hansen, W. R.; Sponberg, S.; Kenny, T. W.; Fearing, R.; Israelachvili, J. N.; Full, R. J. Evidence for van Der Waals Adhesion in Gecko Setae. *Proc. Natl. Acad. Sci. U. S. A.* **2002**, *99*, 12252–12256.

(2) Krahn, J.; Liu, Y.; Sadeghi, A.; Menon, C. A Tailless Timing Belt Platform (TBCP-II) Utilizing Dry Adhesives with Mushroom Caps. *Smart Mater. Struct.* **2011**, *20*, 11.

(3) Unver, O.; Murphy, M. P. Geckobot and Waalbot : Small-Scale Wall Climbing Robots. In *AIAA 5th Aviation, Technology, Integration and Operations Conference*; Arlington, Virginia, 2005.

(4) Li, Y.; Ahmed, A.; Sameoto, D.; Menon, C. Abigaille-II: Towards the Development of a Spider-Inspired Climbing Robot. *Robotica* **2012**, *30*, 79–89.

(5) Kim, S.; Spenko, M.; Trujillo, S.; Heyneman, B.; Santos, D.; Cutkosky, M. R. Smooth Vertical Surface Climbing with Directional Adhesion. *IEEE Trans. Robot.* **2008**, *24*, 65–74.

(6) Varenberg, M.; Gorb, S. Close-up of Mushroom-Shaped Fibrillar Adhesive Microstructure: Contact Element Behaviour. *J. R. Soc. Interface* **2008**, *5*, 785–789.

(7) Del Campo, A.; Greiner, C.; Arzt, E. Contact Shape Controls Adhesion of Bioinspired Fibrillar Surfaces. *Langmuir* **2007**, *23*, 10235–10243.

(8) Jeong, H. E.; Suh, K. Y. Nanohairs and Nanotubes: Efficient Structural Elements for Gecko-Inspired Artificial Dry Adhesives. *Nano Today* **2009**, *4*, 335–346.

(9) Parsaiyan, H.; Barazandeh, F.; Mehdirezaei, S.; Parsaiyan, M.; Safdari, M. Wide-End Fibers and Their Adhesion Performance in Biological Attachment Systems. *Int. J. Adhes. Adhes.* **2009**, *29*, 444–450.

(10) Glassmaker, N. J.; Himeno, T.; Hui, C.-Y.; Kim, J. Design of Biomimetic Fibrillar Interfaces: 1. Making Contact. *J. R. Soc. Interface* **2004**, *1*, 23–33.

(11) Sameoto, D.; Menon, C. A Low-Cost, High-Yield Fabrication Method for Producing Optimized Biomimetic Dry Adhesives. *J. Micromechanics Microengineering* **2009**, *19*, 115002.

(12) Sameoto, D.; Menon, C. Direct Molding of Dry Adhesives with Anisotropic Peel Strength Using an Offset Lift-off Photoresist Mold. *J. Micromechanics Microengineering* **2009**, *19*, 115026.

(13) Greiner, C.; Campo, A. Del; Arzt, E. Adhesion of Bioinspired Micropatterned Surfaces: Effects of Pillar Radius, Aspect Ratio, and Preload. *Langmuir* **2007**, *23*, 3495–3502.

(14) Aksak, B.; Murphy, M. P.; Sitti, M. Adhesion of Biologically Inspired Vertical and Angled Polymer Microfiber Arrays. *Langmuir* **2007**, *23*, 3322–3332.

(15) Parness, A.; Soto, D.; Esparza, N.; Gravish, N.; Wilkinson, M.; Autumn, K.; Cutkosky, M. A Microfabricated Wedge-Shaped Adhesive Array Displaying Gecko-like Dynamic Adhesion, Directionality and Long Lifetime. *J. R. Soc. Interface* **2009**, *6*, 1223–1232.

(16) Hui, C.-Y.; Glassmaker, N. J.; Tang, T.; Jagota, a. Design of Biomimetic Fibrillar Interfaces: 2. Mechanics of Enhanced Adhesion. *J. R. Soc. Interface* **2004**, *1*, 35–48.

(17) Kim, S.; Sitti, M.; Hui, C.-Y.; Long, R.; Jagota, A. Effect of Backing Layer Thickness on Adhesion of Single-Level Elastomer Fiber Arrays. *Appl. Phys. Lett.* **2007**, *91*, 161905.

(18) Kim, S.; Sitti, M. Biologically Inspired Polymer Microfibers with Spatulate Tips as Repeatable Fibrillar Adhesives. *Appl. Phys. Lett.* **2006**, *89*, 261911.

(19) Kim, S.; Sitti, M.; Xie, T.; Xiao, X. Reversible Dry Micro-Fibrillar Adhesives with Thermally Controllable Adhesion. *Soft Matter* **2009**, *5*, 3689.

(20) Jeong, H. E.; Lee, S. H.; Kim, P.; Suh, K. Y. Stretched Polymer Nanohairs by Nanodrawing. *Nano Lett.* **2006**, *6*, 1508–1513.

(21) Röhrig, M.; Thiel, M.; Worgull, M.; Hölscher, H. Hierarchical Structures: 3D Direct Laser Writing of Nano- and Microstructured Hierarchical Gecko-Mimicking Surfaces. *Small* **2012**, *8*, 3009–3015.

(22) Tsai, Y.-C.; Shih, W.-P.; Wang, Y.-M.; Huang, L.-S.; Shih, P.-J. E-Beam Photoresist and Carbon Nanotubes as Biomimetic Dry Adhesives. *19th IEEE Int. Conf. Micro Electro Mech. Syst.* **2006**, 926–929.

(23) Davies, J.; Haq, S.; Hawke, T.; Sargent, J. A Practical Approach to the Development of a Synthetic Gecko Tape. *Int. J. Adhes. Adhes.* **2009**, *29*, 380–390.

(24) Geim, A. K.; Dubonos, S. V; Grigorieva, I. V; Novoselov, K. S.; Zhukov, A. A.; Shapoval, S. Y. Microfabricated Adhesive Mimicking Gecko Foot-Hair. *Nat. Mater.* **2003**, *2*, 461–463.

(25) Sitti, M.; Fearing, R. S. Synthetic Gecko Foot-Hair Micro/nano-Structures as Dry Adhesives. *J. Adhes. Sci. Technol.* **2003**, *17*, 1055–1073.

(26) Day, P.; Eason, E. V; Esparza, N.; Christensen, D.; Cutkosky, M. Micro-Wedge Machining for the Manufacture of Directional Dry Adhesives. *J. Micro Nano-Manufacturing* **2013**, *1*, 10.

(27) Ted Pella Inc. Sceening, Stainless Steel Wire Mesh, Nylon, Polyester, Polypropylene, Fluorocarbon Mesh, http://www.tedpella.com/grids_html/44814.htm (accessed March, 2013).

Chapter 8. Conclusion

In conclusion, the overall goal of this thesis, the design of functional dry adhesives through technological advancement and application development was met by addressing the following three objectives which were established as a way to achieve this goal:

1. Design switchable dry adhesives that are capable of rapid switching between a high and low adhesion state
2. Design force and torque sensing adhesives
3. Design a manufacturing method that does not require a cleanroom environment

Objective 1 was met through the development of switchable dry adhesives through two different approaches: electrostatic force generation and magnetic material stiffness control. Switchable dry adhesives primarily address three of the ideal properties of synthetic dry adhesives listed in chapter 2.1. Namely, switchable dry adhesives provide isotropic adhesion, a high pull-off to preload ratio and low detachment force when required although they also rely on van der Waals' interactions and are anti self-matting.

Chapters 3 and 4 discuss the design, fabrication and testing of electro-dry-adhesives that use conductive polymer electrodes to generate attractive electrostatic voltages when a high voltage was applied across the flexible electrodes. In addition to increased adhesion in shear when utilizing both Van der Waals' adhesion and electrostatic adhesion, the generated electrostatic force was also capable of providing the electro-dry-adhesives with a self-preloading mechanism that could allow the electro-dry-adhesives to ensure good long-term dry adhesion even under the influence of external forces. Increases in shear bond strength ranging from 400% to 2046% over that of flat unstructured CB-PDMS were achieved on several attachment substrates including drywall, PP and PMMA. The self-preloading mechanism provided by electro-dry-adhesives resulted in an average 1.8 kPa increase in shear adhesion. Second

generation electro-dry-adhesives were fabricated with interdigitated conductive polymer electrodes and were compatible with conductive attachment substrates and showed a 256% improvement in shear adhesion bond strength.

Objective 1 was also addressed in chapter 5 where the design, manufacturing and testing of magnetic field controllable dry adhesives was discussed. The magnetically controlled dry adhesives were fabricated with Iron Oxide nanoparticles embedded in a PDMS matrix and, in the presence of a magnetic field were shown to increase the overall stiffness of the device. Depending on the orientation of the applied magnetic field an increase or decrease in the overall thickness of the device was observed. The increase or decrease in device thickness resulted in an increase or decrease in measured normal adhesion bond strength depending on the orientation of the applied magnetic field when the magnetic field was applied during the pull-off portion of the normal adhesion test cycle only. When the 0.0133 ± 0.0009 T magnetic field was present during either preload only or during the entire adhesion cycle a decrease in adhesion was observed due to an increase in the overall stiffness of the device.

Objective 2 was addressed in chapter 6 where the design of force and torque sensing dry adhesives was discussed. The force sensing dry adhesives were capable of measuring compression forces ranging from 0.11Pa to 20.9 kPa as well as torques ranging from 2.6 mN m to 10 mN m. The design of the TFS, which incorporated arrays of CB-PDMS macro-scale pillars, enabled the user to distinguish whether a torque or tension or compressive force was applied to the device. A beam model was used to validate the assumption that under a torque, individual beams that make up the TFS were stretched. The force and torque sensing dry adhesives provided adhesion primarily through van der Waals' interactions and exhibited a high pull-off to preload ratio which were two of the ideal properties of synthetic dry adhesives that mimic the gecko foot as discussed in chapter 2.1.

Finally, objective 3, the design of a manufacturing method which does not require a cleanroom environment, was achieved through the development of a novel fabrication technique for dry adhesives that used commercially available meshes as a mold for the dry adhesive fibres was presented in chapter 7. Dry adhesive were manufactured using several different meshes and the adhesion they provided was compared. The greatest

normal adhesion pressure (350 ± 51 kPa) were measured from dry adhesives manufactured using a polyester 300 mesh while dry adhesives manufactured using polyester 400, nylon 150 and stainless steel 150 meshes were 184 ± 19 kPa, 240 ± 12 kPa and 118 ± 22 kPa respectively. The synthetic dry adhesives manufactured using the method described in chapter 7 provide adhesion primarily through van der Waals interactions, exhibited a high pull-off to preload ratio, and anti self-matting which are three of the ideal properties of synthetic dry adhesives that mimic the gecko foot.

Future work will be focused on integrating the fabrication method discussed in chapter 7 with the switchable and force and torque sensing dry adhesives described in chapters 3 through 6. By integrating the work described within this thesis we anticipate the ability to fabricate low-cost functional dry adhesives.